

## **Distribution Agreement**

In presenting this thesis or dissertation as a partial fulfillment of the requirements for an advanced degree from Emory University, I hereby grant to Emory University and its agents the non-exclusive license to archive, make accessible, and display my thesis or dissertation in whole or in part in all forms of media, now or hereafter known, including display on the world wide web. I understand that I may select some access restrictions as part of the online submission of this thesis or dissertation. I retain all ownership rights to the copyright of the thesis or dissertation. I also retain the right to use in future works (such as articles or books) all or part of this thesis or dissertation.

Signature:

---

Michael N. Sullivan

---

Date

# Electronic Spectroscopy of Polycyclic Aromatic Hydrocarbons (PAHs) and Group IIA Metallic Oxides

By

Michael Neal Sullivan  
Doctor of Philosophy

Physical Chemistry

---

Michael C. Heaven, PhD.  
Advisor

---

Susanna Widicus Weaver, PhD.  
Committee Member

---

Tim Lian, PhD.  
Committee Member

Accepted:

---

Lisa A. Tedesco, PhD.  
Dean of the James T. Laney School of Graduate Studies

---

Date

Electronic Spectroscopy of Polycyclic Aromatic  
Hydrocarbons (PAHs) and Group IIA Metallic Oxides

By

Michael Neal Sullivan  
Master of Science

Advisor: Michael C. Heaven, PhD.

An abstract of  
A dissertation submitted to the Faculty of the  
James T. Laney School of Graduate Studies of Emory University  
in partial fulfillment of the requirements of the degree of  
Doctor of Philosophy  
in Physical Chemistry  
2017

## Abstract

Electronic Spectroscopy of Polycyclic Aromatic Hydrocarbons (PAHs)  
and Group IIA Metallic Oxides  
By Michael Neal Sullivan

Electronic spectroscopy is a powerful technique which can be used to elucidate the nature of bonding and structural characteristics in a variety of molecular species through the study of electronic interactions. This dissertation examines two such applications of electronic spectroscopy focusing on the study of polycyclic aromatic hydrocarbons (PAHs) and group IIA metallic oxides.

PAHs are well known to be involved in the formation of soot, affecting both the environment and human health. Two intermediate species involved in the process of PAH formation are the phenoxy and phenylperoxy radicals. These radicals were generated using an electrical discharge coupled with a supersonic expansion source. Absorption spectra were recorded using cavity ringdown spectroscopy. Molecular constants and excited state lifetimes were derived from the observed spectra. These results were supplemented using electronic structure calculations.

Group IIA metal oxides exhibit unusual bonding characteristics that are not well described by standard models. Additionally, they are also promising candidates for laser cooling experiments utilized in the generation of ultracold molecules. However detailed information on their internal state distribution required for these studies is lacking. Spectroscopic studies of three calcium oxide species are presented: CaO, CaOH, and CaOCa. Laser ablation coupled with a supersonic expansion was used to generate gas phase oxides. Emission spectra were recorded in the visible region using laser induced fluorescence spectroscopy. Molecular constants were determined from corresponding vibronic bands.

# Electronic Spectroscopy of Polycyclic Aromatic Hydrocarbons (PAHs) and Group IIA Metallic Oxides

By

Michael Neal Sullivan  
Master of Science

Advisor: Michael C. Heaven, PhD.

A dissertation submitted to the Faculty of the  
James T. Laney School of Graduate Studies of Emory University  
in partial fulfillment of the requirements of the degree of  
Doctor of Philosophy  
in Physical Chemistry  
2017

## **Acknowledgments**

Every journey has a beginning, and my decision to pursue a career in chemistry began in 2007 when I chose to perform my undergraduate research project with Dr. Scott Reeve at Arkansas State University (ASU) as I started my junior year. At the time I had my mind set on medical school, but as the year progressed I discovered how much I enjoyed working on my research project, which was a study of degradation products in explosive materials. I continued my research with Dr. Reeve through the next year, and when my senior year began I realized that my aspirations for beginning medical school in the next year were unlikely. Dr. Reeve encouraged me to instead stay at ASU and pursue a Masters degree while working in his research group with a new postdoctoral associate he had just hired, Dr. Chris Lue. While working with Chris I quickly realized medical school wasn't for me, and I wanted to continue my career in the field of physical chemistry (more specifically as a spectroscopic). To Scott and Chris, I thank you both for encouraging me to continue on this path, which has been more rewarding than I could have ever imagined.

Thanks to Chris, I had the extraordinary opportunity to complete my doctoral studies under his former research advisor, Dr. Michael Heaven at Emory University. Since the very beginning Michael has been there to assist me in any way he can. His guidance (along with my other teachers) throughout the frustration of classwork and cumulative exams has provided me with background knowledge necessary to be an effective researcher. He is hands on in the lab as well, always willing to lend assistance and to address difficult problems in the laboratory, so that you are prepared to anticipate when similar problems arise in the future, you are ready to tackle them

head on. I can safely say with the utmost confidence that you will be hard pressed to find a better advisor and mentor than Michael. For this and so much more, I thank you for all of your help Michael. If I am able to become half the scientist and mentor that you are, then I can think of no greater accomplishment.

I also like to thank my committee members, Dr. Tim Lian and Dr. Susanna Widicus Weaver, for helping me grow as a researcher during my tenure as a graduate student at Emory. I would especially like to thank Susanna for serving as my secondary mentor. Your passion for science and teaching is unparalleled. It was my pleasure to serve as a laboratory teaching assistant for you as a first year graduate student, which instilled in me the confidence I needed to realize that I can be a passionate and effective mentor to young students eager to learn new skills and expand their knowledge in all multiple fields of science.

During my time at Emory, I have had the great fortune to work with a number of enterprising scientists. This collaborative effort has been paramount to the success and completion of several research projects presented in this dissertation. To each of you, I owe a debt of gratitude for your support and assistance: Dr. Keith Freel (PAH intermediates), Dr. Jacob Stewart (CaO/CaOH), Dr. Wafaa Fawzy (CaOCa theoretical calculations, and Dr. Daniel Frohman (CaOCa experimental work).

Special thanks are also addressed to several members of the Emory staff for their help over the years. I would like give special thanks to Cody Anderson in the machine shop for crafting our ablation sources, Patrick Morris in the electronics shop for helping us fix many fried circuit boards in our lasers, Steve Krebbs in the chemistry stockroom for always making sure I had the chemicals and specialized orders necessary to do science every day, and finally to Ann Dasher, the graduate student coordinator in the chemistry department. Ann is the real administrative workforce for the graduate students, helping me (and the rest of the graduate students) make sure I've gotten all of my paperwork turned in on time.

My graduate research has been greatly aided by the technical assistance and intellectual input I have received from each member of the Heaven lab over the years. Along the way I have established a strong working relationship with each of you. First and foremost of these is our former group member Joshua Bartlett. While things always seem frustrating you have a keen knack for easing the stress at work, be it with your penchant for pulling pranks, or your ramblings of all the characters in the Star Wars extended universe that no one person alone should have knowledge of. And of course when I speak of pranksters I must not forget Kyle Mascaritolo, whose natural talent as a jokester is matched only by his love for pizza products (and his Buddy). Most recently I've had the privilege of working with Robert Vangundy, and while he has a bit of reputation as a cranky sports nut, he is a truly fantastic researcher and overall fantastic person with a heart of gold (which might be candy covered at this point). I'd also like to thank the newer members of the Heaven Lab: Sean Bressler, Mallory Theis (soon to be Green), and Amanda Dermer for providing me with constructive comments and feedback on several of my reports and presentations.

Over the years I've developed strong friendships with my fellow graduate students outside of the Heaven Lab that I hope will extend long my past my tenure here at Emory. To each of you (especially to Pravin Muthu, AJ Mesko, Leann Teadt, Kevin Roenitz, and Becky Bartlett), I treasure our friendship and thank you for your guidance and support during our graduate career and beyond.

The end of this journey has been a most difficult one, but it is safe to say that I could not have made it without the support of the love of my life, Jessica Hurtak. Jessica, you are the most caring and dedicated person I have ever met. Even when things seem most dire, you are always there to remind me of all the good things we have. Like our puppies, Rusty and Cassie, you never let anything get you down. You push me to keep challenging myself, which along with your overwhelming encourage-

ment helps to make me a better person every single day. I am quite literally the luckiest man in the world, and I am so thankful for everything you do for me. You will forever be my bb1.

Finally, I'd like to thank my friends and family back home for all of their support over the years. To my friends Mark and Zac, thanks for always keeping me entertained and alleviating some of the stress of graduate school. You have no idea how much you helped me unwind with your ridiculous antics and ravings. To my parents, brother, and sister: who have always believed in me and knew that I could accomplish anything I put my mind to, I love each of you with all of my heart. While it has been extraordinarily hard to be so far apart from you, I am glad I came here as I've accomplished so much. Now comes the next journey, wherever it may lead. Only time will tell, and as a great author once said,

All we have to decide is what to do with the time that is given to us.

- J.R.R. Tolkien

# TABLE OF CONTENTS

## List of Tables

## List of Figures

<b>1</b>	<b>Motivation</b>	<b>1</b>
1.1	Radical Intermediates in Soot Formation . . . . .	1
1.2	Candidates for Ultracold Molecules:	
	Calcium Oxides . . . . .	8
<b>2</b>	<b>Experimental Techniques</b>	<b>15</b>
2.1	Cavity Ringdown Spectroscopy . . . . .	15
2.2	Laser Induced Fluorescence . . . . .	20
2.3	Supersonic Expansion . . . . .	22
<b>3</b>	<b>Cavity Ringdown Spectroscopy of</b>	
	<b>Polycyclic Aromatic Hydrocarbons (PAHs)</b>	<b>25</b>
3.1	The Phenoxy Radical . . . . .	25
	3.1.1 Introduction . . . . .	25
	3.1.2 Methods . . . . .	28
	3.1.3 Experimental Results . . . . .	32
	3.1.4 Theoretical Calculations . . . . .	34
	3.1.5 Discussion . . . . .	40

## TABLE OF CONTENTS

3.2	The Phenylperoxy Radical . . . . .	45
3.2.1	Introduction . . . . .	45
3.2.2	Methods . . . . .	49
3.2.3	Experimental Results . . . . .	50
3.2.4	Theoretical Calculations . . . . .	54
3.2.5	Discussion . . . . .	58
3.3	Conclusion . . . . .	63
<b>4</b>	<b>Laser Induced Fluorescence (LIF) of Calcium Metal Oxides</b>	<b>65</b>
4.1	Calcium Oxide . . . . .	65
4.1.1	Introduction . . . . .	65
4.1.2	Methods . . . . .	67
4.1.3	Results and Discussion . . . . .	69
4.2	Calcium Hydroxide . . . . .	76
4.2.1	Introduction . . . . .	76
4.2.2	Methods . . . . .	79
4.2.3	Results . . . . .	79
4.2.4	Discussion . . . . .	85
4.3	Dicalcium Oxide (CaOCa) . . . . .	88
4.3.1	Introduction . . . . .	88
4.3.2	Methods . . . . .	89
4.3.3	Experimental Results . . . . .	91
4.3.4	Theoretical Calculations . . . . .	95
4.3.5	Discussion . . . . .	97
4.4	Conclusion . . . . .	99
<b>5</b>	<b>Concluding Remarks</b>	<b>102</b>
	<b>Appendix</b>	<b>105</b>

*TABLE OF CONTENTS*

<b>A Phenoxy</b>	<b>105</b>
<b>B Phenylperoxy</b>	<b>106</b>
<b>C CaOCa</b>	<b>112</b>
<b>Bibliography</b>	<b>113</b>

# LIST OF TABLES

3.1	Calculated Vibrational Frequencies for the Phenoxy Radical in the Ground Electronic state, $\tilde{X}^2B_1$ . . . . .	37
3.2	Normal Mode Frequencies for the Phenoxy Radical in the $\tilde{B}^2A_2$ Electronic State . . . . .	39
3.3	Observed Vibronic Bands of the Phenylperoxy Radical . . . . .	53
3.4	Normal Mode Frequencies for the Phenylperoxy Radical in the $\tilde{X}^2A''$ and $\tilde{B}^2A''$ Electronic States . . . . .	56
3.5	Term Energies for the First Three Electronic Transitions of the Phenylperoxy Radical . . . . .	58
4.1	Fitted Molecular Constants for the $C^1\Sigma^+ - X^1\Sigma^+$ Bands of CaO . . .	71
4.2	Equilibrium Electronic and Vibrational Constants for the $C^1\Sigma^+$ and $F^1\Pi$ States of CaO . . . . .	72
4.3	Fitted Molecular Constants for the $F^1\Pi - X^1\Sigma^+$ Bands of CaO . . . .	73
4.4	Fitted Molecular Constants for the $0^+ - X^1\Sigma^+$ Bands of CaO . . . . .	74
4.5	Molecular Constants for the $\tilde{E}^2\Sigma^+ - \tilde{X}^2\Sigma^+$ Vibronic Bands of CaOH . . . . .	84
4.6	Molecular Constants for the $\tilde{E}^2\Sigma^+$ State of CaOH . . . . .	84
4.7	Molecular Constants of CaOCa Vibronic Bands . . . . .	95
A.1	Summary of Geometric Parameters for the Phenoxy Radical . . . . .	105

*LIST OF TABLES*

B.1	Harmonic Vibrational Constants for the $\tilde{B}^2A''$ State of Phenylperoxy . . . . .	106
B.2	Summary of Geometric Parameters for the Phenylperoxy Radical Calculated at the aug-cc-pVDZ Level. . . . .	107
B.3	Summary of Geometric Parameters for the Phenylperoxy Radical Calculated at the aug-cc-pVTZ Level. . . . .	108
B.4	Normal Mode Frequencies for the Phenylperoxy Radical in the $\tilde{A}^2A'$ Electronic State . . . . .	110
B.5	Normal Mode Frequencies for the Phenylperoxy Radical in the $\tilde{C}^2A''$ Electronic State . . . . .	111

# LIST OF FIGURES

1.1	Schematic of Soot Formation . . . . .	5
1.2	Mechanistic Pathways of Soot Formation . . . . .	6
1.3	CaOH Transitions with Largest Franck-Condon Factors . . . . .	11
1.4	Colulomb Crystals of $^{40}\text{Ca}^+$ Reacted with $\text{H}_2$ . . . . .	12
2.1	Simplified Schematic for a Pulsed CRDS Experiment . . . . .	17
2.2	Reduction of Ringdown Time Due to an Absorbing Species in a CRDS Experiment . . . . .	19
2.3	Energy Level Diagram Depicting LIF . . . . .	21
3.1	Experimental Setup Designed for Detection of Radical Intermediates in Soot Formation . . . . .	29
3.2	CRDS Absorption Spectrum of Jet-Cooled Anisole Discharge Products	33
3.3	Molecular Orbitals of the Phenoxy Radical . . . . .	35
3.4	Equilibrium Bond Lengths and Bond Angles for the Phenoxy Radical	36
3.5	Experimental and Calculated Spectra of the $\tilde{\text{B}}^2\text{A}_2 \leftarrow \tilde{\text{X}}^2\text{B}_1$ Transition of the Phenoxy Radical . . . . .	40
3.6	Optically Active Normal Modes in the $\tilde{\text{B}}^2\text{A}_2 \leftarrow \tilde{\text{X}}^2\text{B}_1$ Vibronic Spectrum of the Phenoxy Radical . . . . .	42
3.7	Decomposition Pathway from the Phenylperoxy Radical to the Cyclopentadienyl Radical . . . . .	46

LIST OF FIGURES

3.8	CRDS Spectrum of Bromobenzene Discharge Products . . . . .	51
3.9	Rotational Contour of the Phenylperoxy $\tilde{B}^2A'' \leftarrow \tilde{X}^2A''$ Origin Band . . . . .	54
3.10	Molecular Orbitals of the Phenylperoxy Radical . . . . .	55
3.11	Equilibrium Bond Lengths and Bond Angles for the Phenylperoxy Radical . . . . .	55
3.12	Calculated Vibrationally Resolved Electronic Spectrum of the $\tilde{A}^2A' \leftarrow \tilde{X}^2A''$ Transition of Phenylperoxy Compared with Experimental Data From Literature . . . . .	59
3.13	Optically Active Normal Modes in the $\tilde{B}^2A'' \leftarrow \tilde{X}^2A''$ Vibronic Spectrum of the Phenylperoxy Radical . . . . .	60
4.1	Experimental Setup for LIF Spectroscopy of Calcium Ablation Products . . . . .	67
4.2	Low Resolution Survey Scan of Calcium Ablation Products . . . . .	70
4.3	Rotationally Resolved Vibronic Bands of CaO . . . . .	70
4.4	Survey Scan of Vibronic Bands of CaOH Observed Using LIF . . . . .	80
4.5	Experimental and Simulated Spectra for the 000-000 Band of the $\tilde{E}^2\Sigma^+ - \tilde{X}^2\Sigma^+$ Transition of CaOH . . . . .	81
4.6	Experimental and Simulated Spectra for the 100-000 Band of the $\tilde{E}^2\Sigma^+ - \tilde{X}^2\Sigma^+$ Transition of CaOH . . . . .	82
4.7	Experimental and Simulated Spectra for the 200-000 Band of the $\tilde{E}^2\Sigma^+ - \tilde{X}^2\Sigma^+$ Transition of CaOH . . . . .	83
4.8	Experimental Spectra for the 000-000 Band of the $\tilde{F}^2\Pi - \tilde{X}^2\Sigma^+$ Transition of CaOH . . . . .	85
4.9	Revised Experimental Setup for LIF Spectroscopy of Calcium Ablation Products . . . . .	90
4.10	Initial LIF Survey for CaOCa . . . . .	92

*LIST OF FIGURES*

4.11 Vibronic Bands Observed From Laser Ablation of Calcium in the Red Region of the Visible Spectrum . . . . .	92
4.12 High Resolution LIF Spectrum of a Rotationally Resolved Vibronic Band of CaOCa with PGOPHER Simulation . . . . .	94
4.13 PES for the Ground and First Excited Electronic State of CaOCa . .	97
B.1 Calculated Vibrationally Resolved Electronic Spectra of the Phenylperoxy Radical . . . . .	109
C.1 LIF Scan Containing Unassigned Vibronic Bands . . . . .	112

# Chapter 1

## Motivation

### 1.1 Radical Intermediates in Soot Formation

Climate change has become one of the most defining (and controversial) scientific problems of the late 20<sup>th</sup> and early 21<sup>st</sup> century. Rigorous mathematical modeling has shown that Earth's climate has fluctuated numerous times over millions of years[1]. However, since the beginning of the Industrial Revolution the amount of greenhouse gases present within the atmosphere has risen to a point unexplainable by natural processes, causing an increase in the average global temperature over the years[2]. Greenhouse gases that contribute significantly to rising global temperatures are carbon dioxide, methane, and nitrous oxide[2]. However, larger molecular species could also contribute to rising temperatures due to climate change. For example, secondary organic aerosols (SOA's) constitute a significant fraction of tropospheric aerosols. The properties, formation mechanisms, and transformation of SOA molecules have been the focus of several recent studies and reviews[3, 4, 5].

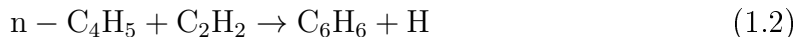
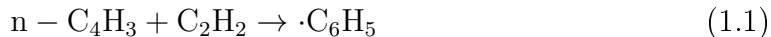
When one speaks of species associated with anthropogenic climate change, one of the largest contributing factors arises from byproducts of internal combustion engines. The efficiency of a modern internal combustion in a standard passenger car is typically

around 10-20 % during day to day usage[6, 7]. Maximum efficiencies of up to 35 % are possible, but not sustainable for extended periods[6]. Ongoing legislation on reducing vehicle emissions is aimed at reducing their impact on the environment, and attempts to improve the efficiency of the internal combustion engine are currently ongoing[8]. Pollutants in vehicle emissions primarily constitute a mixture of NO<sub>x</sub>, CO, and small hydrocarbons, which combine to form soot[8, 9, 10, 11]. Buildup of soot within the combustion chamber hinders the efficiency of the discharge used to break down gasoline, and subsequently reduces the engines efficiency to produce usable fuel used to mechanically power the vehicle. Under fuel rich conditions (high C/O ratio), small aromatic hydrocarbons are formed in the combustion process. These small aromatic hydrocarbons are composed of carbon and hydrogen in a fused ring structure, which contain a minimum of two benzene rings. These small aromatic hydrocarbons are referred to as polycyclic aromatic hydrocarbons (PAHs). PAH formation and subsequent growth is well known to lead to increased soot formation[9, 12], which reduces engine efficiency as noted earlier. This inefficiency leads in turn to increased atmospheric pollution from incomplete combustion byproducts, which exacerbates man made climate change and associated health problems, imposing substantial costs on society[13].

PAH's are a ubiquitous class of compounds. In addition to their impact on increasing greenhouse gas concentrations from mobile emissions in urban/suburban areas[9], they have also been classified as an emerging pollutant for climate change in the Artic region[14]. Additional studies of PAH concentrations and their environmental impact have been performed in various areas of the world, such as: the UK[15, 16, 17], China[18, 19, 20], Canada[21], Japan[22], various Oceans[23, 24], and the United States[25, 26, 27]. One of the main concerns with rising PAH concentrations is the effect that these species have on human health. Consistent occupational exposure to high concentrations of PAHs can cause eye irritation, nausea, vomiting,

diarrhea, etc[28]. Long term effects are more severe, including exacerbated respiratory conditions (i.e. asthma)[29], and several types of cancer[28, 30]. Teratogenic and genetic effects have also been associated with long term PAH exposure and have been well documented[28]. PAH's are also of special interest in the field of astrochemistry, as their presence in the interstellar medium (ISM) has been postulated as a source of mid-infrared emissions[31, 32] and also as carriers of diffuse interstellar bands (DIBs)[33, 34].

PAH formation is generally understood to occur through a process referred to as Hydrogen-Abstraction-C<sub>2</sub>H<sub>2</sub>-Addition, or "HACA" as originally described by Frenklach and Wang[35]. As noted by the acronym, this process involves removal of a hydrogen atom from the reacting hydrocarbon by a free hydrogen followed quickly by the addition of acetylene to the radical site formed. The first step is crucial as it produces the radical products necessary for additional growth, making this the rate limiting step in PAH formation and growth. The formation of the first aromatic ring arises from small chain aliphatic compounds. Two possibilities are generally considered the first step. These are the addition of HC≡C-CH=CH (n-C<sub>4</sub>H<sub>3</sub>) to acetylene (C<sub>2</sub>H<sub>2</sub>) producing the phenyl radical (C<sub>6</sub>H<sub>5</sub>) or the addition of H<sub>2</sub>C=CH-CH=CH (n-C<sub>4</sub>H<sub>5</sub>) to C<sub>2</sub>H<sub>2</sub> producing benzene plus a lone hydrogen atom[36, 37].



Pyrolysis[38] and kinetics[36, 39, 40, 41] studies indicate that the reaction shown in Equation 1.1 plays a vital role in the formation of the first aromatic ring, especially at high temperatures. Equation 1.2, on the other hand, predominates at lower temperatures[36]. Another study by Miller and Melius[42] suggests that the reactions shown in Equations 1.1 and 1.2 cannot proceed in high concentrations as rapid

rearrangement to the iso configuration occurs at high temperatures. Instead they propose the combination of two propargyl ( $C_3H_3$ ) radicals to form benzene or the phenyl radical plus hydrogen



as a candidate for the formation of the first aromatic ring in PAH formation. Later theoretical work[43, 44], most notably a diffusion Monte Carlo (DMC) study by Krokidis *et al.*[45], indicated that the stability of the n-isomer was underestimated compared to iso. These results restored the validity of the mechanisms in Equations 1.1 and 1.2 as candidates for the first ring formation. A combination of these proposed reactions has also been presented as the formation of the first aromatic ring, namely the addition of the propargyl radical to acetylene to form the cyclopentadienyl radical ( $C_5H_5$ )[46].



Additional reactions with the first ring will then occur and eventually form soot (see Figure 1.1). The mechanisms which lead to larger PAHs are still unclear[47, 48]. The HACA process is a viable option; however, studies by Böhm[49] and McKinnon[50] indicate that this mechanism proceeds too slowly compared to PAH formation observed experimentally. Another possible pathway is the polymerization of the phenyl radical to produce larger PAHs[47]. The smallest PAH is naphthalene, which constitutes nearly 50 % of airborne PAH species[51]. Naphthalene is formed through combination of cyclopentadienyl radicals[52, 53, 54], and has been shown to play a large role in further PAH growth[46, 52, 55, 56]. The cyclopentadienyl radical is also well known to contribute significantly to PAH growth through insertion into other aromatic rings[52, 53, 55, 57]. One example is the reaction of the cyclopenta-

dienyl radical with the indenyl radical, which rearranges to form phenanthrene[58].

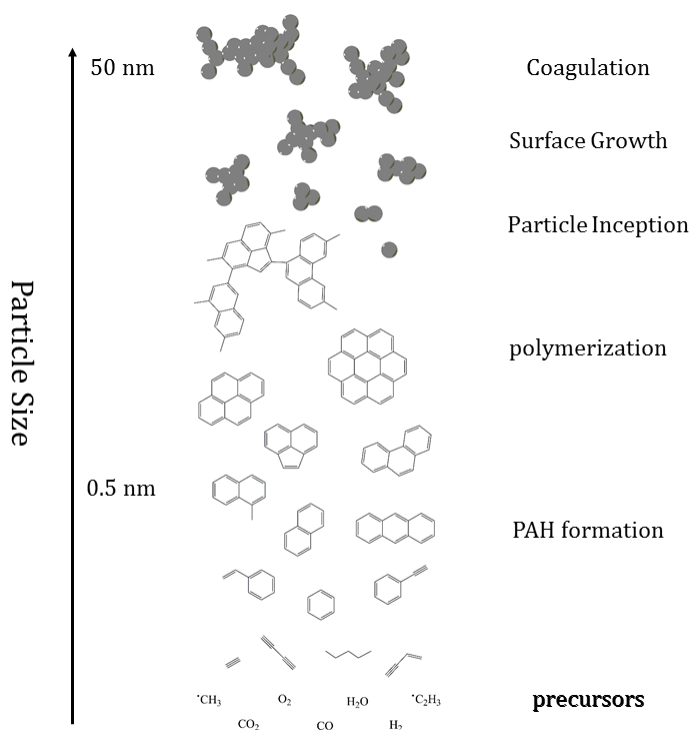


Figure 1.1: Schematic demonstrating the formation of soot starting from small aliphatic chains. These chains lead to aromatic ring formation which combine to form PAHs, which then further combine to form a conglomeration of particles eventually leading to soot formation. Adapted from Bockhorn[59]

Extensive studies of PAH formation and kinetic models exist in the literature. These models are vast and consist of thousands of molecules. Despite the wealth of data available these models are still limited due to the lack of kinetic data on intermediate species involved in these reaction mechanisms. Two intermediate species of vital importance in PAH formation are the phenoxy and phenylperoxy radical. At high temperatures benzene readily dissociates to form the phenyl radical[60]. The phenyl radical can then either react via the phenyl addition/cyclization mechanism reported by Shukla *et al.*[47] to form larger PAHs or with  $\text{O}_2$  to form the phenoxy or phenylperoxy radical[61, 62]. The formation of phenylperoxy by the reaction with  $\text{O}_2$  is a competing pathway to PAH formation. Experimental and theoretical studies

suggest that the decomposition of the phenylperoxy leads to the phenoxy radical as the most abundant product[61, 62, 63, 64]. The phenoxy radical then breaks down into the cyclopentadienyl radical, which as noted earlier can react to form naphthalene (and eventually soot)[64, 65].

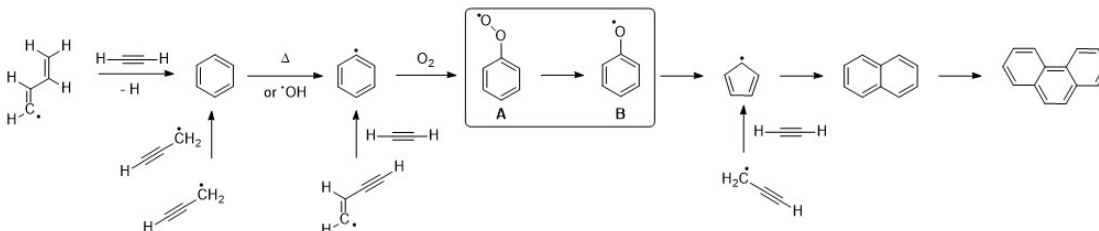


Figure 1.2: Mechanistic pathways involved in the process of soot formation, as outlined in the text. The phenylperoxy radical (A) is formed by the addition of  $\text{O}_2$  to the phenyl radical, the first aromatic ring. Decomposition of the phenylperoxy radical leads to the phenoxy radical (B), which further decomposes to the cyclopentadienyl radical. PAH growth is stimulated by combination of additional aromatic rings, which leads to soot formation.

Kinetic studies have quantified numerous reactions involving species relevant to PAH formation, including the phenoxy and phenylperoxy radicals. Rate constants were extracted for the phenoxy[66] and phenylperoxy[67] radicals by studying their reactions with arylperoxyl and methyl radicals, respectively, using absorption spectroscopy. The next logical step in these studies is to perform a complete spectroscopic characterization on the electronic structure of the intermediates of interest in these kinetic studies. Precise band positions are required in order to monitor the presence of these intermediates. The results from these spectroscopic studies would complement the results from kinetic studies, and provide a more accurate characterization of the structure and corresponding reaction mechanisms associated with these PAH intermediates. The extracted molecular constants would also provide a benchmark for future computational studies.

Ideally, one would consider laser induced fluorescence (LIF) as a promising technique for spectroscopic analysis of these PAH intermediates. LIF is a highly sensitive technique, requiring only that the molecule of study has a sufficient quantum yield,

$\Phi$ [68]. LIF has been used for diagnostic measurements in combustion chemistry since the 1980s[69, 70]. It has also been a useful diagnostic tool for studying PAHs at high temperatures[71, 72] and even in flame sources[73]. However, a previous study in our group determined that the lifetime of the  $9_0^1$  band of the  $1\ ^2B_1 \leftarrow \tilde{X}\ ^2A_1$  transition of the phenyl radical was only 96 ps, with a quantum yield of  $3.4 \times 10^{-5}$ [74]. This could be due to the presence of nonradiative decay channels. It is possible that similar nonradiative decay channels could be present in the phenoxy and phenylperoxy radicals as well due to a large density of states, making LIF a poor candidate for the study of these systems.

Since optical detection by fluorescence cannot be used, an absorption technique must be used instead. In 1993 Yu and Lin performed the first experimental study of PAHs using cavity ringdown spectroscopy (CRDS) in a kinetics study of the phenyl radical[75]. CRDS is an extremely powerful optical absorption technique that utilizes highly reflective mirrors to increase sensitivity by increasing the length of the optical path. The details of this technique are covered in more detail in Section 2.1. CRDS has been widely utilized to characterize the structure[76, 77, 78, 79] and perform kinetics studies[80, 81, 82, 83] of numerous radicals involved in combustion chemistry.

Chapter 3 of this dissertation describes the CRDS experiments of the phenoxy and phenylperoxy radicals. An electrical discharge source was used to produce the radicals of interest, which were jet-cooled to alleviate spectral congestion. Vibronically resolved spectra were recorded in the visible region. These experimental studies were coupled with high level electronic structure calculations in order to assist with spectral assignments. The results and analysis of these findings are presented, along with future work for this project.

## 1.2 Candidates for Ultracold Molecules:

### Calcium Oxides

The ability to produce ultracold molecules is of special interest throughout the scientific community. Applications for ultracold molecules are vast, including (but not limited to) quantum computing[84, 85, 86], the study of dark matter[87], the control and study of chemical reactions at low temperature[88, 89], and atomic clocks([90] and references therein). In the physics community they are especially promising candidates for accurate measurements of several fundamental physical constants[91] including the electron electric dipole moment (eEDM)[92, 93, 94] and variations in the electron-to-proton mass ratio ( $\mu = m_e/m_p$ )[93, 95, 96] and the fine structure constant ( $\alpha = e^2/\hbar c$ )[93, 96, 97], which are consequences of parity violation[98, 99]. Despite being a relatively new area of study, at roughly twenty years old, the concept of ultracold molecules can trace its lineage all the way back to the 1920's. In 1924, Satyendranath Bose derived the Planck law for black body radiation wherein the photons are treated as a gas of identical particles[100]. Bose sent the paper to Albert Einstein who extended the concept to a case of non-interacting atoms[101]. Using this adjusted concept, Einstein predicted that at a very low temperature a large fraction of these atoms condense into the lowest quantum state. The spatial characteristics of a quantum mechanical wave packet of atoms can be defined by the de Broglie wavelength

$$\lambda_{dB} = (2\pi\hbar^2/k_B m T)^{1/2} \quad (1.6)$$

where  $k_B$  is the Boltzmann constant,  $m$  is the atomic mass, and  $T$  is the temperature of the atoms. When the atoms are cooled to the point where  $\lambda_{dB}$  is on the order of interatomic separation, then the wavefunctions of atoms overlap with one another to become a coherent superposition. Assuming the atoms in this process are bosons (i.e. particles with integer values of spin) rather than fermions (i.e. particles with half

integer spin), they occupy the same quantum state at a specific temperature. The occupation of the state is related to the peak atomic density  $n$  by  $n\lambda_{dB}^3 = 2.612$ . This phenomenon is known as Bose-Einstein condensation.

Pioneering work on laser cooling techniques in the 1980's paved the way for the first experimental observation of a Bose-Einstein condensate. Laser cooling was first proposed by Hänsch and Schawlow in 1975[102]. This concept, now referred to as Doppler cooling, assumes a group of atoms in the gas phase are irradiated by six counter propagating laser beams (three pairs of beams along three axes). From a one dimensional view, the lasers are slightly detuned to the red of the atomic resonance frequency. Atoms moving to the right view the frequency of the approaching beam (to the left) as closer to the resonance frequency of the atom than the opposing beam, due to the Doppler effect. The atom will therefore strongly absorb the radiation from the opposing laser, slowing its trajectory. A similar effect is seen for atoms moving to the left. By applying a pair of lasers along the other axes, one obtains three dimensional laser cooling. This is typically the most common form of laser cooling. Other versions, including Sisyphus cooling and sideband cooling, are well described by Cohen-Tannoudji and Phillips[103] and in the 1997 Nobel lectures in Physics by Steven Chu[104], Claude Cohen-Tannoudji[105], and William D. Phillips[106]. Doppler cooling was first performed by Chu *et al.* in 1985[107], who noted that the spatial motion of atoms within the beam is diffusive in nature. Essentially the atoms are trapped within the beams used for laser cooling, earning the nickname "optical molasses". Jean Dalibard suggested the use of circularly polarized light within a weak magnetic field to concentrate the atoms at the center (zero) of the magnetic field, increasing the density of atoms within the trap. Raab *et al.* implemented this suggestion in their first experimental demonstration of the magneto-optical trap (MOT)[108], which increased the number density of cooled atoms from  $\sim 10^6$  (traditional laser cooling only) to  $\sim 10^{12} \text{ cm}^{-3}$ . These advances led to the

first reported observation of a Bose-Einstein condensate of rubidium atoms ( $^{87}\text{Rb}$ ) in 1995[109], followed shortly thereafter by lithium ( $^7\text{Li}$ )[110] and sodium ( $^{23}\text{Na}$ )[111]. For their work on Bose-Einstein condensation of alkali vapors, the 2001 Nobel Prize in Physics was awarded to Eric Cornell, Wolfgang Ketterle, and Carl Wieman[112, 113].

Doppler cooling of atoms is facilitated through the use of a closed optical loop, where photon absorption is always followed by spontaneous decay to the initial state. As no completely closed loop exists in any physical system due to unavoidable spontaneous decay, population in these additional levels must be driven back to the desired "closed loop" using one (or two) "repump" lasers. This is experimentally challenging to implement in molecular systems due to the large density of energy levels available within any given species (i.e. electronic, rotational, vibrational, hyperfine structure). However Di Rosa proposed that certain diatomic molecules may be amenable to direct laser cooling provided they meet three criteria, namely 1) a transition with a large oscillator strength 2) highly diagonal Franck-Condon factors (FCF) for said transition, and 3) a quasi closed optical loop, typically a transition between the ground and first excited electronic state[114]. Direct laser cooling schemes have been proposed for a number of diatomic molecules, including  $\text{TiO}$ [115],  $\text{CaF}$ [116],  $\text{MgF}$ [117],  $\text{AlCl}$ [118],  $\text{AlBr}$ [118],  $\text{AlH}$ [119],  $\text{AlF}$ [119],  $\text{YbF}$ [120],  $\text{RaF}$ [121], and  $\text{SrF}$ [122]. Direct laser cooling has been successfully applied to  $\text{SrF}$ [123],  $\text{CaF}$ [124], and  $\text{YO}$ [125, 126] at mK temperatures. Using an improved magneto-optical trapping scheme[127],  $\text{SrF}$  has since been produced at temperatures three orders of magnitude lower ( $\mu\text{K}$ ) than previously reported[128].

In a recent publication, Isaev and Berger identified several polyatomic molecules suitable for Doppler laser cooling[129], extrapolated from Di Rosa's criteria for Doppler laser cooling of diatomic molecules. Diagonal FCF's are expected (but not guaranteed) in diatomic/polyatomic molecules with one unpaired valence electron, where the electron is promoted between non-bonding orbitals, creating a quasi closed op-

tical loop. These molecules have the general formula  $MF$ , where  $M$  is a group IIA metal, and  $F$  represents a halogen/pseudohalogen species (i.e. CN) or a functional group (i.e. OH). Utilizing this quasi closed optical loop, an optical cycling scheme for SrOH has been very recently demonstrated by Doyle and co-workers[130], which further opens the possibility for direct laser cooling of polyatomic molecules (ex. CaOH, Figure 1.3) in the near future.

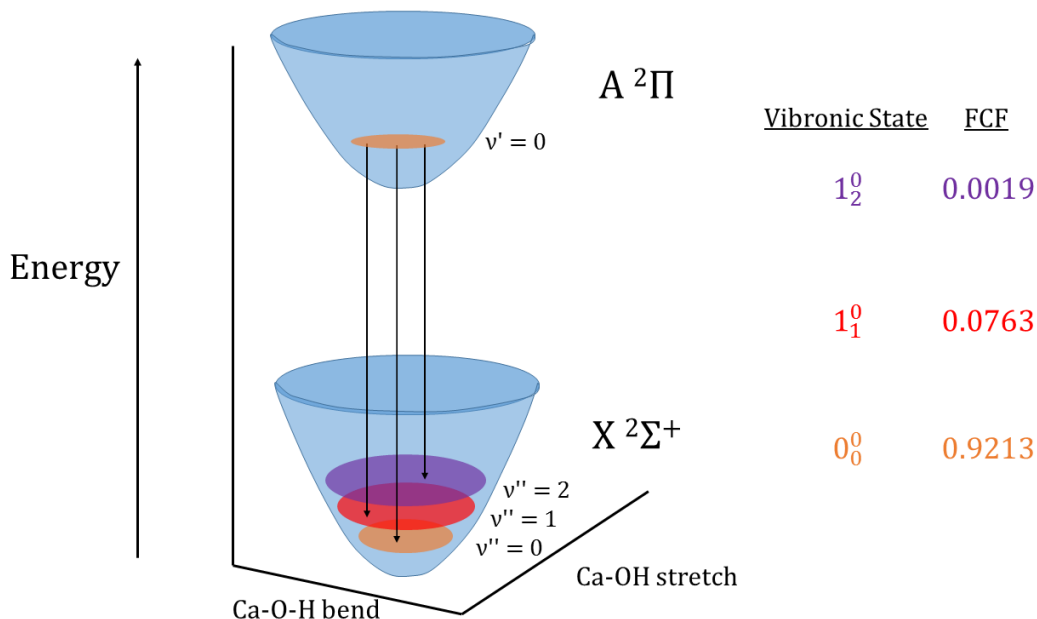


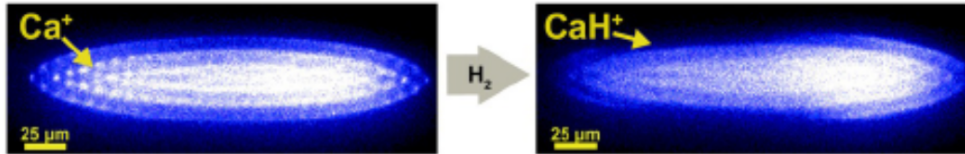
Figure 1.3:  $\tilde{A} \ ^2\Pi - \tilde{X} \ ^2\Sigma^+$  vibronic transitions of CaOH with the largest Franck - Condon factors. The lower coordinate axes correspond to the Ca-OH stretching bond length and bending angle, each displaced from their equilibrium values. The vibronic state assignments (ex.  $1_2^0$ ) listed correspond to the ground (0) vibrational state of the  $\tilde{A} \ ^2\Pi$  state and the vibrational state (1) in the Ca-OH stretching mode, which is doubly (2) excited in the  $\tilde{X} \ ^2\Sigma^+$  state. This figure has been adapted from Isaev and Berger[129].

Several additional methods have been developed and demonstrated in the literature in order to produce ultracold neutral molecules. These methods, including Stark and Zeeman deceleration, buffer gas cooling, photoassociation, and stimulated Raman adiabatic passage (STIRAP) are examined in detail in excellent reviews by Carr *et al.*[131], Quéméner and Julienne[132], and Dulieu and Gabbanini[133]. These also include a broad overview of theoretical and experimental work on ultracold molecules

not described herein.

In contrast to the work on neutral ultracold molecules, production and subsequent studies of ultracold molecular ions require a different approach as those presented above. Sympathetic cooling of molecular ions has proven most effective in generating translationally cold species in the mK temperature range[134]. However, it does not significantly reduce the other internal degrees of freedom within the molecular ion. This is due to the long range Coulombic interactions between molecular ions, forming a lattice of molecular ions surrounded by simultaneously sympathetically cooled atomic ions, dubbed a "Coulomb crystal"[134, 135]. Coulomb crystals can be utilized to determine the number of molecular ions present in the trap by measuring the fluorescence of the atomic ions, providing the overall crystal size[134, 136]. They can also provide information on reaction rates and the internal state distribution of the molecular ion[134, 136], examples of which can be seen in Figure 1.4.

A)



B)

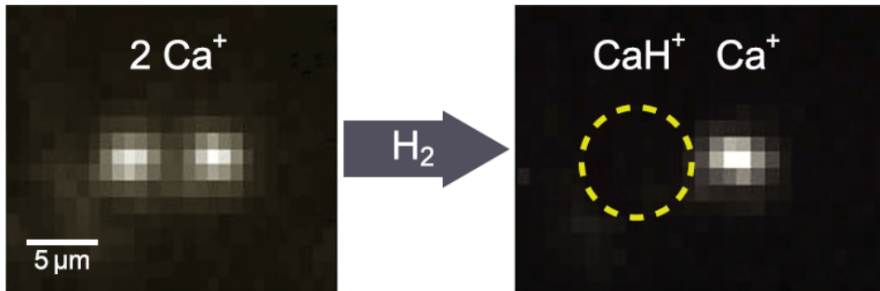


Figure 1.4: Coulomb crystals of sympathetically cooled  $^{40}\text{Ca}^+$  atoms.  $\text{CaH}^+$  is produced upon addition of  $\text{H}_2$  to  $^{40}\text{Ca}^+$ . This is indicated by depleted fluorescence on the left side of the crystal in A) (taken from Rugango *et al.*[137]) and the disappearance of the left  $^{40}\text{Ca}^+$  atom in B) (taken from Rugango *et al.*[138]).

The majority of the internal population remaining in the molecular ions after sympathetic cooling is largely confined to the vibrational and rotational energy levels. A series of investigations by Drewsen and co-workers have focused on further reducing the ground state ( $X^1\Sigma^+$ ) rotational population of  $\text{MgH}^+$  ions using sympathetically cooled  $\text{Mg}^+$  ions. Utilizing a rotational state optical pumping scheme[139], they have demonstrated the ability to trap  $\sim 37\%$  of the rotational population into the  $X^1\Sigma^+$  state of  $\text{MgH}^+$ , with an effective thermal distribution of  $\sim 20\text{K}$ [140]. Through the addition of helium buffer gas cooling to this experiment, they have can produce single  $\text{MgH}^+$  ions with an effective rotational temperature of  $\sim 7\text{K}$  [141].

Eric Hudson and co-workers have amended the method of sympathetic cooling utilizing laser cooled neutral atoms, as opposed to ions, to induce collisions[142]. This has the added benefit of achieving both sub mK translational temperatures and significant vibrational cooling as well. They demonstrated this technique by first generating  $\text{BaCl}^+$ , which is then vibrationally quenched by collisions with sympathetically cooled  $^{40}\text{Ca}$  atoms to confine  $\sim 90\%$  of the vibrational population to the ground state ( $X^1\Sigma^+$ )[143]. Theoretical calculations confirm the large degree of vibrational quenching observed experimentally[144].

Recently, while performing experiments on the barium methoxy cation ( $\text{BaOCH}_3^+$ ) sympathetically cooled by  $^{40}\text{Ca}$ , Hudson and co-workers recorded a mass spectrum indicating the presence of  $\text{CaOBa}^+$  within their linear ion (Paul) trap[145]. There is a strong precedent for this observation, as hypermetallic group IIA oxides (MOM) have been previously observed within our group while performing laser ablation experiments of both beryllium and calcium metals. Hypermetallic beryllium oxide,  $\text{BeOBe}$ , has been previously studied by our group using a wide array of spectroscopic techniques[146]. Under specific conditions their production by laser ablation (monitored using a time-of-flight mass (TOF) spectrometer) is quite strong, of comparable (or surpassing) intensity to other molecular species frequently observed (ex. metal

oxides, MO) in these experiments. The ability to readily produce large concentrations of small triatomic species such as these suggests they could be utilized as candidates for ultracold polyatomic molecules, as demonstrated by their observation in ongoing sympathetic cooling studies. However, in order to assess their viability as ultracold molecules the internal state distribution and structural characteristics of these species must first be examined. Unfortunately experimental and theoretical information on species of this nature is lacking. The spectroscopic characterization of molecules such as CaOCa (and their cationic equivalents) can provide internal state distribution data for the ultracold molecule community, which our group is well equipped to study. Additionally, these experiments are well in line with our groups primary research objective involving the study of unusual bonding mechanisms in group IIA metallic species[147].

Chapter 4 of this dissertation describes the spectroscopic investigations of the neutral species CaO, CaOH, and CaOCa created using laser ablation. Corresponding vibronic bands were detected using LIF. Studies of the neutral species preceded those of cations, as well known intermediates states of the neutral are needed to perform zero kinetic energy photoelectron (ZEKE) spectroscopy[148]. Jet-cooling was utilized to alleviate spectral congestion, which aided in spectroscopic assignment of vibronic bands observed experimentally (UV and near IR spectral regions). Electronic structure calculations for CaOCa were performed by one of our collaborators, Dr. Wafaa Fawzy. Results from the spectroscopic investigations are presented, along with future work for this project.

# Chapter 2

## Experimental Techniques

### 2.1 Cavity Ringdown Spectroscopy

Hebelin *et al.*[149] first introduced the idea of using an optical cavity for the measuring the reflectivity of mirror coatings in 1980. This was accomplished by modulating light intensity from a continuous wave (CW) laser into an optical cavity and measuring the phase shift of the laser as it exited the cavity. Anderson *et al.*[150] showed that the reflectivity of the mirrors could be measured with higher accuracy by shutting off the CW laser using an optical switch and recording the exponential decay of the light as it exited the cavity. In each of these techniques the frequency of the light injected into the cavity coincidentally mode matched with one of the narrow modes of the cavity.

These problems with coincidental mode matching were addressed by Deacon Research in late 1980's by replacing the CW laser with a pulsed laser source[151, 152]. The short laser pulses (ns) allow the injected light to behave less wave like and accordingly the interference within the cavity becomes random and independent of wavelength. This eliminates the need for laser shut off electronics, greatly simplifying the instrumental design. Deacon Research began selling this instrument for

the testing of high reflective mirrors under the commercial name Cavity Lossmeter, mostly to aerospace technology companies and national laboratories[152, 153]. They soon realized that this instrument could be utilized for the spectroscopic detection of molecules trapped in the cavity. O’Keefe and Deacon measured the forbidden  $b\ ^1\Sigma_g^+ \leftarrow X\ ^3\Sigma_g^-$  transition of  $O_2$  to demonstrate this capability[151]. This was soon followed by studies of the metal cluster species  $Cu_2$  and  $Cu_3$ [154] with this new technique, dubbed cavity ringdown spectroscopy (CRDS). Since its inception CRDS has proven to be a highly sensitive and robust spectroscopic technique, with applications in numerous fields such as: astrophysical chemistry, atmospheric chemistry, medical applications, and combustion chemistry[155].

A traditional absorption spectroscopy experiment involves passing light through a sample medium (solid, liquid, or gas) in order to determine the concentration of the absorbing species using the Beer-Lambert law,

$$I_t = I_0 e^{-\sigma LN} \quad (2.1)$$

where  $I_0$  is the initial light intensity,  $I_t$  is the intensity of the transmitted light,  $\sigma$  is the cross section of the absorbing species in  $cm^2$ ,  $L$  is the pathlength of the absorbing medium in  $cm$ , and  $N$  is the number density (concentration) of the absorbing species in  $cm^{-3}$ . The difficulty in traditional absorption experiments comes from limited sensitivity. In order to increase the detection limit two options are possible, the first being increasing the concentration of the species of interest while the second is increasing the absorption pathlength. Sample cells based on the designs by White[156] and Herriot[157, 158] take advantage of increased pathlength in order to improve absorption sensitivity. In each of these designs consist of two or more sets of reflective mirrors located on either end of the cavity. Light enters the cavity and bounces between the sets of mirrors multiple times (along a different path with

each reflection), passing through the absorbing medium multiple times. Typically the increased pathlength is on the order of tens of meters, but advanced configurations can achieve path lengths up to hundreds of meters[159]. These sample cells, typically referred to as multi-pass cells, follow a similar concept as CRDS.

This section focuses solely on the concept of the pulsed CRDS used in this dissertation. A standard pulsed CRDS experiment is shown below in Figure 2.1.

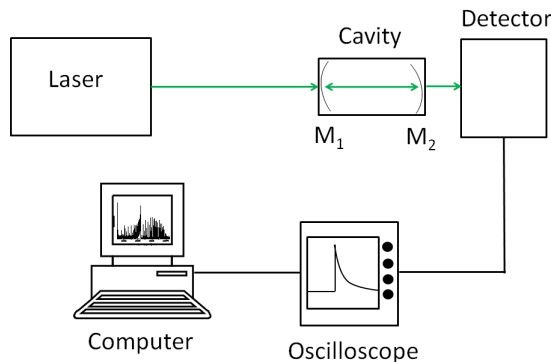


Figure 2.1: Simplified schematic for a pulsed CRDS experiment. The light from a pulsed dye laser (green lines) enters the optical cavity, and reflects between the mirrors many times, increasing the effective pathlength. The sample of interest is contained in the cavity between two highly reflective mirrors, labeled as  $M_1$  and  $M_2$ , respectively. The light which exponentially decays from the cavity is detected and recorded on a computer. This figure is taken from Sullivan[160].

In this schematic, pulsed laser light enters one end of a high Q optical cavity with mirrors on each end with reflectivity,  $R, \geq 99.9\%$ . Since the mirrors have such a high reflectivity, only a small amount of light enters the cavity. The light that enters the cavity bounces back and forth between each mirror thousands of times, increasing the path length. A tiny amount of light decays from the cavity exponentially with each reflection from the mirrors (with identical reflectivity,  $R$ ). Assuming an empty cavity with length,  $L$ , the intensity of the light within the cavity can be detected as

a function of time by the equation[161]

$$I_t = I_0 \exp\left(- (1 - R) \frac{tc}{L}\right) \quad (2.2)$$

which shows that the rate of exponential decay of light from the cavity is determined by the loss of mirrors per reflection (1-R) and also the number of round trips (n) after time t, given by

$$n = \frac{tc}{2L} \quad (2.3)$$

where c is the speed of light within the optical cavity[159, 161].

Consider the addition of an sample species to the cavity. This species will absorb radiation at specific wavelengths dictated by the absorption cross section, as described in Equation 2.1. The absorption loss ( $AL$ ) within the cavity per round trip[161] is

$$AL = (2\alpha L) \left(\frac{tc}{2L}\right) \quad (2.4)$$

where  $\alpha$  is equal to the absorption coefficient equal to  $\sigma N$  in Equation 2.1. The total loss ( $TL$ ) is equal to the loss in the empty cavity plus the loss due to absorption, seen in Equation 2.5 below[161].

$$TL = [(1 - R) + \alpha L] \left(\frac{tc}{2L}\right) \quad (2.5)$$

Accounting for the total loss Equation 2.2 is then re-written as[159, 161]

$$I_t = I_0 \exp\left(- (1 - R + \alpha L) \frac{tc}{L}\right). \quad (2.6)$$

The time it takes for the light to exponentially decay from the cavity as a function of

$1/e$  is called the ringdown time ( $\tau$ ), and is defined by the following equation[159]

$$\tau = \frac{L}{c(1 - R + \alpha(\nu))} \quad (2.7)$$

where  $\alpha(\nu)$  is the frequency dependent absorption coefficient for a sample species within the cavity[159].

As an example, assume there is a ringdown cavity that is one meter long with a set of mirrors on each end with a reflectivity of 99.9985% , with no absorbing species present. Using Equation 2.7 the maximum ringdown time of this cavity is 222  $\mu s$ . Next, an absorbing species is added to the cavity with an absorption coefficient,  $\alpha = 3 \times 10^{-5} \text{ m}^{-1}$ . Using Equation 2.7 again the ringdown time is reduced to 74  $\mu s$  due to the presence of an absorbing species within the cavity. These curves can be seen in Figure 2.2.

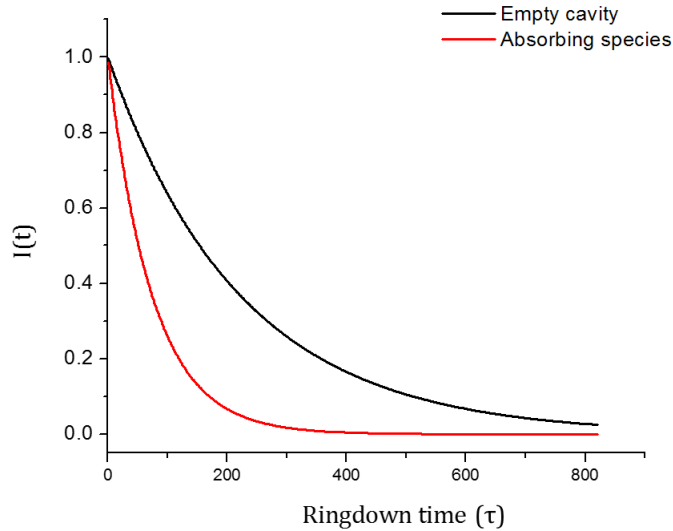


Figure 2.2: Theoretical ringdown curves simulated for an empty cavity ( $\tau = 222 \mu s$ ) and with an absorbing species ( $\tau = 74 \mu s$ ) present.

The absorption coefficient of a species present with the cavity can be calculated using the equation

$$\alpha = \frac{1}{c} \left( \frac{1}{\tau_1} - \frac{1}{\tau_2} \right) \quad (2.8)$$

where  $\tau_1$  is the ringdown time for the cavity with an absorbing species and  $\tau_2$  is the ringdown time for an empty cavity[161]. If both ringdown times are measured, an absorption spectrum can be obtained using a tunable radiation source.

The main advantage of CRDS is the increased sensitivity due to the large effective path length. Using the example from Figure 2.2, if the theoretical ringdown time is 222  $\mu\text{s}$ , then the corresponding path length is 66 kilometers (using Equation 2.3). The other significant advantage is that CRDS is largely independent of shot-to-shot noise variations in the pulsed laser. This noise will only affect the intensity of ringdown signal but not the decay rate of light exiting the cavity.

## 2.2 Laser Induced Fluorescence

The invention of the laser in 1960 by Maiman[162] has had a tremendously profound effect on the spectroscopic community. Indeed, a vast majority of spectroscopic techniques in use today would be fundamentally impossible without it. The development of a coherent light source made it possible to probe individual quantum states of atoms and molecules alike. Richard Zare was the first to utilize the laser as a means of probing and observing electronically excited states of a molecular species in 1968, a term quickly coined as laser induced fluorescence (LIF). In this experiment Zare used a He-Ne laser (632.8 nm) to probe excited vibronic states of the potassium dimer ( $\text{K}_2$ ) which subsequently relax back to its ground electronic state[163]. Other LIF experiments followed with fixed frequency laser sources such as the He-Ne and argon ion laser. The advent of the dye laser by Spaeth[164], Sorokin[165] and Schäfer[166] greatly extended the capability of LIF (and many other spectroscopic methods) by providing the ability to probe molecular transitions over a broad energy range. LIF has since been used as an effective tool to study a wide array of atomic and molecular species of interest to the fields of chemistry, physics, biology

and astronomy[68, 167].

The concept of LIF is quite simple. Consider the energy level diagram below.

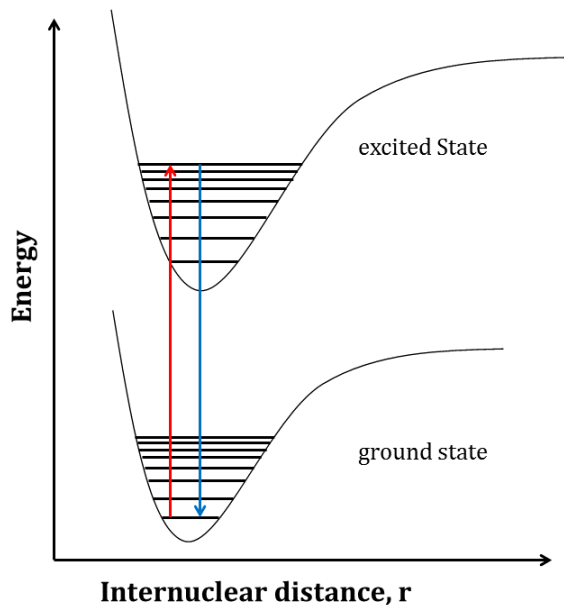


Figure 2.3: Energy level diagram depicting the process of LIF. Using a laser source, a photon is promoted to an excited electronic state (red arrow) and subsequently fluoresces down to a lower state (blue arrow).

A laser is used to excite an electron to an upper electronic state by absorption of a photon. The electron then fluoresces back down to some lower state, re-emitting a photon in the process. The observed molecular transitions due to fluorescence are recorded using a detector, typically a photomultiplier tube (PMT). By stepping the laser in frequency space, one can obtain a complete spectrum of the molecular species in question.

LIF is a powerful technique, as the only requirement for a molecule to fluoresce is that the upper state being probed must possess a significant quantum yield for emission. Also, since detection is limited to fluorescing species it is essentially a background free technique. As such, it is a highly sensitive technique enabling detection limits down to a single molecule[167].

## 2.3 Supersonic Expansion

One of the main difficulties associated with high resolution spectroscopy is the amount of spectral overlap that arises from a molecular species with a high density of states. This can result in severe spectral congestion which limits the ability to differentiate between overlapping bands of a single molecular species, or overlap from bands of multiple molecular species. This in turn inhibits the ability to extract meaningful molecular constants from a transition/species of interest. One way to circumvent this problem is through the use of a technique commonly referred to as a supersonic expansion, which reduces the internal state population (i.e. lower rotational and translational temperature) of the desired species. This alleviates the degree of spectral congestion observed experimentally, which greatly aids in spectroscopic analysis for many species.

In order to describe a supersonic expansion source, first consider an effusive beam[168]. An effusive beam source consists of two parts. The first of these is a high pressure gas reservoir, with an orifice designed to allow a gas sample to pass through into a high vacuum chamber. The second are a series of apertures to collimate the effusive flow, which is required to convert and direct the randomized molecular flow into a beam. The effusive beam is one of the earliest examples of a molecular beam[169]. The orifice in an effusive beam is small, such that

$$D \ll \Lambda_0 \tag{2.9}$$

where  $D$  is the diameter of the orifice, a circular orifice in this case (i.e. pinhole), and  $\Lambda_0$  is the mean free path for collisions between atoms or molecules that pass through the pinhole. In an effusive beam there are no collisions within or downstream from the pinhole. The molecules within the reservoir have a Maxwell-Boltzmann distribution of velocities. This velocity distribution of the molecular beam does not change after it

exits the pinhole into the vacuum chamber. Since there is no change in the distribution of the internal molecular states, no cooling of the molecule within the beam occurs.

Kantrowitz and Grey were the first to suggest the idea of supersonic expansion in 1951[170]. By either increasing the diameter of the pinhole (typically on the order of  $\mu\text{m}$ ) or the pressure (typically on the order of several atmospheres) such that

$$D \gg \Lambda_0 \tag{2.10}$$

then numerous collisions will occur both within and after the pinhole. These collisions converts the random motions of species into a directed mass flow. The range of velocities of molecules within the beam is narrowed and the overall peak velocity of the molecules is increased due to the increased flow. By converting the random motion of the species within the beam to a more directed flow, the effective translational temperature of the beam becomes very low, on the order of 1 K[171, 172]. This is because particles traveling in the beam have a small velocity compared to the rest of the neighboring particles, and thus few collisions between particles occur. Translational cooling continues downstream of the pinhole and in this region the flow is defined as hydrodynamic. When the flow is no longer hydrodynamic, collisions no longer occur and there is no further decrease in translational temperature. At this point, the beam behaves similarly to an effusive beam[171, 173].

The term supersonic arises due to the relationship between the increased mass flow velocity,  $u$ , and the local speed of sound,  $a$ . This relationship can be seen in the equation,

$$M = \frac{u}{a} \tag{2.11}$$

where the local speed of sound,  $a$ , is defined as

$$a = \left( \frac{\gamma k T_{tr}}{m} \right)^{1/2} \tag{2.12}$$

where  $m$  is the mass of the gas particles, and  $\gamma$  is equal to

$$\gamma = \frac{C_P}{C_V} \tag{2.13}$$

where  $C_P$  and  $C_V$  are the heat capacities at constant pressure and volume, respectively. Typically the gases used in supersonic expansions are helium and argon, for which the value of  $\gamma$  is 5/3. The Mach number in a supersonic expansion can be extremely high (hence the term supersonic), on the order of 100 or more[171, 173].

The majority of cooling that occurs in a supersonic expansion comes from the cooling of the translational degree of freedom. However, rotational and vibrational cooling occur as well. The level of rotational and vibrational cooling are dependent on the rate at which these degrees of freedom reach equilibrium with the translational degree of freedom. Typically the rate of equilibration between rotational and translational degrees of freedom occurs quickly, before the molecules enter the collision free region of the expansion. Since the efficiency of rotational cooling is less efficient, the rotational temperature is typically higher than the translational temperature, around 10 K. Equilibration between the translational and vibrational degrees of freedom are slower still, and temperatures can be much higher, typically around 100 K depending on the nature of vibration within the molecule[171].

It should be noted that since no collimating apertures are present in these studies to control the downstream flow past the pinhole, this source is forms a free jet expansion[173, 174]. Several other designs for supersonic sources are covered extensively in the literature, such as the slit source. An extensive review of supersonic beam sources by Michael Morse[174] covers these concepts in extensive detail.

# Chapter 3

## Cavity Ringdown Spectroscopy of Polycyclic Aromatic Hydrocarbons (PAHs)

### 3.1 The Phenoxy Radical

#### 3.1.1 Introduction

The phenoxy radical is an important intermediate in the high temperature oxidation of several small aromatic hydrocarbons[65, 175, 176, 177]. The reaction of atomic oxygen with benzene, for example, at high temperature leads to the formation of phenol which in turn then forms the phenoxy radical through either unimolecular decomposition or bimolecular reactions with atomic and radical species[65, 175, 177]. Similarly, the reaction of the phenyl radical with O<sub>2</sub> at high temperatures (T > 1,000 K) leads to the formation of the phenoxy radical plus atomic oxygen[61, 62, 63, 178],



followed by decomposition of the phenoxy radical to the cyclopentadienyl radical with carbon monoxide



at  $T > 900$  K[65, 179]. This reaction forms a competing pathway with the polymerization of phenyl radicals via the HACA mechanism to produce PAHs[178],



which are believed to be the precursors of soot formation in hydrocarbon combustion[35, 37, 46, 180].

Due to its importance in combustion chemistry, the phenoxy radical has been the subject of numerous experimental and theoretical studies over the years. Several kinetics studies have been performed on the reaction of the phenoxy radical with various species, including:  $\text{CH}_3$ [66],  $\text{O}_2$ [181, 182],  $\text{O}_3$ [183],  $\text{NO}$ [181, 184], and  $\text{NO}_2$ [181]. These studies employ monitoring of broadband transitions in the UV and visible regions.

The symmetry species of the ground electronic state has been difficult to assign, where  $\text{A}_1$ [185],  $\text{A}_2$ [186], and even  $\text{B}_2$ [187] designations are reported in the literature. It is now generally accepted that the ground electronic state of the phenoxy radical has  $\text{B}_1$  symmetry, with a planar geometry[188, 189, 190, 191, 192]. EPR studies show that the unpaired electron in the ground state is delocalized from the oxygen onto the  $\pi$  orbitals of the carbon ring, indicating the the CO bond has double bond character[193, 194, 195, 196, 197, 198]. A nearly complete set of ground state vibrational frequencies for the phenoxy radical have been determined using resonance Raman spectroscopy[186, 199, 200, 201, 202, 203, 204, 205] and matrix-isolation polarized FTIR spectroscopy[188].

The electronic spectrum of the phenoxy radical was first reported in 1955 by Porter

and Wright through a flash photolysis study of anisole, with two bands appearing in the UV region centered around 300 and 400 nm, respectively[206]. Ward observed four broad bands in the visible region, near 600 nm, spaced approximately  $500 \text{ cm}^{-1}$  from each other[207]. This transition was assigned as  $n - \pi^*$ , where  $n$  denotes a non-bonding orbital. Pullin and Andrews later recorded these absorption bands in an argon matrix[208], but neither they nor Ward were able to make any definitive vibrational assignments. A theoretical study (CAS-MCSCF/CI) by Takahashi *et al.*[191] assigned this electronic transition,  $\tilde{B}^2A_2 \leftarrow \tilde{X}^2B_1$ , as  $n - \pi^*$  in agreement with the previous study by Ward. However several conflicting studies exist in the literature concerning this assignment. These include a flash photolysis study of the 600 nm absorption band of the phenoxy radical coupled with CASSCF calculations by Johnston *et al.*[187], an *ab initio* study of the fundamental vibrational bands of the phenoxy radical using the UNO-CAS method by Chipman *et al.*[190], an *ab initio* study of the thermal decomposition mechanism of the phenoxy radical by Liu *et al.*[192], and finally a UV-VIS/IR polarization spectroscopy study of the four electronic bands of the phenoxy radical in an argon matrix by Radziszewski *et al.*[209] who each assigned this transition as  $\pi - \pi^*$ [209].

Despite the extensive number of studies performed on the  $\tilde{B}^2A_2 \leftarrow \tilde{X}^2B_1$  transition of the phenoxy radical, it would be advantageous to examine these bands in greater detail in order to elucidate the origin of this transition as  $n - \pi^*$ ,  $\pi - \pi^*$ , or some other assignment. Electronic structure calculations indicate that this band progression arises from a totally symmetric in-plane CC stretching/bending mode, with a vibrational frequency of roughly  $500 \text{ cm}^{-1}$ [190, 191]. While DFT calculations have been shown to produce an accurate contour fit of these vibronic bands[210], they are still quite broad at room temperature. The use of a supersonic jet can be used to relieve spectral congestion in order to aid spectral assignments. A sensitive detection method is highly desirable for gas phase studies of the phenoxy radical, as typical

methods used to generate these types of radicals have low production efficiencies (i.e. electrical discharge or photolysis). CRDS has been effectively utilized as a detection method of the UV/visible electronic bands of the phenoxy radical[66, 184], as well as the symmetry forbidden but vibronically allowed  $\tilde{A} \ ^2B_2 \leftarrow \tilde{X} \ ^2B_1$  transition of the phenoxy radical located in IR region[211]. In our group we have utilized a discharge slit expansion source coupled with CRDS to record rotationally resolved spectra for the  $1 \ ^2B_1 \leftarrow \tilde{X} \ ^2A_1$  transition of the phenyl radical[74]. This experimental apparatus was used to study the phenoxy radical. However this work remains unpublished as we were unable to definitively assign one of the vibronic bands observed experimentally. Due to unforeseen complications, additional experiments were not possible. In 2015 Araki *et al.* published a gas phase study of the  $\tilde{B} \ ^2A_2 \leftarrow \tilde{X} \ ^2B_1$  transition of the phenoxy radical using CRDS at room temperature which agrees with our vibronic band assignments[212].

This section details the first gas phase jet-cooled study of the phenoxy radical using CRDS. Absorption spectra were recorded over the 15,750 - 17,500  $\text{cm}^{-1}$  region. A progression of four vibronic bands were observed which have been assigned to the  $\tilde{B} \ ^2A_2 \leftarrow \tilde{X} \ ^2B_1$  transition of the phenoxy radical. These experimental studies were complemented with TD-DFT calculations in order to aid in the vibronic assignments and to address the nature of  $\pi$  bonding in this system.

### 3.1.2 Methods

The experimental setup utilized for the spectroscopic study of both the phenoxy and phenylperoxy radicals has been previously described by Freel *et al.*[74] and Freel[213]. As such the reader is directed to these sources for any experimental details not listed in this dissertation.

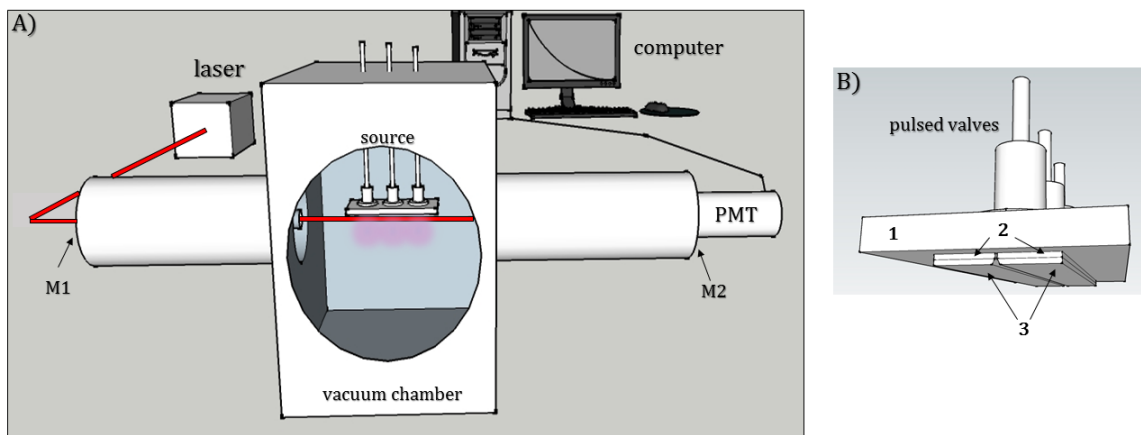


Figure 3.1: Experimental setup designed for detection of radical intermediates in soot formation. The overall setup is shown in A. The expansion/discharge source is enlarged in B) for additional detail. In this enlargement, 1) is the ground plate, 2) is the phenolic insulator, and 3) is the high voltage jaw over which the discharge is created. This figure has been adapted from Freel *et al.*[74].

The vacuum chamber used for these experiments (MDC Vacuum Corp.) was a 6-way cross design equipped with precision optical mounts at the ends of two large baffle arms to hold the cavity ringdown mirrors, creating an optical cavity 1 meter long. Two sets of mirrors were used to cover the largest possible range of the  $\tilde{B}^2A_2 \leftarrow \tilde{X}^2B_1$  transition of the phenoxy radical. Both sets of mirrors have a 6 m radius of curvature designed to correct for beam divergence. One set of mirrors (CRD Optics Inc.) had a reflectance of 99.9985% at their center wavelength, 620 nm, with a 30 nm bandwidth. Ringdown times of up to  $\sim 220 \mu\text{s}$  were observed with an empty cavity. The other set of mirrors (Los Gatos) were 99.995% reflective at their center, 570 nm, with a 40 nm bandwidth. For these mirrors, ringdown times of up to  $\sim 40 \mu\text{s}$  were observed with an empty cavity. During operation, ringdown times were reduced due to deposit of discharge products on the mirrors. In order to limit this effect, a small flow of Ar or He was passed over each mirror inside the baffle arms. Additionally,

sets of metal washers were placed inside each baffle arm to further limit this effect. The vacuum chamber was evacuated using a 500 CFM Roots blower (Leybold, WSU 1001), with pressures averaging around 15-60 mtorr with the purge gas flowing.

Light from a tunable dye laser (Lambda Physik, FL3002) pumped by a XeCl excimer laser (Lambda Physik, EMG201) was used to probe vibronic transitions of phenoxy. The pulse duration of the laser was 10 ns, operating at frequency of 10 Hz. The output power of excimer light was typically anywhere between 200-250 mJ. For these experiments a variety of laser dyes were used, including: Coumarin 540A, Rhodamine 590 and Rhodamine 610. Output power of the dye laser ranged from .1 - 2 mJ/pulse. The linewidth of the dye laser is  $0.2 \text{ cm}^{-1}$  at full width half maximum (FWHM). No intracavity etalon was incorporated for these experiments.

Light exiting the cavity was detected using a photomultiplier tube PMT (Hamamatsu R889). The signal output from the PMT was captured using a 16 bit, 10 MS/s GageScope A/D card installed on a personal computer. A custom LabVIEW program, developed by Dr. Keith Freel, was used to control the experiment and to record ringdown times. Typical scans were collected using 10-15 averaged pulses per wavelength point in order to reduce error in the ringdown decay time between pulses. Multiple scans were collected and co-averaged in such a case wherein additional noise reduction was required.

The electrical discharge assembly, shown in Figure 3.1 B), was based on previous designs by Linnartz *et al.*[214] and Biennier *et al.*[215]. Three pulsed solenoid valves (Parker Hannifin, Series 9) were attached to the front of a 1.0 cm thick aluminum plate with three 0.8 mm pinholes to provide a channel for gas pulses to expand into the vacuum chamber. Flow rates of the pulsed valves were largely inconsistent over time due to variations in the discharge source, gas concentration, etc. which required frequent re-adjustments to compensate for day-to-day inconsistencies in gas flow. Alternatively all interior valve components could be removed to create a continuous

expansion source. A new faceplate was designed for the continuous expansion with narrowed pinhole widths of 0.5 mm in order to reduce the increased gas load into the vacuum chamber. While the cooling efficiency was reduced by switching to a continuous expansion source, the flow rates were more stable over time.

It should be noted that in Figure 3.1 three pulsed valves are shown. One of the pulsed valves malfunctioned during operation, and was subsequently removed from the source. Results presented in this section were collected using two pinholes for both pulsed valved and continuous flow.

The plate and pulsed valves were electrically grounded. Metal strip electrodes (also referred to as high voltage jaws) and grounding plates were mounted onto the valve plate to confine the pinhole expansion between a slit discharge assembly. Phenolic spacers (1 mm thick) provided insulation between the valve mounting plate and the ground plates. An additional set of phenolic spacers were placed between the ground plates and the high voltage jaws. The discharge plates (80 mm in length) formed a slit with a width of 0.8 mm for supersonic expansion. The electrical current was carried across the outer electrodes (negatively charged) and aluminum plate (ground). The current passed through the highest concentration of gas density, which could be varied by adjusting both the backing pressure and/or the opening time of pulsed valves. The high voltage source for these experiments was a Stanford Research Systems high voltage power supply (Model: VS325). The discharge was pulsed using a PVX-4140 Pulse Generator (Directed Energy, Inc.) which was controlled using a delay generator (Stanford Research Systems, DG535). This delay generator was also used to control the timing between the laser and pulsed valves. The electrical discharge was operated with a pulse duration of 2 ms. Ringdown measurements were collected after the discharge had stabilized, approximately  $\sim 300\text{-}400 \mu\text{s}$  after the discharge onset. After the ringdown time was recorded, the high voltage was switched off. For experiments performed using the pulsed valves, the valves were open for a duration

of 500  $\mu\text{s}$  (after the discharge had stabilized). For additional details on the electrical discharge assembly, see the aforementioned references by Freil *et al.*[74] and Freil[213].

Anisole ( $\text{CH}_3\text{OC}_6\text{H}_5$ , Aldrich, anhydrous, 99.7%) was utilized as the radical precursor. Argon carrier gas was passed over the surface of the precursor. The precursor and gas lines were heated to approximately 70° C to increase the partial pressure of anisole. The pressure of the carrier gas (0.8 atm) carried approximately 5% of anisole at 70° C. The following conditions produced the largest concentration of phenoxy radicals: low ballast resistance (1k  $\Omega$ ) and high voltage (1 kV), which in turn produced  $\sim 220$  mA current when the discharge was on. A probe beam detection distance of 6 mm from the exit of the nozzle provided the highest sensitivity for radical detection while maintaining low rotational temperatures ( $\sim 20\text{K}$  with pulsed valves,  $\sim 45$  K with continuous expansion). Spectral calibrations were obtained using both metastable argon and  $\text{C}_2$  absorption features.

### 3.1.3 Experimental Results

The observed spectrum ( $\sim 571\text{-}633$  nm) of jet-cooled anisole discharge products observed using cavity ringdown spectroscopy is shown in Figure 3.2 on the next page. The broad features present were assigned to the  $\tilde{\text{B}}^2\text{A}_2 \leftarrow \tilde{\text{X}}^2\text{B}_1$  transition of the phenoxy radical. The weak origin band is centered at  $\sim 15,860$   $\text{cm}^{-1}$ . To the blue of the origin band is a  $516$   $\text{cm}^{-1}$  progression of vibronic bands. Red shaded peaks can be seen on each shoulder of the vibronic bands, roughly  $60$   $\text{cm}^{-1}$  from the peak. The  $16,600 - 17,513$   $\text{cm}^{-1}$  region was recorded with the pulsed valve configuration. For the remainder of the observed spectrum ( $15,758 - 16,600$   $\text{cm}^{-1}$ ), the continuous expansion source was used instead due to erratic gas flow rates. This erratic performance was caused by frequent deformation of the teflon pulsed valve poppets. This caused instability in the discharge and therefore variations in the radical production. The spectrum in this region was recorded with the continuous flow configuration,

which provided better discharge stability and allowed for greater reproducibility for spectral averaging. Computational results were needed to make definitive vibronic band assignments due to the diffuse nature of the observed features. These results will be outlined in the following subsection.

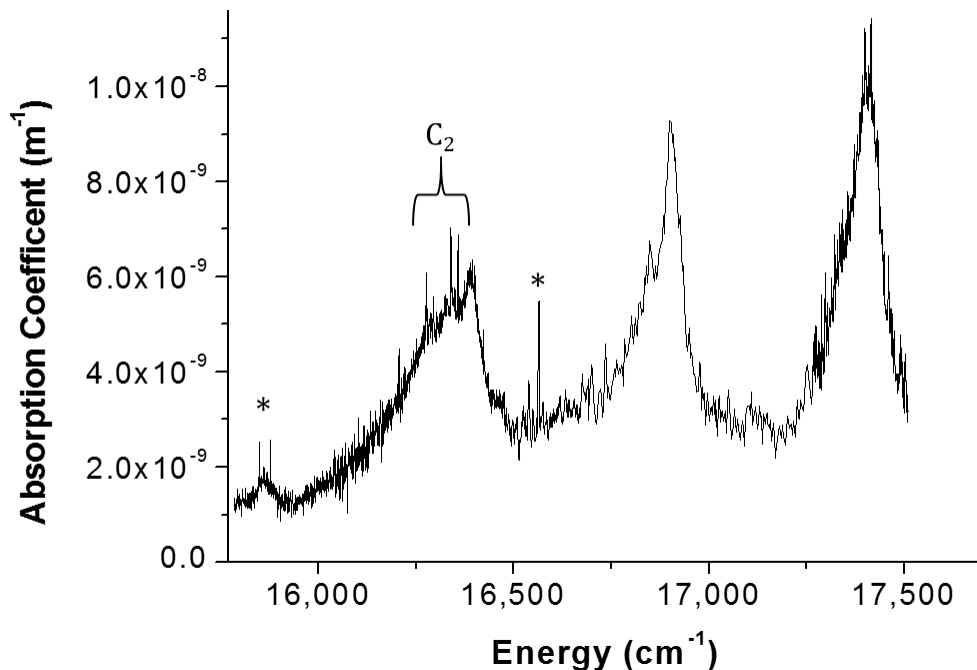


Figure 3.2: CRDS absorption spectrum of jet-cooled anisole discharge products. The features marked with \* arise from metastable argon created in the electrical discharge.

A slow baseline increase was observed throughout the spectrum due to broadband absorption and/or scattering losses. The change in ringdown time is also affected by decreasing/increasing mirror reflectivity as a function of wavelength. The absorption coefficient,  $\alpha$  ( $\text{cm}^{-1}$ ), was calculated at each measured wavelength using the equation

$$\alpha = \frac{L}{lc} \left( \frac{1}{\tau_1} - \frac{1}{\tau_2} \right) \quad (3.4)$$

which is a modified form of Equation 2.8 needed to account for the difference between the effective single pass absorption path length ( $l = 0.08$  m) and the total cavity length ( $L = 1$  m). Additionally,  $\tau_1$  is measured ringdown time with the laser passing

through the discharge and  $\tau_2$  is the background ringdown time including broadband absorption/scattering losses in the expanding gas without the electrical discharge.

Several features in Figure 3.2 are attributed to the well known Swan Bands of  $C_2$ . These features increased as the discharge voltage increased. A similar relationship was observed for the vibronic bands of the phenoxy radical. In the pulsed valve configuration, the intensity of the 0-0 band of  $C_2$  was compared with PGOPHER simulations to determine the efficiency of rotational cooling in the expansion ( $T_{\text{rot}} \sim 30$  K). The cooling efficiency of the continuous expansion was determined by performing a rotational contour fit of the phenyl radical at 505.1 nm[74], using bromobenzene as the precursor ( $T_{\text{rot}} \sim 45$  K). The level of vibrational cooling was not as efficient, where the vibrational temperature of  $C_2$  in the continuous expansion was nearly 5,000 K. The level of vibrational cooling for larger molecules could not be determined. Peaks from metastable argon, arising from the  $3s^23p^5 \left( {}^2P_{1/2}^{\circ} \right) 4p$  and  $3s^23p^5 \left( {}^2P_{3/2}^{\circ} \right) 4p$  states, proved to be an excellent calibration source[216].

### 3.1.4 Theoretical Calculations

Theoretical calculations were used to supplement the analysis of the observed vibronic transitions. These calculations were performed using the Gaussian 09 computational package[217]. The ground state geometry optimization, electronic structure, and harmonic vibrational frequencies were calculated using the UB3LYP hybrid DFT method. The corresponding information for the excited electronic state was calculated using time-dependent density function theory (TD-DFT). Dunning’s cc-pVDZ and aug-cc-pVTZ basis sets were utilized for both ground and excited electronic states[218]. For the geometry optimizations tight convergence criteria were used. The vertical excitation energy and oscillator strength were also calculated for the  $\tilde{B} \ ^2A_2 \leftarrow \tilde{X} \ ^2B_1$  transition. The phenoxy radical is planar, with  $C_{2v}$  symmetry in both the  $\tilde{B} \ ^2A_2$  and  $\tilde{X} \ ^2B_1$  states. Consistent with previous studies[189, 190, 209], the molecule

was oriented in the  $yz$  plane with the  $C_2$  axis coinciding with the  $z$ -axis. The  $\sigma_v$  plane is the  $xz$  plane while the  $\sigma'_v$  is the  $yz$  plane. The rotational  $a$ ,  $b$ , and  $c$  axes coincide with the  $z$ ,  $y$ , and  $x$  axes, respectively.

The molecular orbitals determined from the calculations are shown in Figure 3.3. In the electronic ground state the lone electron is located in the 25<sup>th</sup> molecular orbital (MO). This singly occupied molecular orbital (SOMO) has  $B_1$  symmetry, which is best described as a delocalized  $\pi$  orbital with nodes at the  $C_1$ -O bond and in between the  $C_2C_3$  /  $C_5C_6$  bonds, with bonding character along the  $C_3C_4C_5$  and  $C_6C_1C_2$  bonds. These findings are consistent with a previous study by Cheng *et al.*[189].

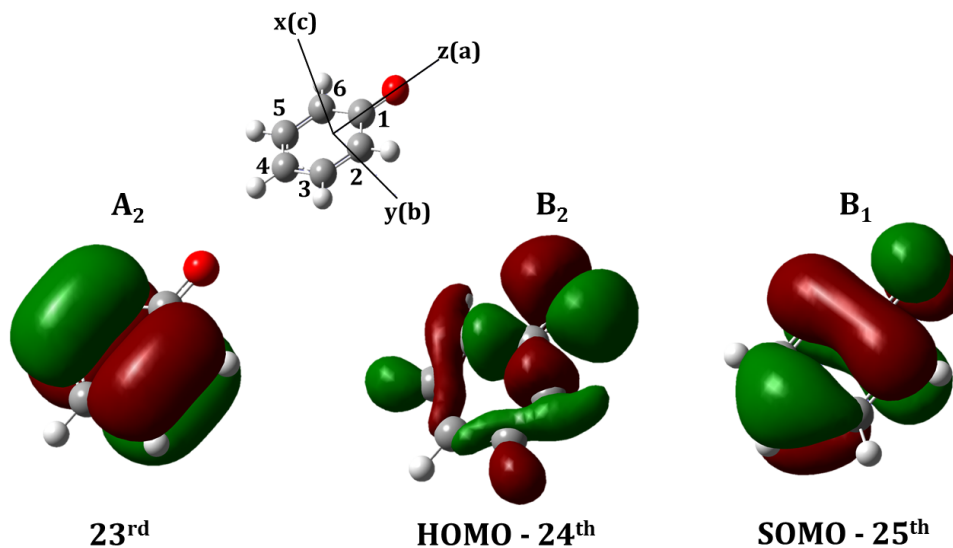


Figure 3.3: Molecular orbitals involved in the first two electronic transitions of the phenoxy radical calculated at the UB3LYP/aug-cc-pVTZ level for the ground electronic state,  $\tilde{X} B_1$ . Plots were generated with an isodensity value of 0.02 au.

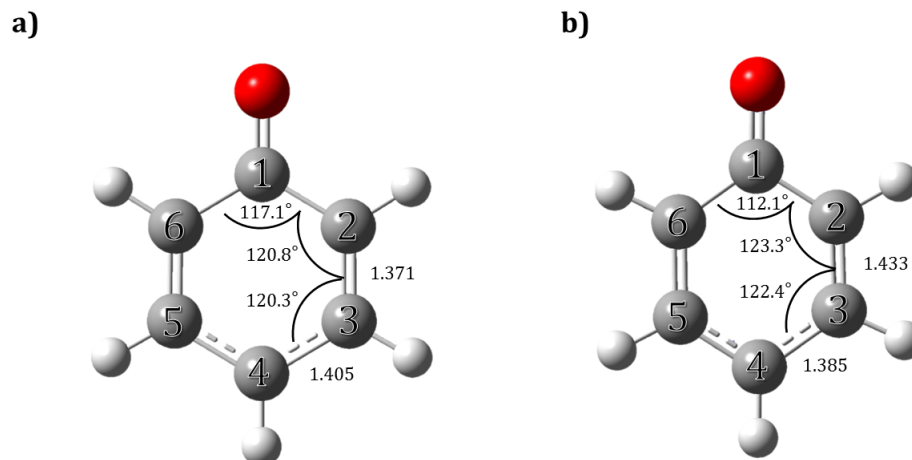


Figure 3.4: Equilibrium bond lengths ( $\text{\AA}$ ) and bond angles for the phenoxy radical calculated at the UB3LYP/aug-cc-pVTZ level for (a)  $\tilde{X} \ ^2B_1$  and (b) by TD-DFT/aug-cc-pVTZ for  $\tilde{B} \ ^2A_2$ .

The calculated equilibrium structure and geometric parameters for both the ground and excited states are listed in Figure 3.4 and Appendix A.1, respectively. The calculated C=O bond length in the ground electronic state is 1.252  $\text{\AA}$  at the UB3LYP/aug-cc-pVTZ level of theory. This agrees well with Chen *et al.*[189], who noted that this value is similar to CO double bonds for various ketone and aldehyde species (1.215  $\text{\AA}$  for acetone, 1.205  $\text{\AA}$  for formaldehyde, 1.191  $\text{\AA}$  for cyclopropanone, 1.202  $\text{\AA}$  for cyclobutanone, 1.225  $\text{\AA}$  for *p*-benzoquinone, 1.216  $\text{\AA}$  for acetaldehyde, and 1.202  $\text{\AA}$  for acetic acid)[219, 220]. The CC bonds within the ring deviated from typical benzene character, where the CC bonds are all equal to 1.397  $\text{\AA}$ [220]. The CC bonds for C<sub>1</sub>C<sub>2</sub>, C<sub>2</sub>C<sub>3</sub>, and C<sub>3</sub>C<sub>4</sub> were 1.448, 1.371, and 1.405  $\text{\AA}$ , respectively, at the UB3LYP/aug-cc-pVTZ level of theory. These values are close to experimentally determined CC bond lengths in *p*-benzoquinone (1.477  $\text{\AA}$ , 1.322  $\text{\AA}$ , and 1.477  $\text{\AA}$ ) which have been described as an alternating chain (single-double) of CC bonds[219]. The rotational constants in the ground state predicted by calculations were  $A'' = 0.18501 \text{ cm}^{-1}$ ,  $B'' = 0.093459 \text{ cm}^{-1}$ , and  $C'' = 0.062093 \text{ cm}^{-1}$ . The calculated ground state harmonic vibrational

frequencies, which agree well with values determined by Chen *et al.*[189], have been scaled by the recommended value of 0.967[221] and are listed in Table 3.1.

Table 3.1: Calculated vibrational frequencies ( $\text{cm}^{-1}$ ) for the phenoxy radical in the ground electronic state,  $\tilde{X}^2B_1$ . Calculations were performed at the B3LYP level of theory.

Mode	Sym.	cc-pVDZ	aug-cc-pVTZ
$\nu_1$	A <sub>1</sub>	3,102	3,094
$\nu_2$	A <sub>1</sub>	3,091	3,084
$\nu_3$	A <sub>1</sub>	3,070	3,063
$\nu_4$	A <sub>1</sub>	1,542	1,534
$\nu_5$	A <sub>1</sub>	1,437	1,432
$\nu_6$	A <sub>1</sub>	1,367	1,373
$\nu_7$	A <sub>1</sub>	1,114	1,128
$\nu_8$	A <sub>1</sub>	978	977
$\nu_9$	A <sub>1</sub>	946	957
$\nu_{10}$	A <sub>1</sub>	782	780
$\nu_{11}$	A <sub>1</sub>	511	514
$\nu_{12}$	A <sub>2</sub>	958	962
$\nu_{13}$	A <sub>2</sub>	784	781
$\nu_{14}$	A <sub>2</sub>	369	368
$\nu_{15}$	B <sub>1</sub>	974	973
$\nu_{16}$	B <sub>1</sub>	903	905
$\nu_{17}$	B <sub>1</sub>	781	782
$\nu_{18}$	B <sub>1</sub>	639	634
$\nu_{19}$	B <sub>1</sub>	472	465
$\nu_{20}$	B <sub>1</sub>	188	182
$\nu_{21}$	B <sub>2</sub>	3,099	3,091
$\nu_{22}$	B <sub>2</sub>	3,077	3,069
$\nu_{23}$	B <sub>2</sub>	1,498	1,496
$\nu_{24}$	B <sub>2</sub>	1,395	1,399
$\nu_{25}$	B <sub>2</sub>	1,300	1,296
$\nu_{26}$	B <sub>2</sub>	1,230	1,236
$\nu_{27}$	B <sub>2</sub>	1,118	1,126
$\nu_{28}$	B <sub>2</sub>	1,047	1,055
$\nu_{29}$	B <sub>2</sub>	576	577
$\nu_{30}$	B <sub>2</sub>	429	432

The electronic structure calculations predicted that the first electronic transition occurs by promotion of an electron from MO 24, which was a doublet with B<sub>2</sub> symmetry, to the SOMO (see Figure 3.3). This transition (symmetry forbidden) was predicted to appear in the IR region, consistent with previous theoretical[189] and experimental[211] studies by Cheng and co-workers. The second electronic transition occurs by promotion of an electron from MO 23 to the SOMO, which was a doublet with A<sub>2</sub> symmetry. The calculated vertical excitation energy for this transition (aug-cc-pVTZ basis set) was 2.3484 eV (527.96 nm or 18,940 cm<sup>-1</sup>) with a weak oscillator strength (f=0.0048). MO 23 is best described as a bonding  $\pi_x$  orbital with population density centralized over the C<sub>2</sub>C<sub>3</sub> and C<sub>5</sub>C<sub>6</sub> carbons, similar in character to one of the doubly degenerate HOMO's of benzene with e<sub>1g</sub> symmetry. As noted previously, geometrical parameters for the  $\tilde{B}^2A_2$  excited state can be seen in Figure 3.4 and Appendix A.1. Minimal change in the C=O bond length was noted upon excitation. The largest change in carbon-carbon bond distance occurs along the C<sub>2</sub>C<sub>3</sub> bond, from 1.380 to 1.433 Å (aug-cc-pVTZ). Minor increases in bond distance were observed along the C<sub>1</sub>C<sub>2</sub> and C<sub>3</sub>C<sub>4</sub> bonds upon excitation. A large decrease in the bond angle along the C<sub>6</sub>C<sub>1</sub>C<sub>2</sub> and C<sub>3</sub>C<sub>4</sub>C<sub>5</sub> bonds upon electronic excitation, from 117.1 to 112.1° was also present (aug-cc-pVTZ basis set). The calculated rotational constants in the  $\tilde{B}^2A_2$  state predicted by calculations were  $A' = 0.19602$  cm<sup>-1</sup>,  $B' = 0.087466$  cm<sup>-1</sup>, and  $C' = 0.060480$  cm<sup>-1</sup>. The calculated vibrational frequencies are listed in Table 3.2. The listed vibrational assignments are linear combinations of the ground state normal modes with coefficients corresponding to the dominant squared elements of the Duschinsky matrix ( $J_{ik}^2$ )[222] .

Table 3.2: Calculated normal mode frequencies ( $\text{cm}^{-1}$ ) for the phenoxy radical in the  $\tilde{\text{B}}^2\text{A}_2$  electronic state.

Mode Assignment	Sym.	cc-pVDZ	aug-cc-pVTZ
$0.63\nu_2 + 0.26\nu_1$	A <sub>1</sub>	3,123	3,114
$0.74\nu_1 + 0.25\nu_2$	A <sub>1</sub>	3,089	3,083
$0.87\nu_3 + 0.12\nu_2$	A <sub>1</sub>	3,067	3,062
$0.76\nu_5 + 0.19\nu_4$	A <sub>1</sub>	1,576	1,534
$0.69\nu_4 + 0.21\nu_6 + 0.09\nu_5$	A <sub>1</sub>	1,529	1,520
$0.73\nu_6 + 0.15\nu_5 + 0.11\nu_4$	A <sub>1</sub>	1,366	1,373
$0.92\nu_7$	A <sub>1</sub>	1,127	1,139
$0.91\nu_8$	A <sub>1</sub>	1,005	1,007
$0.99\nu_9$	A <sub>1</sub>	936	947
$0.99\nu_{10}$	A <sub>1</sub>	787	789
$1.00\nu_{11}$	A <sub>1</sub>	498	503
$0.96\nu_{12}$	A <sub>2</sub>	947	948
$0.97\nu_{13}$	A <sub>2</sub>	809	813
$0.99\nu_{14}$	A <sub>2</sub>	324	320
$0.87\nu_{15} + 0.12\nu_{16}$	B <sub>1</sub>	952	964
$0.63\nu_{16} + 0.27\nu_{17}$	B <sub>1</sub>	834	838
$0.48\nu_{17} + 0.29\nu_{18} + 0.12\nu_{16} + 0.10\nu_{19}$	B <sub>1</sub>	739	749
$0.63\nu_{18} + 0.12\nu_{16} + 0.10\nu_{17}$	B <sub>1</sub>	512	511
$0.84\nu_{19} + 0.13\nu_{17}$	B <sub>1</sub>	400	397
$0.94\nu_{20}$	B <sub>1</sub>	106	98
$1.00\nu_{21}$	B <sub>2</sub>	3,088	3,082
$1.00\nu_{22}$	B <sub>2</sub>	3,070	3,065
$0.47\nu_{24} + 0.31\nu_{23} + 0.17\nu_{25}$	B <sub>2</sub>	1,567	1,567
$0.60\nu_{23} + 0.36\nu_{24}$	B <sub>2</sub>	1,366	1,392
$0.74\nu_{25} + 0.13\nu_{24}$	B <sub>2</sub>	1,312	1,321
$0.98\nu_{26}$	B <sub>2</sub>	1,204	1,218
$0.89\nu_{27}$	B <sub>2</sub>	1,126	1,143
$0.94\nu_{28}$	B <sub>2</sub>	985	987
$0.99\nu_{29}$	B <sub>2</sub>	574	579
$0.99\nu_{30}$	B <sub>2</sub>	416	420

The vibronically resolved electronic spectrum for the  $\tilde{B}^2A_2 \leftarrow \tilde{X}^2B_1$  transition of the phenoxoy radical was predicted using the Franck-Condon approximation, implemented using Gaussian 09[222]. Only transitions arising from the zero-point level of the ground state are considered. Optimized geometries and scaled vibrational frequencies for both  $\tilde{B}^2A_2$  and  $\tilde{X}^2B_1$  states were used in this simulation, shown in Figure 3.5.

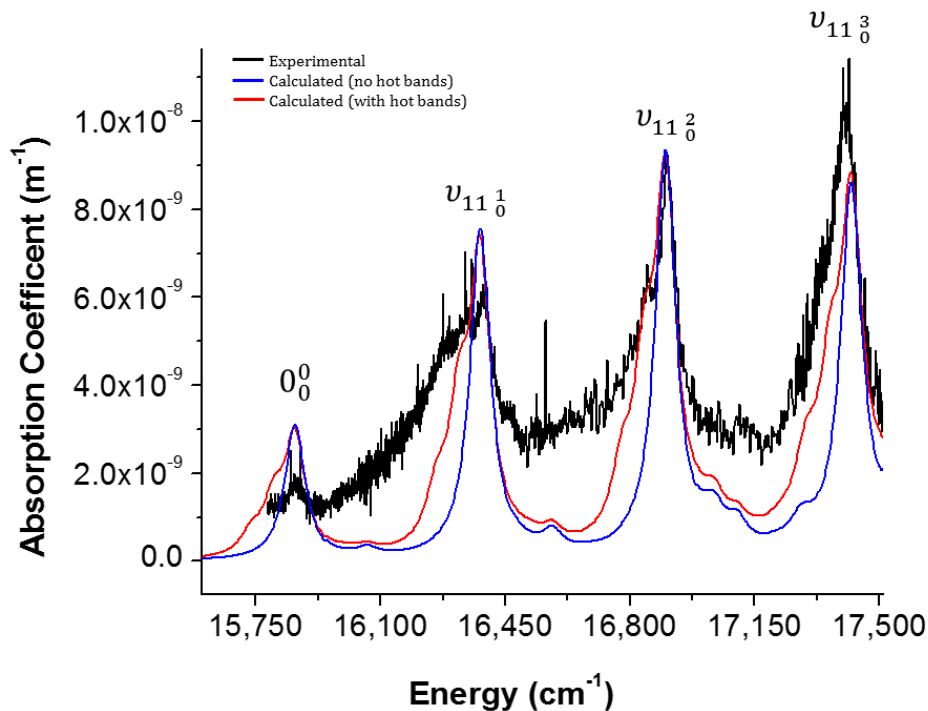


Figure 3.5: CRDS absorption spectrum of the jet-cooled anisole discharge products (black trace) overlaid with calculated spectra (aug-cc-pVTZ) of the  $\tilde{B}^2A_2 \leftarrow \tilde{X}^2B_1$  transition of the phenoxoy radical both with (red) and without (blue) hot bands.

### 3.1.5 Discussion

The ring geometry in the ground electronic has been previously described as an intermediate between aromatic and quinoid in character by Chipman *et al.*[190]. Our calculated bond lengths for the carbon ring in the ground state are consistent with their study. In the  $\tilde{B}^2A_2$  state the ring structure is more quinoid in character. As

noted previously, the largest geometry changes upon excitation are the lengthening of the C<sub>2</sub>C<sub>3</sub> (and C<sub>5</sub>C<sub>6</sub>) bond and a decrease in the C<sub>6</sub>C<sub>1</sub>C<sub>2</sub> and C<sub>3</sub>C<sub>4</sub>C<sub>5</sub> bond angles. The C<sub>2</sub>C<sub>3</sub> bond is lengthened by removal of an electron from the  $\pi_x$  orbital centralized on this bond to a delocalized  $\pi_x$  bond with bonding character over the C<sub>6</sub>C<sub>1</sub>C<sub>2</sub> and C<sub>3</sub>C<sub>4</sub>C<sub>5</sub> regions, while also decreasing the bond angles over these regions by roughly 5°.

These results cannot be accurately compared to the isoelectronic phenylthiyl radical as the only reported gas phase study on the  $\tilde{B}^2A_2 \leftarrow \tilde{X}^2B_1$  transition does not provide sufficient details of the bonding characteristics for the states involved[223]. Additionally, previous studies of the  $\tilde{A}^2B_2 \leftarrow \tilde{X}^2B_1$  transition of phenylthiyl[224, 225] indicate that the electron density is centered on the sulfur in both electronic states, while for the corresponding transition in the phenoxy radical the electron density is delocalized over the oxygen and the aromatic ring[189, 211].

The electronic origin of the  $\tilde{B}^2A_2 \leftarrow \tilde{X}^2B_1$  was predicted to occur at 16,620 cm<sup>-1</sup> from TD-DFT calculations (aug-cc-pVTZ basis set). Results from the aug-cc-pVDZ calculations are not shown as only minor differences are present between the simulations for the double- $\zeta$  and triple- $\zeta$  basis sets. The calculated spectra in Figure 3.5 have been shifted by 760 cm<sup>-1</sup> in order to make a more direct comparison with the experimental data. The level of agreement between the experimental and calculated spectra provides strong support for our assignment of these bands as arising from the  $\tilde{B}^2A_2 \leftarrow \tilde{X}^2B_1$  transition of the phenoxy radical. These findings are consistent with a previous theoretical study by Dierksen and Grimme[210], as well as the room temperature CRDS study by Araki *et al.*[212].

In order to further test the correlation between the experimental and simulated spectra, the molecular constants predicted using Gaussian were used to simulate the rotational contours of the observed vibronic bands by means of the PGOPHER program[226]. A Lorentzian line width component (FWHM  $\sim$  70 cm<sup>-1</sup>) was included

for each vibronic band to account for lifetime broadening of the excited state. These vibronic contours were markedly similar to the contour of a single broadened delta function when the Lorentzian contribution was greater than  $20 \text{ cm}^{-1}$ . As such the simulated spectra shown in Figure 3.5 contain no rotational information from the Gaussian calculations but are instead composed of broadened delta functions assigned to the observed vibronic progressions. It should be noted that any discrepancies in intensity between the experimental and simulated spectra are due to errors in the calculations, contributions from vibrationally hot bands, and variations in radical production efficiency in the experiment (most notable in the origin band).

The four vibronic bands observed in the experimental spectrum are assigned to the lowest energy  $A_1$  mode,  $\nu_{11}$ . The displacement vectors for this mode can be seen in Figure 3.6. This mode is a totally symmetric in-plane CC stretching/bending mode, with a large change in the  $C_6C_1C_2$  and  $C_3C_4C_5$  bond angles. This Franck-Condon favored normal mode is responsible for the  $516 \text{ cm}^{-1}$  vibronic band progression observed experimentally.

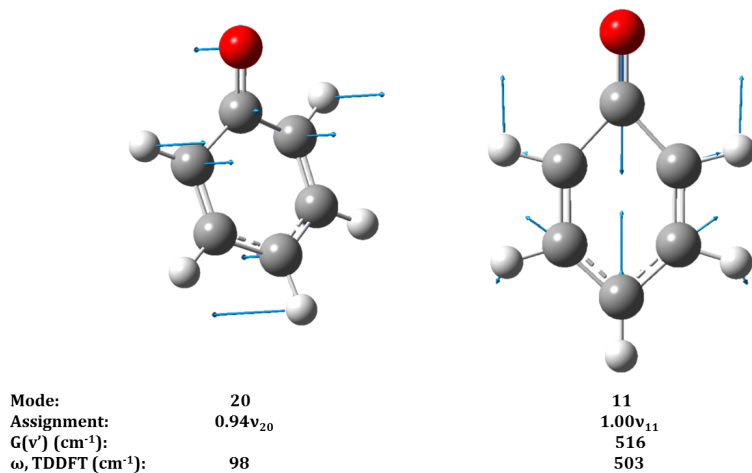


Figure 3.6: Excited state normal modes contributing to the optical activity in the  $\tilde{B}^2A_2 \leftarrow \tilde{X}^2B_1$  vibronic spectrum of the phenoxyl radical. The experimental term values are compared with the harmonic vibrational frequencies calculated at the TD-DFT/aug-cc-pVTZ level of theory.

The simulated vibronic bands (with  $70\text{ cm}^{-1}$  Lorentzian contribution) provide strong agreement with the most intense regions of each vibronic progression. However there are shoulders approximately  $60\text{ cm}^{-1}$  to the red of each peak that are not reproduced by these simulations. Initially it was assumed that these shoulders were vibrationally hot bands. The lowest ground state mode,  $\nu_{20}$  (out-of-plane CO wag), has a frequency of  $182\text{ cm}^{-1}$ . In the  $\tilde{\text{B}}\ ^2\text{A}_2$  state the  $\nu_{20}$  mode decreases to  $98\text{ cm}^{-1}$  (see Table 3.2). This could explain the origin of the shoulders in each feature if they were assigned to the symmetry allowed  $\nu_{20}$  hot bands. In order to test this theory, hot bands originating from  $\nu_{20_1^1}$  and  $\nu_{20_2^2}$  were included in the vibronic simulations by incorporating intensities from a Boltzmann distribution at 300K and a  $60\text{ cm}^{-1}$  red shift from each vibronic band. The resulting simulation can be seen as the red trace in Figure 3.5. This simulation had much stronger agreement with the experimental spectrum. It should be noted that since the origin and  $\nu_{11_0^1}$  bands were recorded using the continuous expansion source, the increased broadening observed (compared to the  $\nu_{11_0^2}$  and  $\nu_{11_0^3}$  bands collected using the pulsed valve configuration) is likely due to additional hot bands unaccounted for using this method. To verify this assumption the  $\nu_{11_0^3}$  band was recorded using the continuous expansion, which produced a much broader peak when compared to the pulsed valve configuration. Araki *et al.* studied the temperature dependence of the  $\tilde{\text{B}}\ ^2\text{A}_2 \leftarrow \tilde{\text{X}}\ ^2\text{B}_1$  transition of the phenoxy radical by analyzing the vibronic peak intensities at room temperature, cooled with dry ice, and at 400 K with a ribbon heater[212]. Their findings indicate that the shoulders on each peak arise from the  $\nu_{20_1^1}$  and  $\nu_{20_2^2}$  hot bands, confirming the results presented here.

The  $\tilde{\text{B}}\ ^2\text{A}_2 \leftarrow \tilde{\text{X}}\ ^2\text{B}_1$  transition of the phenoxy radical has been most recently assigned as  $\pi - \pi^*$  by Johnston[187] *et al.* and Radziszewski *et al.*[209]. However the results presented here favor a  $\pi - \pi^\circ$  assignment instead, where  $\pi^\circ$  is designated as a non-bonding orbital. The electronic structure calculations indicate only minor

changes in the Mulliken atomic spin densities between the  $\tilde{B}^2A_2$  and  $\tilde{X}^2B_1$  states. This is unsurprising as the electron promotion occurs within the carbon ring system, whereas for the  $\tilde{A}^2B_2$  state the electron density is localized over the oxygen atom[189]. The  $\tilde{A}^2B_2 \leftarrow \tilde{X}^2B_1$  transition of the phenoxy radical has been assigned as either  $\pi - \pi$  or  $\pi - \pi^\circ$  by Cheng *et al.*[189]. The results presented here support the  $\pi - \pi^\circ$  assignment as both the  $\tilde{A}^2B_2 \leftarrow \tilde{X}^2B_1$  and  $\tilde{B}^2A_2 \leftarrow \tilde{X}^2B_1$  transitions involve the promotion of an electron to the SOMO which Cheng *et al.*[189] describe as a, "non-bonding  $\pi^\circ$  orbital delocalized over the oxygen atom and the aromatic ring."

The substantial homogenous line broadening ( $70 \text{ cm}^{-1}$  FWHM) observed is attributed to lifetime broadening arising from nonradiative decay from the  $\tilde{B}^2A_2$  electronic state. The lifetime of the  $\tilde{B}^2A_2$  electronic state is 76 fs. The electronic structure calculations predict an oscillator strength of  $f=0.0054$ , which corresponds to a radiative lifetime of  $1.1 \mu\text{s}$ . The fluorescence quantum yield is  $7 \times 10^{-8}$ . Previous matrix studies by Johnston[187] *et al.* and Radziszewski *et al.*[209] reported similar broadening effects, but to a slightly larger degree. This is likely due to interactions with the matrix. This is supported by the room temperature CRDS study Araki *et al.*[212] who report a similar value for the Lorentzian line width as that presented here. Two possible pathways for nonradiative decay from the  $\tilde{B}^2A_2$  state have been presented in the literature. The first of these is rapid internal conversion to the  $\tilde{A}$  state[187]. However the  $\tilde{A}$  state was unassigned at the time of this study, and is now known to have  $^2B_2$  symmetry. This transition ( $\tilde{B}^2A_2 - \tilde{A}^2B_2$ ) is symmetry forbidden but could be allowed through vibronic coupling. The second is thermal decomposition of the phenoxy radical to produce the cyclopentadienyl radical plus carbon monoxide[64, 192]. This decomposition mechanism has been measured in two previous kinetic studies which report an activation energy of approximately  $15,400 \text{ cm}^{-1}$  (44 kcal/mol), which is roughly  $470 \text{ cm}^{-1}$  below the origin band reported here[179, 227]. An *ab initio* study of this decomposition mechanism by Liu and Lin predict an activation energy roughly

2,800  $\text{cm}^{-1}$  (52 kcal/mol) higher in energy than that reported experimentally[192]. However a later study by Carstensen and Dean[228] found that the kinetic data used by Liu and Lin do not represent high pressure values, and as such incorporating these values into an Arrhenius expression will underestimate the activation energy.

## 3.2 The Phenylperoxy Radical

This section is adapted from Freel *et al.*[229]. Access provided by American Chemical Society Publications.

### 3.2.1 Introduction

The phenylperoxy radical ( $\text{C}_6\text{H}_5\text{O}_2$ ) is known to be an important intermediate in combustion chemistry and the low temperature oxidation of benzene[10, 230, 231, 232, 233, 234]. It is produced by the barrierless exothermic reaction of the phenyl radical with  $\text{O}_2$ . Following its production, phenylperoxy may be stabilized by collisional relaxation or it may rearrange to form the 2-oxepinoxy radical[61, 178, 235]. If there is sufficient internal energy, the latter may further decompose to  $\text{CO}_2$  and the cyclopentadienyl radical via the sequence shown in Figure 3.7.

There are several other decomposition pathways at higher energies, including those that lead to the formation of the phenoxy radical ( $\text{C}_6\text{H}_5\text{O}$ ) [61, 62, 63, 178, 235]. Experimental studies of the  $\text{C}_6\text{H}_5 + \text{O}_2$  reaction have been conducted using normal gas phase conditions [80, 81, 230] and crossed molecular beams techniques [62, 63, 232]. This work has been accompanied by a substantial computational modeling effort [61, 178, 233, 234, 235, 236].

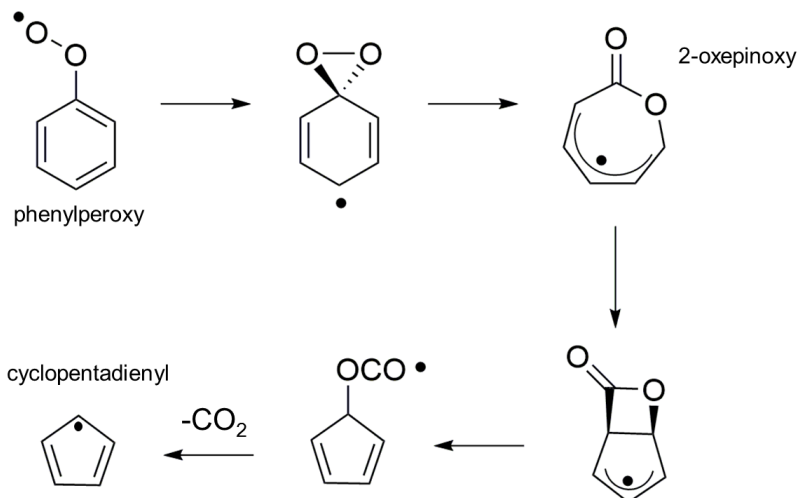


Figure 3.7: Formation of the cyclopentadienyl radical through the decomposition of the phenylperoxy radical.

In several experimental studies of the reaction kinetics, the absorption spectrum in the visible range has been used to monitor the concentration of the radical [80, 81, 230]. Some of the earliest spectroscopic data for phenylperoxy were obtained in the solution phase, using pulsed radiolysis to generate the radical [67, 237]. A broad absorption band, with a maximum near 470 nm, was reported. Yu and Lin [81] then observed an absorption feature in a gas phase experiment that was attributed to phenylperoxy. Their original intent was to study the phenyl + O<sub>2</sub> reaction by means of a phenyl absorption band at 504.8 nm. Owing to the weakness of this transition, they used the pulsed cavity ring-down spectroscopy (CRDS) technique for these measurements. A revised monitoring strategy was adopted when it was recognized that one of the reaction products also absorbed the 504.8 nm light. A spectrum for this product, which was essentially featureless over the 495-531 nm range, was attributed to phenylperoxy. This absorption was used by Lin and Yu [81], and subsequently by other groups studying the kinetics of phenylperoxy [80, 230], to monitor the production and decay of the radical. There is good circumstantial evidence linking the broad absorption near 504 nm to phenylperoxy, but the lack of structure is problematic. First, it is difficult to know if phenylperoxy is the only

absorbing species, or if there are other reaction products that contribute. Second, the lack of structure precludes a rigorous species assignment.

There have been theoretical studies of the three lowest energy electronic transitions of phenylperoxy[236, 237, 238]. Electronic structure calculations predict that the molecule is planar in the ground and the lower energy excited states, with  $C_s$  symmetry. The lowest energy transition,  $\tilde{A} \ ^2A' \leftarrow \tilde{X} \ ^2A''$  is attributed to promotion of an electron between orbitals that are mostly localized on the peroxy moiety[236, 238] (the singly occupied molecular orbital (SOMO) of the ground state receives the excited electron). This transition, which typically has a very small oscillator strength, is found at an energy near  $7,500 \text{ cm}^{-1}$  for a range of aromatic and aliphatic peroxy radicals[236, 239]. The next higher excited state for phenylperoxy involves promotion of an electron from an orbital that is approximately  $p\pi$  of the phenyl ring to the SOMO. As there are two ring  $p\pi$  orbitals that are close in energy (related to the  $e_{1g}$  orbitals of benzene), the second and third excited states (both  $A''$  symmetry) are attributed to promotions from these two orbitals (see Figure 5 of Weisman and Head-Gordon[236]). These transitions have larger oscillator strengths (on the order of  $10^{-3}$  to  $10^{-2}$ ) and are thought to be responsible for the visible and near UV absorption.

There are few spectroscopic studies reported for phenylperoxy. Yamauchi *et al.*[240] tentatively assigned the EPR spectrum and obtained a  $g$ -value typical of peroxy radicals ( $g \sim 2.014$ ). IR absorption spectra have been reported for the radical isolated in solid argon at 10 K[241]. In that study, seventeen fundamental bands were identified for the normal isotope, and three other isotopic variants were characterized. Density functional theory (DFT) calculations, at the level of UB3LYP with the Dunning cc-pVTZ basis set[218], yielded vibrational frequencies that were in reasonably good agreement with the measurements. The  $\tilde{A} \ ^2A' \leftarrow \tilde{X} \ ^2A''$  transition of phenylperoxy in the gas phase was examined by Just *et al.*[238] using CRDS. Their vibrationally resolved spectrum showed the origin ( $7,497 \text{ cm}^{-1}$ ), sequence bands involving a low

frequency mode ( $\sim 85 \text{ cm}^{-1}$ ), the O-O stretch modes, and C-O-O bending. The intensity pattern was consistent with the model of a peroxy-centered excitation to the  $\pi^*$ -like SOMO. Electronic structure calculations were performed to facilitate the analysis of the spectrum. Equilibrium geometries and vibrational frequencies were calculated for both the  $\tilde{A}$  and  $\tilde{X}$  states using the combination B3LYP/6-31+g(d). The scaled vibrational frequencies for the excited state were in good agreement with the observations.

Gas phase CRDS data for the higher energy transition(s) have been recorded at room temperature, with a focus on the 18,850 - 20,200  $\text{cm}^{-1}$  range[80, 81, 230]. These studies all report a structureless spectrum, and it is of obvious interest to determine the cause. Is the lack of structure due to homogeneous line broadening associated with rapid internal conversion and/or isomerization, spectral congestion, or some combination of these causes? Are there lower energy regions of the spectrum where structure can be observed? If so, the analysis of this structure might be used to further explore the validity of the assignment to the phenylperoxy radical. The discovery of structured regions of the spectrum may also facilitate a more species specific detection of the radical in future kinetic studies.

The congestion of the phenylperoxy spectrum may be significantly reduced by the application of jet-expansion cooling techniques. Miller and co-workers have shown that cold peroxy radicals can be produced using  $\text{O}_2$  addition reactions in an electric discharge slit expansion[242, 243, 244]. In the recent past we have used the discharge slit expansion technique to record rotationally resolved spectra for the  $1^2\text{B}_1 \leftarrow \tilde{X}^2\text{A}_1$  transition of the phenyl radical[74]. In the present study we used the same system to examine phenylperoxy. A vibrationally resolved spectrum was observed in the 17,500-19,900  $\text{cm}^{-1}$  range. The spectrum was assigned using the predictions from time dependent density functional theory (TD-DFT) calculations.

### 3.2.2 Methods

The discharge-jet, cavity ring down spectrometer used for these measurements was described in detail by Freel *et al.*[74]. The most significant difference for the present experiments was the use of a continuous slit expansion. The pulsed valves of the earlier design were not used due to problems with the repeatability of the gas pulses, which resulted in nonuniform discharges, intermittent arching, and problems with the deposition of soot on the discharge electrodes. Consequently, a continuous gas flow was used, with pulsed discharge production of the radicals.

High voltage jaws and grounding plates defined the slit discharge assembly (see Figure 2 of Freel *et al.*[74]). Phenolic spacers (1 mm thick) provided insulation between the electrically grounded aluminum mounting plate and the high voltage jaws. The discharge plates (80 mm in length) formed a slit with a width of 1 mm. The electrical discharge was operated at a voltage of -800 V with a pulse duration of 2 ms. These conditions produced a current of approximately 65 mA through a 1 k $\Omega$  ballast resistor during the discharge.

The phenylperoxy radical was produced by secondary reactions in the discharge and postdischarge flow. The gas mixture prior to the discharge consisted of bromobenzene vapor in a mixture of Ar and O<sub>2</sub>. It is well-known that discharge excitation of bromobenzene/Ar mixtures will produce the phenyl radical. Presumably, the phenylperoxy radical was produced in the postdischarge region of the jet by the O<sub>2</sub> addition reaction ( $\text{C}_6\text{H}_5 + \text{O}_2 + \text{Ar} \rightarrow \text{C}_6\text{H}_5\text{O}_2 + \text{Ar}$ ). Bromobenzene vapor was entrained by bubbling the Ar/O<sub>2</sub> carrier gas mixture through a liquid sample. The sample and gas lines were heated to 70 C° to increase the partial pressure of bromobenzene. For a carrier gas source pressure of 1 atm (the typical operating condition for these experiments) we estimate that the mole fraction of bromobenzene was in the range 0.01-0.04. To help identify the reaction products resulting from the oxygen chemistry, spectra were recorded for mixtures with and without oxygen,

but with all other conditions held as near to constant as could be achieved. The mole fraction of the oxygen in the gas mixture was varied to find the optimum conditions for phenylperoxy formation. Initial experiments were performed with premixed Ar/O<sub>2</sub>. However, it was found to be easier to tune the conditions continuously by inline mixing. A needle valve was used to control the addition of O<sub>2</sub> to Ar, prior to the mixture passing through the bromobenzene. The liquid sample was replaced at regular intervals to avoid the accumulation of oxidation products.

Two sets of cavity mirrors were used for these measurements. The dielectric coatings on these mirrors provided their highest reflectivities (99.995 %) at 500 and 540 nm. As the mirrors were separated by 1 m, the maximum theoretical ringdown time was 66  $\mu$ s. Typically, empty cavity ring-down times of around 40  $\mu$ s were observed. The ring-down spectra of the discharge products exhibited lines from metastable excited states of Ar and the Swan bands of C<sub>2</sub>. These features were used to establish the absolute wavenumber calibrations. For the phenylperoxy spectrum, the best compromise between signal strength and cooling was obtained with the laser beam position 7 mm away from the discharge slit.

Survey scans covering about 10 nm per sweep were acquired using a laser step size of  $\sim 0.4$  cm<sup>-1</sup> while averaging 30 ringdown decay curves per point (15 with the discharge on and 15 with the discharge off). Pairs of scans were coadded to improve the sensitivity and ensure reproducibility. Shorter ranges of interest, such as the origin band region, were acquired using a smaller laser step size of  $\sim 0.04$  cm<sup>-1</sup> while averaging 30 ringdown time measurements per point. Five scans were coadded to reduce the noise.

### 3.2.3 Experimental Results

The experimental conditions were first optimized by observing the spectrum of the phenyl radical by discharging Ar/C<sub>6</sub>H<sub>5</sub>Br mixtures. Broad-band absorption and/or

scattering losses were present across the entire range of the spectrum. The ring-down time also changed with wavelength due to changes in mirror reflectivity. The absorption coefficient,  $\alpha$  ( $\text{m}^{-1}$ ), was calculated at each wavelength measurement from Equation 3.4 where  $L$  is the cavity length (1 m),  $l$  is the single pass sample path length (0.08 m),  $\tau_1$  is the directly measured ring-down time with the laser passing through the discharge products, and  $\tau_2$  is the background ring-down time that included broadband absorption and scattering losses, but without the discharge. Figure 3.8a shows a typical spectrum for the Ar/C<sub>6</sub>H<sub>5</sub>Br mixture.

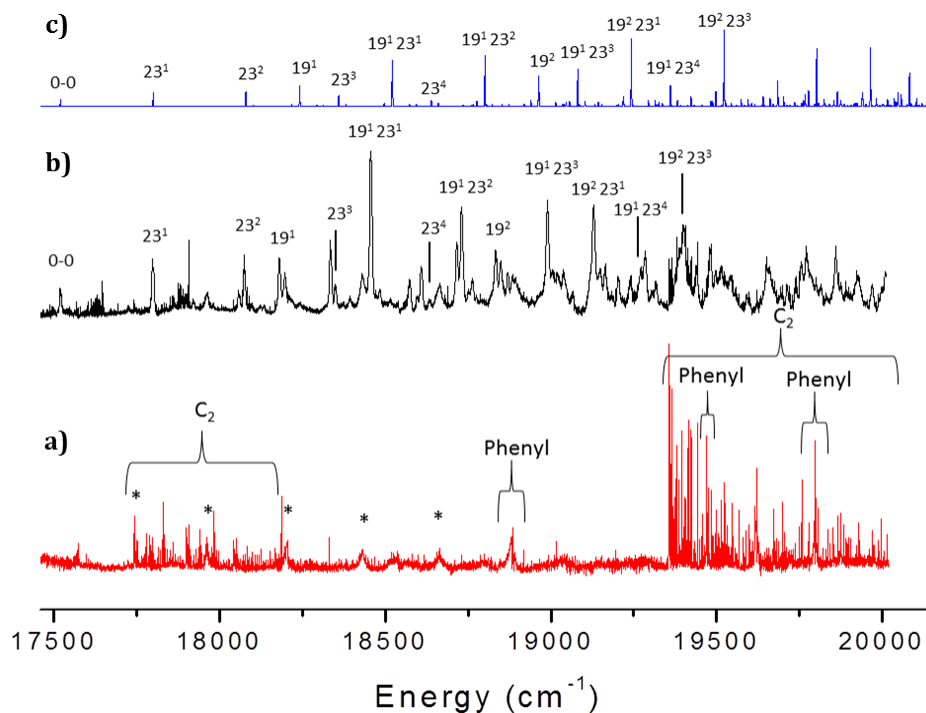


Figure 3.8: CRDS absorption spectra of the products in an expansion of electrically dissociated bromobenzene (a) without O<sub>2</sub> and (b) with O<sub>2</sub> compared to (c) a spectrum for phenylperoxy predicted using molecular properties from a TD-DFT/aug-cc-pVTZ calculation.

The bands of phenyl and C<sub>2</sub> were the dominant features. There was also a progression of bands with a spacing of about 235 cm<sup>-1</sup> (marked with asterisks in Figure 3.8), for which the carrier has not yet been identified. In addition to the structured features, there was a continuous background that increased approximately linearly from

$8.1 \times 10^{-9} \text{ m}^{-1}$  at  $17,650 \text{ cm}^{-1}$  to  $3.6 \times 10^{-8} \text{ m}^{-1}$  at  $20,000 \text{ cm}^{-1}$ . This background has been subtracted from the traces of Figure 3.8a,b.

After observing the Ar/C<sub>6</sub>H<sub>5</sub>Br discharge products, O<sub>2</sub> was added to the carrier flow and the concentration was increased until the phenyl radical absorption was below the noise level. Premixed gases with 1 % and 10 % O<sub>2</sub> in Ar were used to test the concentration necessary to observe new features. It was found that >10 % O<sub>2</sub> was needed to deplete the phenyl absorption and produce the new spectral features. At 10 % O<sub>2</sub>, the phenyl absorption was reduced by 50 %, but new features were not observed. However, further addition of O<sub>2</sub>, accomplished using inline mixing, resulted in the complete consumption of phenyl and the appearance of many new spectral features. As can be seen in Figure 3.8b, the reaction with oxygen removed the C<sub>2</sub> and phenyl absorption bands, but the unidentified features with a spacing of  $235 \text{ cm}^{-1}$  remained. We have assigned the dominant bands in Figure 3.8b to a single carrier, on the basis of their common response to changes in the oxygen content and expansion conditions. Scanning to energies below  $17,500 \text{ cm}^{-1}$  revealed known bands of the phenoxy radical[81], but no other features of the dominant new spectrum. Hence, we assign the feature at  $17,519 \text{ cm}^{-1}$  as an origin band. The band centers for the more intense new features of Figure 3.8b are listed in Table 3.3. After correction for the baseline signal, the most intense band of the new spectrum ( $18,463 \text{ cm}^{-1}$ ) had an absorption coefficient of  $\alpha = 4.2 \times 10^{-8} \text{ m}^{-1}$ . Regular vibrational progressions were easily recognized in the lower energy range. The harmonic vibrational constants defined by these progressions are given in Table B.1 of the Appendix.

The sharper molecular features of Figure 3.8b exhibited widths of approximately  $5\text{-}10 \text{ cm}^{-1}$  (FWHM) in the low resolution survey scan. To learn more about the rotational structure, or the homogeneous line broadening, the  $17,519 \text{ cm}^{-1}$  band was recorded using a step size of  $0.04 \text{ cm}^{-1}$ . The result from this scan, shown in Figure 3.9, was an unresolved contour. However, this feature was not entirely without structure,

and the characteristic P- and R- branch maxima of a parallel transition could be discerned.

Table 3.3: List of measured band positions and vibrational energies ( $G(\nu)$ ) compared with scaled harmonic vibrational frequencies ( $\Delta E$ ) from theoretical calculations (in  $\text{cm}^{-1}$ )

Band	Band Center	$G(\nu)$	$\Delta E$	$\Delta E$ Scaled
$0^0$	17,159	0	0	0
$23^1$	17,798	279	289.3	279.8
$22^1$	17,920	401	432.2	417.9
$20^1$	18,057	538	601.3	581.5
$23^2$	18,074	555	578.6	559.5
$19^1$	18,180	661	746.2	721.6
$22^1 23^1$	18,196	678	721.5	697.7
$20^1 23^1$	18,335	816	890.5	861.1
$23^3$	18,349	830	867.8	839.2
$19^1 23^1$	18,456	937	1,035.4	1,001.3
$22^1 23^2$	18,483	964	1,010.8	977.4
$19^1 22^1$	18,573	1,054	1,178.4	1,139.5
$20^2$	18,596	1,078	1,202.5	1,162.8
$20^1 23^2$	18,608	1,090	1,179.8	1,140.9
$23^4$	18,633	1,115	1,157.1	1,118.9
$19^1 20^1$	18,715	1,196	1,347.4	1,303.0
$19^1 23^2$	18,730	1,211	1,324.7	1,281.0
$22^1 23^3$	18,752	1,234	1,300.0	1,257.1
$12^1$	18,762	1,243	1,288.7	1,246.2
$19^2$	18,833	1,314	1,492.3	1,443.1
$19^1 22^1 23^1$	18,848	1,329	1,467.6	1,419.2
$20^2 23^1$	18,869	1,351	1,491.8	1,442.6
$20^1 23^3$	18,883	1,365	1,469.1	1,420.6
$19^1 23^3$	18,989	1,471	1,614.0	1,560.7
$19^1 20^1 23^1$	19,004	1,486	1,636.7	1,582.7
$20^1 22^1 23^2$	19,019	1,501	1,612.0	1,558.8
$12^1 23^1$	19,038	1,520	1,578.0	1,525.9
$19^2 23^1$	19,128	1,610	1,781.6	1,722.8
$19^1 22^1 23^2$	19,148	1,629	1,756.9	1,698.9
$12^1 22^1$	19,163	1,645	1,720.9	1,664.1
$19^1 20^2$	19,203	1,684	1,948.7	1,884.4
$12^1 20^1$	19,240	1,721	1,889.9	1,827.6
$19^1 23^4$	19,271	1,752	1,903.3	1,840.5
$19^1 20^1 23^2$	19,284	1,765	1,926.0	1,862.4
$12^1 23^2$	19,316	1,797	1,867.3	1,805.6

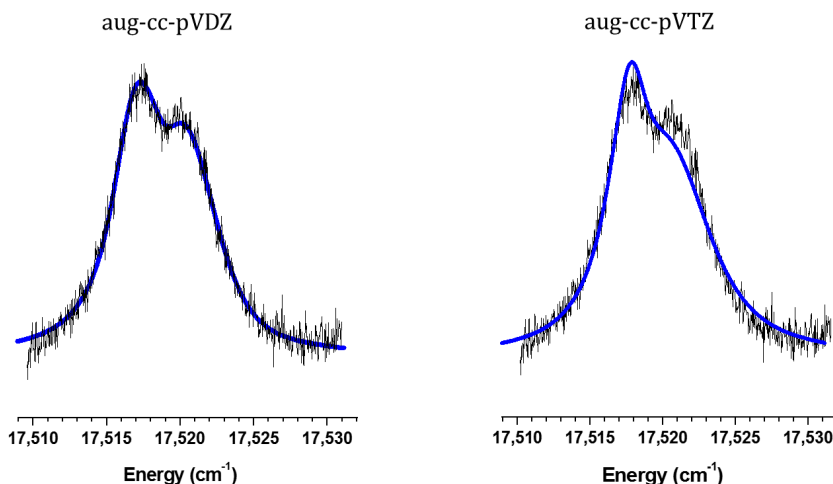


Figure 3.9: Rotational contour of the phenylperoxy  $\tilde{B}^2A'' \leftarrow \tilde{X}^2A''$  origin band. This figure shows two copies of the experimental data (traces with noise) accompanied by computer simulations. The left-hand side shows the best fit simulation based on the molecular constants from the TD-DFT/aug-cc-pVDZ calculations. These were  $A'' = 0.172045$ ,  $B'' = 0.053640$ ,  $C'' = 0.040903$ ,  $A' = 0.162784$ ,  $B' = 0.055228$ ,  $C' = 0.0412371 \text{ cm}^{-1}$ ,  $\mu_a = 0.827$ , and  $\mu_b = 0.371 \text{ D}$ . The simulation on the right used the constants from the TD-DFT/aug-cc-pVTZ calculations. These were  $A'' = 0.17415$ ,  $B'' = 0.05045$ ,  $C'' = 0.04125$ ,  $A' = 0.16449$ ,  $B' = 0.05564$ ,  $C' = 0.04115 \text{ cm}^{-1}$ ,  $\mu_a = 0.838$ , and  $\mu_b = 0.385 \text{ D}$ .

### 3.2.4 Theoretical Calculations

Theoretical predictions of the visible band systems of phenylperoxy were carried out to assist with the spectral assignment. All calculations were performed using the Gaussian 09 suite of computational chemistry programs[217]. The ground state equilibrium structure and harmonic vibrational frequencies were calculated using the UB3LYP hybrid DFT method with Dunning’s aug-cc-pVDZ and aug-cc-pVTZ basis sets[218]. Tight convergence criteria were used for the geometry optimizations. In agreement with earlier studies[236, 238], the peroxy  $p\pi$  orbital was found to be prominent in the SOMO of the  $\tilde{X}^2A''$  ground state. This orbital is shown in Figure 3.10. Bond lengths and bond angles are listed in Tables B.2 and B.3 of the Appendix, and Figure 3.11a shows the equilibrium structure from the B3LYP/aug-cc-pVTZ calculation. The O=O bond length of  $1.321 \text{ \AA}$  is close to known lengths for other peroxy radicals.

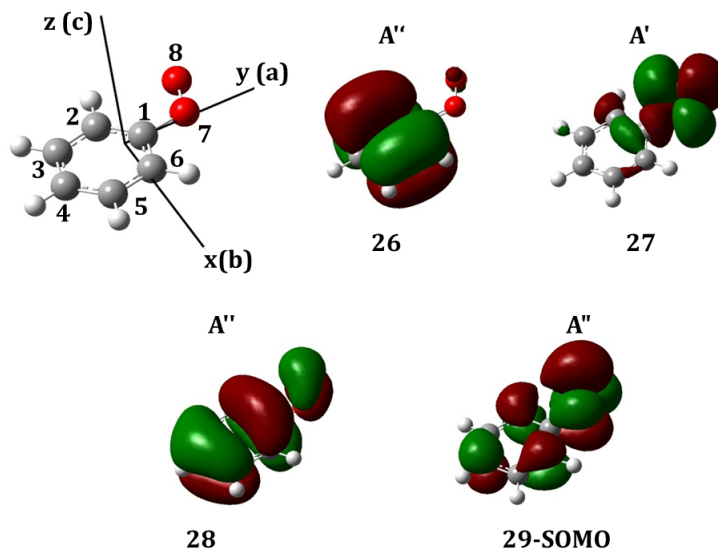


Figure 3.10: Molecular orbitals involved in the first three electronic transitions of phenylperoxy calculated at the B3LYP/aug-cc-pVTZ level for  $\tilde{X}^2A''$ . Plots were generated with an isodensity value of 0.02 au.

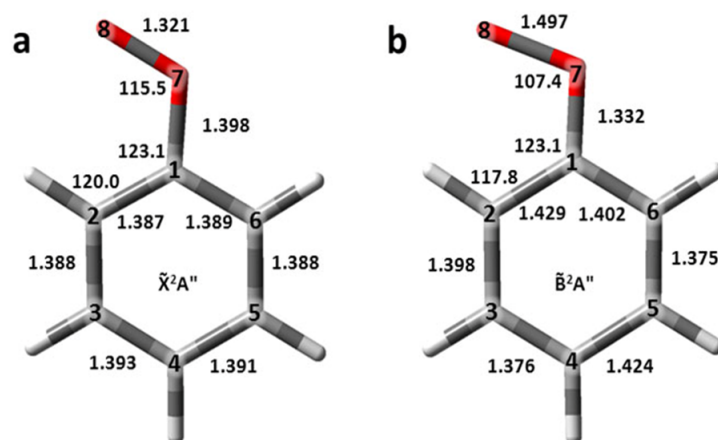


Figure 3.11: Equilibrium bond lengths and bond angles for the phenylperoxy radical calculated at the B3LYP/aug-cc-pVTZ level for (a)  $\tilde{X}^2A''$  and (b) by TD-DFT/aug-cc-pVTZ for  $\tilde{B}^2A''$ .

Table 3.4: Calculated and scaled normal mode frequencies ( $\text{cm}^{-1}$ ) for the phenylperoxy radical in the  $\tilde{X}^2A''$  and  $\tilde{B}^2A''$  electronic states compared with experimental vibrational intervals<sup>a</sup>

$\tilde{X}^2A''$				$\tilde{B}^2A''$			
Mode	Sym.	$\omega$	Exp.	Mode Assignment	Sym.	$\omega$	Exp.
$\nu_1$	$a'$	3,120	3,119	$0.99\nu_1\dots$	$a'$	3,157	
$\nu_2$	$a'$	3,096	3,189	$0.96\nu_2\dots$	$a'$	3,101	
$\nu_3$	$a'$	3,088	3,089	$0.97\nu_3\dots$	$a'$	3,095	
$\nu_4$	$a'$	3,078	3,071	$0.85\nu_4 + 0.14\nu_5\dots$	$a'$	3,080	
$\nu_5$	$a'$	3,069		$0.84\nu_5 + 0.13\nu_4\dots$	$a'$	3,072	
$\nu_6$	$a'$	1,586		$0.67\nu_7\dots$	$a'$	1,623	
$\nu_7$	$a'$	1,566		$0.53\nu_9 + 0.31\nu_6\dots$	$a'$	1,480	
$\nu_8$	$a'$	1,461	1,481	$0.66\nu_8 + 0.25\nu_6\dots$	$a'$	1,448	
$\nu_9$	$a'$	1,447	1,464	$0.17\nu_{11} + 0.35\nu_9 + 0.19\nu_6\dots$	$a'$	1,396	
$\nu_{10}$	$a'$	1,303	1,313	$0.68\nu_{10}\dots$	$a'$	1,333	
$\nu_{11}$	$a'$	1,300		$0.66\nu_{11}\dots$	$a'$	1,274	
$\nu_{12}$	$a'$	1,161		$0.47\nu_{15} + 0.22\nu_{10}\dots$	$a'$	1,246	1,243
$\nu_{13}$	$a'$	1,143		$0.79\nu_{13}\dots$	$a'$	1,150	
$\nu_{14}$	$a'$	1,131		$0.14\nu_{16} + 0.18\nu_{15} + 0.49\nu_{12}\dots$	$a'$	1,104	
$\nu_{15}$	$a'$	1,088		$0.75\nu_{16} + 0.15\nu_{12}\dots$	$a'$	1,038	
$\nu_{16}$	$a'$	1,066	1,123	$0.28\nu_{16} + 0.59\nu_{17}\dots$	$a'$	976	
$\nu_{17}$	$a'$	986	1,019	$0.68\nu_{18} + 0.28\nu_{17}\dots$	$a'$	962	
$\nu_{18}$	$a'$	820		$0.76\nu_{19} + 0.14\nu_{14}\dots$	$a'$	794	
$\nu_{19}$	$a'$	750	793	$0.12\nu_{20} + 0.17\nu_{19} + 0.58\nu_{14}\dots$	$a'$	721	661
$\nu_{20}$	$a'$	606	615	$0.80\nu_{21} + 0.17\nu_{20}\dots$	$a'$	581	538
$\nu_{21}$	$a'$	600	607	$0.17\nu_{21} + 0.66\nu_{20}\dots$	$a'$	493	
$\nu_{22}$	$a'$	432		$0.93\nu_{22}\dots$	$a'$	418	401
$\nu_{23}$	$a'$	257		$0.95\nu_{23}\dots$	$a'$	280	279
$\nu_{24}$	$a''$	1,005		$0.94\nu_{24}\dots$	$a''$	963	
$\nu_{25}$	$a''$	981		$0.92\nu_{25}\dots$	$a''$	959	
$\nu_{26}$	$a''$	962	905	$0.93\nu_{26}\dots$	$a''$	871	
$\nu_{27}$	$a''$	906		$0.92\nu_{27}\dots$	$a''$	806	
$\nu_{28}$	$a''$	780	752	$0.98\nu_{28}\dots$	$a''$	736	
$\nu_{29}$	$a''$	673	679	$0.87\nu_{29}\dots$	$a''$	672	
$\nu_{30}$	$a''$	479	481	$0.88\nu_{30}\dots$	$a''$	461	
$\nu_{31}$	$a''$	407		$0.94\nu_{31}\dots$	$a''$	390	
$\nu_{32}$	$a''$	228		$0.20\nu_{33} + 0.78\nu_{32}\dots$	$a''$	173	
$\nu_{32}$	$a''$	88		$0.77\nu_{33} + 0.20\nu_{32}\dots$	$a''$	111	

<sup>a</sup>The ground state experimental values were reported by Mardyukov and Sander[241]. The calculations are for the aug-cc-pVDZ/aug-cc-pVTZ basis set.

The CO bond was 1.398 Å, which is comparable to the single bond C-O in methanol (1.427 Å). All of the CC bonds were close to 1.40 Å, representative of a benzene ring. The rotational constants were predicted to be  $A'' = 0.17415$ ,  $B'' = 0.05045$ , and  $C'' = 0.04125$  cm<sup>-1</sup>. Ground state vibrational frequencies, scaled by the recommended value[221] of 0.967, are listed in Table 3.4. These were in good agreement with the results from the matrix isolation study of the IR spectrum[241].

Excited state properties were predicted using time-dependent density functional theory (TD-DFT) with the basis sets noted above. The calculations considered eight excited states and were separately optimized for the first, second, and third excited states. Equilibrium structures and vibrational frequencies were obtained. The bond lengths and bond angles for the  $\tilde{A} \ ^2A'$ ,  $\tilde{B} \ ^2A''$ , and  $\tilde{C} \ ^2A''$  states are given in Tables B.2 and B.3 of the Appendix. Figure 3.11b shows the equilibrium structure for the second excited state ( $\tilde{B} \ ^2A''$ ). At the ground state equilibrium geometry, the calculations yielded vertical transition energies of 9,345 cm<sup>-1</sup> ( $\tilde{A} \ ^2A' \leftarrow \tilde{X} \ ^2A''$ ), 22,696 cm<sup>-1</sup> ( $\tilde{B} \ ^2A'' \leftarrow \tilde{X} \ ^2A''$ ), and 24,917 cm<sup>-1</sup> ( $\tilde{C} \ ^2A'' \leftarrow \tilde{X} \ ^2A''$ ). The oscillator strengths were  $<10^{-4}$ , 0.059, and 0.022, respectively. These transitions involve the promotion of an electron from molecular orbitals 26, 27, or 28 (cf., Figure 3.10) to the SOMO. Orbital 27 has been described as being antibonding along the R-O bond, and nonbonding between the oxygen atoms. Orbitals 26 and 28 resemble the two  $e_{1g}$  degenerate HOMO's of benzene.

Scaled vibrational frequencies for the  $\tilde{B} \ ^2A''$  state are listed in Table 3.4, and the frequencies for the  $\tilde{A} \ ^2A'$  and  $\tilde{C} \ ^2A''$  states are given in Tables B.4 and B.5 of the Appendix. Note that the mode labels for the excited states are given as linear combinations of the ground state normal modes with coefficients corresponding to the leading squared elements of the Duschinsky matrix[222] ( $J_{ik}^2$ ).

The vibrationally resolved electronic spectra for the first three electronic transitions of phenylperoxy were predicted using the Franck-Condon approximation, as implemented in Gaussian 09. This model considers transition arising from only the zero-point level of the ground state. The scaled vibrational frequencies were used. The calculated oscillator strengths and adiabatic transition energies ( $T_e$  and  $T_0$ ) are given in Table 3.5.

Table 3.5: Oscillator strength ( $f$ ), vertical excitation energy, adiabatic excitation energy ( $T_e$ ), and electronic transition origin ( $T_{0,0}$ ) for the first three electronic transitions of phenylperoxy calculated using TD-DFT with the aug-cc-pVDZ and aug-cc-pVTZ basis sets

Transition	$\tilde{A}^2A' \leftarrow \tilde{X}^2A''$	$\tilde{B}^2A'' \leftarrow \tilde{X}^2A''$	$\tilde{C}^2A'' \leftarrow \tilde{X}^2A''$
Oscillator Strength ( $f$ ) <sup>a</sup>	0.0/0.0	0.0561/0.0587	0.0228/0.0220
vertical excitation energy (cm <sup>-1</sup> ) <sup>a</sup>	9,314/9,345	22,486/22,696	24,614/24,917
TD-DFT $T_e$ (cm <sup>-1</sup> ) <sup>a</sup>	8,900/8,938	17,572/17,580	20,516/20,686
TD-DFT $T_{0,0}$ (cm <sup>-1</sup> ) <sup>a</sup>	8,743/8,787	17,204/17,222	21,056/21,189
exp $T_{0,0}$ (cm <sup>-1</sup> ) <sup>b</sup>	7,497	17,518	

<sup>a</sup>Calculated value listed using basis sets aug-cc-pVDZ/aug-cc-pVTZ.

<sup>b</sup>Experimental values are listed for comparison ( $T_{0,0}$  for  $\tilde{A}^2A' \leftarrow \tilde{X}^2A''$  taken from Just *et al.*[238]).

### 3.2.5 Discussion

The calculated spectrum for the  $\tilde{A}^2A' \leftarrow \tilde{X}^2A''$  transition is compared with the experimental data of Just *et al.*[238] in Figure 3.12. For this exercise the origin band was shifted down by 1,290 cm<sup>-1</sup> to match the experiment. With this correction, the vibronic intensity pattern is in moderately good agreement with the data for transitions from the zero-point level.

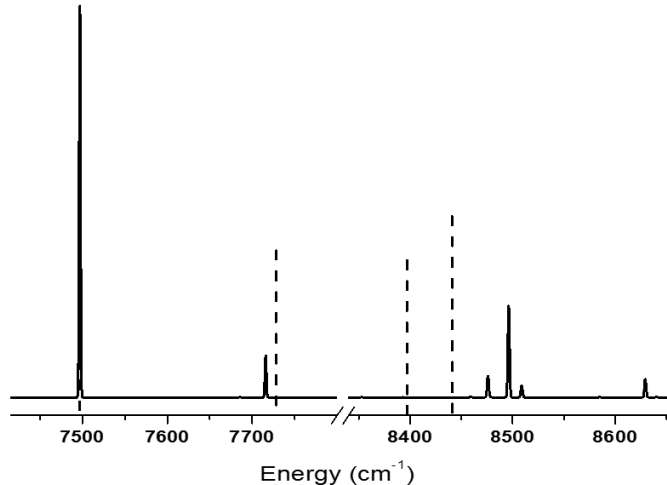


Figure 3.12: Calculated (TD-DFT/aug-cc-pVTZ) vibrationally resolved electronic spectrum for the  $\tilde{A}^2A' \leftarrow \tilde{X}^2A''$  transition of phenylperoxy (solid trace) compared to the experimental (dashed) line positions and estimated relative intensities from Just *et al.*[238]. The break is where experimental data were not available.

As expected[236, 238], significant geometry changes for the  $\tilde{A}^2A' \leftarrow \tilde{X}^2A''$  transition were localized at the peroxy group. There was an increase in the O-O bond length and slight decreases in the C-O bond length and O-O-C bond angle. These same geometric changes were also predicted for the  $\tilde{B}^2A'' \leftarrow \tilde{X}^2A''$  transition, but to a larger extent (cf., Figure 3.11). In addition, there were significant changes in the carbon ring. The ring geometry in the excited state resembled a quinone whereas the ground electronic state resembled benzene. The largest changes in bond angles for this transition were the  $8^\circ$  decrease of the  $O_8 - O_7 - C_1$  bond angle, the  $2^\circ$  decrease of the  $C_2 - C_1 - C_6$  angle, and the  $2^\circ$  decrease of the  $C_1 - C_2 - H_2$  angle. In the ground state the atoms  $O_8 - O_7 - C_1 - C_2 - H_2$  were arranged with angles resembling a six-member ring. The geometry of these atoms in the  $\tilde{B}^2A''$  state resembled a five-member ring. This is explained by the interaction between  $O_8$  and  $C_2$  indicated by the SOMO, which becomes stronger when the orbital is doubly occupied in the excited state.

The calculated vibronic structure for the  $\tilde{B}^2A'' \leftarrow \tilde{X}^2A''$  transition is shown in Figure 3.8c. For comparison with the experimental data, the origin of the calculated spectrum has been shifted up by  $296 \text{ cm}^{-1}$ . The level of agreement between the new spectrum and the simulation strongly supports the assignment to phenylperoxy. Excited state vibrational intervals from the spectrum are compared with calculated frequencies in Table 3.4. As Gaussian 09 uses harmonic frequencies, it is no surprise to find that the level of agreement decreases with increasing vibrational excitation. All of the optically active vibrational modes are of  $a'$  symmetry. The two most intense progressions are associated with vibrational modes 23 and 19. These can be approximately described as the C-O-O bend and the O-O stretch. Progressions with weaker intensities were associated with modes 22, 20, and 12. The displacement vectors for these Franck-Condon favored modes are shown in Figure 3.13. All have significant displacements relating to O-O stretching or in-plane bending within the  $O_8 - O_7 - C_1 - C_2 - H_2$  group.

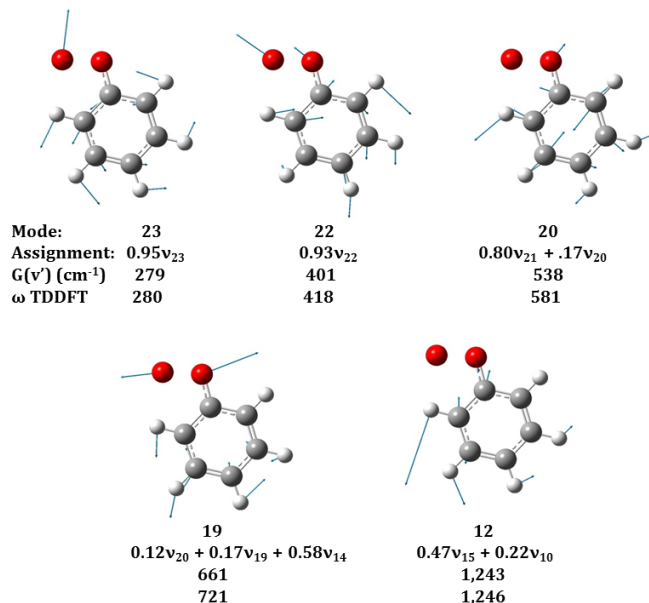


Figure 3.13: Excited state normal modes responsible for the observed progressions in the  $\tilde{B}^2A'' \leftarrow \tilde{X}^2A''$  vibronic spectrum of phenylperoxy. The experimental term values are compared with the harmonic vibrational frequencies calculated by TD-DFT/aug-cc-pVTZ.

Similar geometric changes were predicted for the  $\tilde{C}^2A'' \leftarrow \tilde{X}^2A''$  transition. Again there was an increase in the O-O bond length, and decreases in the CO bond length, O-O-C angle,  $C_2 - C_1 - C_6$  angle (cf., Tables B.2 and B.3, Appendix). Theoretical simulation of the  $\tilde{C}^2A'' \leftarrow \tilde{X}^2A''$  transition produces a prominent origin band at  $21,056 \text{ cm}^{-1}$ , followed by progressions of the O-O stretch and O-O-C bend. In contrast to the behavior of the  $\tilde{B}^2A'' \leftarrow \tilde{X}^2A''$  transition, the vibronic intensity envelope decreases for bands above the origin (see Figure B.1).

The TD-DFT calculations favored assignment of the dominant spectral features of Figure 3.8b to the  $\tilde{B}^2A'' \leftarrow \tilde{X}^2A''$  transition of phenylperoxy. As a further test of the correspondence between the observed and calculated results, the predicted molecular constants were used to simulate the rotational contour of the origin band. The program PGOPHER[226] was used to simulate and fit the contour. In this process the centrifugal distortion and spin-rotation constants were set to zero. The rotational constants and transition moment projections were fixed. For comparison with the experimental contour, the band origin, rotational temperature and Lorentzian line width were treated as variable parameters. The results from both the double- $\zeta$  and triple- $\zeta$  basis sets were used. The smooth curves in Figure 3.9 show the best fit contours, and the molecular constants are given in the figure caption. Note that the fit for the DZ constants is better than that for TZ, mostly due to the relative changes in the rotational constants on excitation (more influential than the slight difference in the transition moment projections). The analysis based on the DZ rotational constants yielded a band origin of  $17,519 \text{ cm}^{-1}$ , a rotational temperature of 34 K, and a homogeneous line width of  $2.2 \text{ cm}^{-1}$ . The last parameter shows that the resolution of the contour was limited by lifetime broadening.

Rotational contour modeling was also carried out using the molecular constants for the  $\tilde{C}^2A'' \leftarrow \tilde{X}^2A''$  transition, which included transition dipole moment projections of  $\mu_a = 0.513$  and  $\mu_b = 0.460$  D. This ratio of projections consistently produced

contours where the relative intensities of the P- and R-branch were reversed relative to the experimental spectrum.

The assignment of Figure 3.8b provided by the theoretical model indicated that the spectrum is dominated by transitions from the zero-point level. In contrast, the room temperature spectrum of the  $\tilde{A} \ ^2A' \leftarrow \tilde{X} \ ^2A''$  transition reported by Just *et al.*[238] included hot bands, resulting in repeated patterns of sequence bands where successive members were separated by just  $30 \text{ cm}^{-1}$ . These were attributed to a population of a ground state vibrational mode ( $\nu_{33}$ ) that had a frequency of about  $85 \text{ cm}^{-1}$ . For the present measurements, if the vibrational temperature for the low frequency modes was close to the rotational temperature, the lowest energy vibrationally excited state would have a fractional population of just 3%. Hence, the absence of obvious hot bands was reasonable.

If it is accepted that the broad absorption feature previously reported[80, 81, 230] in the  $18,850 - 20,200 \text{ cm}^{-1}$  range does belong to phenylperoxy, then the results from this study may be used to account for the lack of structure. This energy region of Figure 3.8b is quite congested, despite the simplification resulting from jet cooling. The features appear to be broader at these energies, occurring in clumps that are suggestive of the mixing of bright and dark states. For the room temperature spectrum we anticipate a considerable increase in congestion resulting from hot band transitions. Typically, the rates of nonradiative decay processes increase with vibronic excitation, so the homogeneous line widths will be in excess of  $2 \text{ cm}^{-1}$ . Add to this the broadening of the rotational contours produced by the greater range of rotational levels populated, and it is quite plausible that the combined effect will be a nearly continuous spectrum.

There are no reports of room temperature gas phase CRDS measurements for phenylperoxy in the region  $17,500 - 18,100 \text{ cm}^{-1}$ . In future experiments it will be of interest to see if vibrationally resolved data can be obtained for the lower energy

bands. If so, this will provide a more species specific method for observing phenylperoxy in kinetic studies. The conventional wisdom is that phenylperoxy would be a poor candidate for detection by laser induced fluorescence, and this is confirmed for the  $\tilde{B}^2A'' \leftarrow \tilde{X}^2A''$  transition. The line width of the origin band indicates a nonradiative decay rate of  $4 \times 10^{11} \text{ s}^{-1}$ , which would result in a fluorescence quantum yield on the order of  $3 \times 10^{-5}$ .

### 3.3 Conclusion

Jet-cooled spectra for the  $\tilde{B}^2A_2 \leftarrow \tilde{X}^2B_1$  transition of the phenoxy radical and the  $\tilde{B}^2A'' \leftarrow \tilde{X}^2A''$  transition of the phenylperoxy radical have been recorded using CRDS. The vibronically resolved spectral simulations from Gaussian provided reasonable agreement with experimental spectra for each species. Rotationally resolved spectra for each species could not be produced by jet-cooled methods as each transition was limited by lifetime broadening. For the phenoxy radical, this nonradiative decay could occur through either rapid internal conversion to the  $\tilde{A}^2B_2$  state (assuming a vibronically allowed relaxation) or thermal decomposition to the cyclopentadienyl radical (plus carbon monoxide)[64, 192]. For the phenylperoxy radical this broadening could arise as a result of rapid internal conversion to the  $\tilde{A}^2A'$  state (symmetry allowed)[238] or through decomposition to the phenoxy radical and continue through several intermediates states to the cyclopentadienyl radical[61, 236, 237].

The  $\tilde{B}^2A_2 \leftarrow \tilde{X}^2B_1$  transition of the phenoxy radical consists of a  $516 \text{ cm}^{-1}$  progression of four vibronic bands, assigned to the  $\nu_{11}$  totally symmetric in-plane CC stretching/bending mode, consistent with previous theoretical studies[190, 191, 210]. Small shoulders on the red shaded region of the observed vibronic bands were assigned to the  $\nu_{20_1}^1$  and  $\nu_{20_2}^2$  hot bands, as previously reported by Araki *et al.*[212]. This transition has been assigned as  $\pi - \pi^\circ$  based on the results presented here.

This assignment is supported by electronic structure calculations (TD-DFT) and by comparison of these calculations with those by Cheng *et al.*[189].

The  $\tilde{B}^2A'' \leftarrow \tilde{X}^2A''$  transition of the phenylperoxy is dominated by five vibrational modes, each of which have strong displacement attributed to O-O stretching or in-plane bending. The high density of vibronic modes observed experimentally, coupled with lifetime broadening, explains the lack of structure observed in room temperature spectra attributed to the phenylperoxy radical[80, 81, 230]. The lower energy region of this transition (17,500 - 18,100  $\text{cm}^{-1}$ ) is less congested than the higher energy region. It is plausible that this region may show more resolvable vibrational structure at room temperature. If so, this could provide an accurate signature of phenylperoxy in future kinetics studies.

# Chapter 4

## Laser Induced Fluorescence (LIF) of Calcium Metal Oxides

### 4.1 Calcium Oxide

This section is taken from Stewart *et al.*[245]. Access provided by Elsevier.

#### 4.1.1 Introduction

In this study we have examined the electronic spectrum of CaO in the 29,800 - 33,150  $\text{cm}^{-1}$  energy range. This work was carried out in order to identify vibronic levels that will be suitable for two-photon pulsed-field ionization zero kinetic energy photoelectron characterization of the  $\text{CaO}^+$  ion (similar to a previously reported study of  $\text{BaO}^+$  [246]). The spectra obtained have provided data for CaO that extend the range of vibronic levels for two known electronically excited states, and revealed a few additional levels that arise from a state of  $0^+$  symmetry.

The electronic spectrum of CaO is notoriously congested and complex [247, 248, 249, 250, 251, 252, 253, 254, 255, 256]. Field and co-workers[256] have developed a very instructive atomic-ions-in-molecules model that provides configurational assignments

for the lower energy electronic states. The  $X^1\Sigma^+$  ground state is uniquely assigned to the  $\text{Ca}^{+2}\text{O}^{2-}$  configuration. The lower energy excited states are then approximated as various configurations of the  $\text{Ca}^+ + \text{O}^-$  pair, with an electron localized on Ca and a hole localized on O. All of the previously observed excited electronic states of CaO can be mapped as combinations of molecular states from CaF[257] (which is a model for the electronic structure of the  $\text{Ca}^+$  ion) and NaO[258] (which is a model for the electronic structure of the  $\text{O}^-$  ion). The  $\text{Ca}^+ X\sigma$ ,  $A\pi$ , and  $B\sigma$  configurations correspond to the  $X^2\Sigma^+$ ,  $A^2\Pi^+$ , and  $B^2\Sigma^+$  states of CaF. For  $\text{O}^-$ , the  $\pi^-$  and  $\sigma^-$  configurations correspond to the  $X^2\Pi$  and  $A^2\Sigma^+$  states of NaO. The configurations of these atomic ions combine to give electronic configurations of the CaO molecule. As an example, the first excited singlet state is  $A'^1\Pi$ , which arises from the  $X\sigma\pi^-$  configuration. There have been several high-level theoretical studies of the electronic states of CaO[259, 260, 261, 262, 263, 264, 265], mostly focused on the ground and low-lying excited states. Overall, the electronic structure calculations support the atomic-ions-in molecules model of Field and co-workers[256].

The present results extend the range of observed vibrational levels for the  $C^1\Sigma^+$  and  $F^1\Pi$  states. These excited states have been attributed to the  $B\sigma\sigma^-$  and  $B\sigma\pi^-$  configurations. Data for the  $C^1\Sigma^+$  state were obtained by Lagerqvist[251] who observed the  $\nu'=0-3$  levels in emission spectra for the  $C^1\Sigma^+ - X^1\Sigma^+$  transition. Baldwin and Field[266] characterized the 0-0 origin band of the  $F^1\Pi \leftarrow A'^1\Pi$  transition, which provided the only experimental data available for the  $F^1\Pi$  state. Three other vibronic levels were observed, where the rotational structure was consistent with an electronic state of  $0^+$  symmetry. One of these levels interacts strongly with the  $C^1\Sigma^+ \nu'=7$  level.

### 4.1.2 Methods

Figure 4.1 shows the instrument used to record the laser induced fluorescence (LIF) spectrum of CaO.

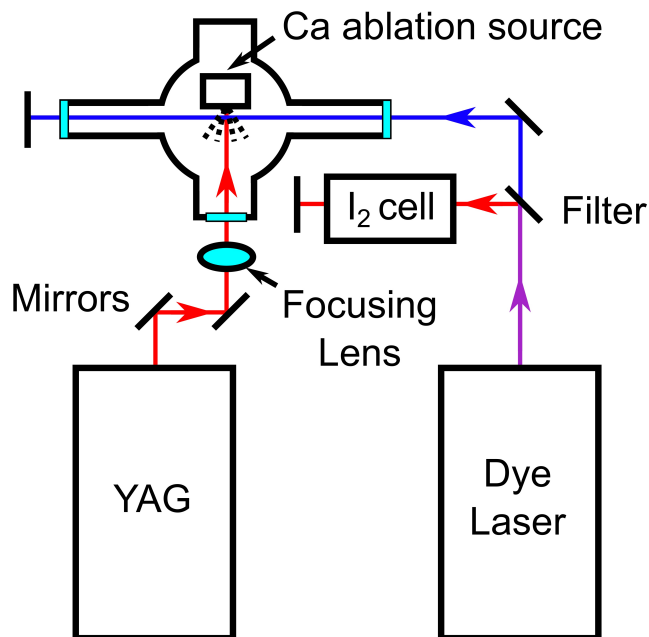


Figure 4.1: Apparatus used to record the LIF spectrum of CaO.

To produce CaO, 1064 nm light from a pulsed Nd:YAG laser (Quanta-Ray, DCR-1A) was focused onto a calcium rod (ESPI Metals, 99.9% pure) to ablate Ca into the gas phase. The calcium rod was continuously rotated and translated using a stepper motor to ensure that a fresh surface of metal was used for each ablation shot. The ablated material was entrained in a pulse of helium carrier gas at  $\sim 10$  atm backing pressure. The He contained a small amount of N<sub>2</sub>O ( $\sim 0.2\%$ ) to provide a source of oxygen for production of CaO. The ideal conditions for producing CaO were obtained when the Nd:YAG laser was operated at low power, just above the lasing threshold. The gas pulses were produced using a Parker-Hannifin General Valve (Series 99), with a pulse duration of 500  $\mu$ s. After traveling through a short channel (2 mm diameter,

$\sim 6$  mm long) the gas exited the ablation source into a vacuum chamber, forming a supersonic expansion. The expansion source was based on designs by Scherer[267]. The vacuum was maintained using a Roots blower (Leybold, RUVAC WSU 251) backed by a rotary vane pump (Leybold, TRIVAC D65B). The background pressure in the chamber was typically  $<10$  mTorr.

Once the molecules were formed in the supersonic expansion, they were probed using light from a tunable pulsed dye laser (Lambda Physik, FL3002) pumped by a XeCl excimer laser (Lambda Physik, EMG201). The laser was operated at 10 Hz with a nominal pulse duration of 10 ns. To generate tunable UV light, the output of the dye laser was frequency doubled using a BBO crystal (Lambda Physik, FL30). The linewidth of the doubled light was  $\sim 0.4$   $\text{cm}^{-1}$  when the dye laser operated without an intracavity etalon, and  $\sim 0.1$   $\text{cm}^{-1}$  when the etalon was used. The fundamental light from the dye laser was directed through an iodine cell for absolute wavenumber calibration using the B-X transition. Calibration was performed by comparing the measured iodine spectra to the iodine atlas reported by Salami and Ross[268]. The frequency accuracy of the fundamental light was  $\sim 0.03$   $\text{cm}^{-1}$  without the intra-cavity etalon and  $\sim 0.01$   $\text{cm}^{-1}$  when the etalon was used.

The UV light passed through a short-pass filter (to block the fundamental) and was sent into the vacuum chamber, where the laser light crossed the supersonic expansion  $\sim 2.5$  cm downstream from the nozzle. A two-lens telescope was situated beneath the expansion, perpendicular to both the expansion and the probe laser, to collect fluorescence and focus it onto a photomultiplier tube (PMT, Hamamatsu R889). A long pass filter was added between the focusing assembly and the PMT to block scattered light from the dye laser. The signal from the PMT was sent to two boxcar integrators (Stanford Research Systems, SR250), time-gated to integrate over the fluorescence signal and the background signal, respectively. The outputs from the boxcar integrators were sent to an analog processor (Stanford Research Systems,

SR235) where the background signal was subtracted from the fluorescence signal. The subtracted signal was then sent to a computer, where it was recorded using a data acquisition card (National Instruments, USB-6210). A custom LabVIEW program was used to control the data acquisition and display. Timing for all of the instruments was maintained using a delay generator (Stanford Research Systems, DG535) that was referenced to the 10 Hz internal frequency standard of the Nd:YAG laser. The optimal delays for observing CaO were to fire the ablation laser  $\sim 600 \mu\text{s}$  after opening the pulse valve, and then fire the probe laser  $24 \mu\text{s}$  after the ablation laser. Note that the pulsed valve opens approximately  $350 \mu\text{s}$  after the trigger signal from the delay generator due to mechanical delay in pneumatic components. Firing the pulsed valve in this way ensures that there is strong overlap with the laser ablation and gas pulses.

To record the spectrum of CaO, the wavelength of the dye laser was stepped sequentially in 0.003 nm steps in the fundamental wavelength (without the intra-cavity etalon) or  $\sim 0.0005$  nm steps in the fundamental wavelength (with the intra-cavity etalon). The boxcar integrators were set to average 30 shots from the laser. The laser was fixed at each wavelength step for 6 s to allow sufficient time for averaging.

### 4.1.3 Results and Discussion

Figure 4.2 shows a low-resolution survey scan of the CaO spectrum. An example of two bands recorded at a higher resolution (using the intra-cavity etalon) is shown in Figure 4.3. All of the bands observed had rotational structures that were consistent with  $^1\Sigma^+ - ^1\Sigma^+$  or  $^1\Pi - ^1\Sigma^+$  transitions. The program PGOPHER[226] was used to analyze the rotational structures. The spectra were rotationally cold, but the temperature varied significantly depending on the source conditions. Rotational temperatures ranged from as low as  $\sim 10$  K to as high as  $\sim 100$  K.

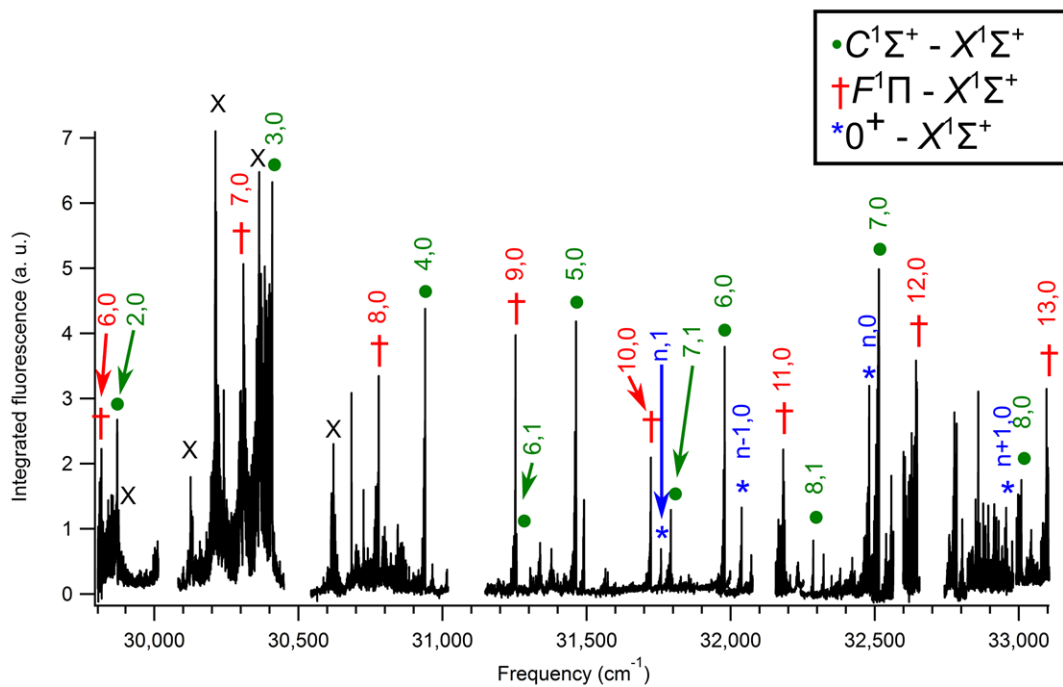


Figure 4.2: Low resolution survey scan showing rovibronic bands of CaO. The bands marked with X are from CaOH[269].

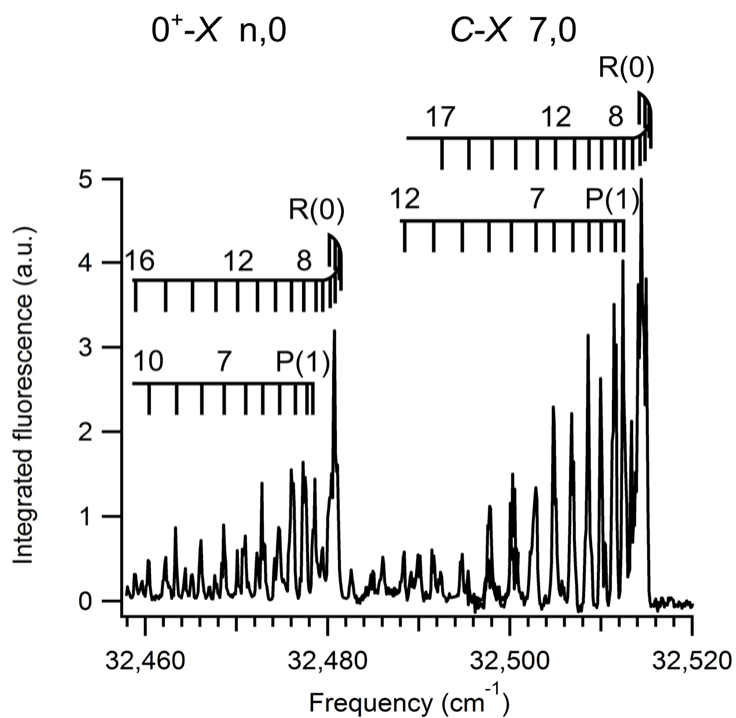


Figure 4.3: Rotationally resolved scan of the  $C^1\Sigma^+ - X^1\Sigma^+$ , 7-0 and  $0^+ - X^1\Sigma^+$ , n-0 bands of CaO.

Vibrational progressions were readily identified in the survey spectrum (indicated by the symbols  $\bullet$ ,  $\dagger$  and  $*$  in Figure 4.2). The C  $^1\Sigma^+$  - X  $^1\Sigma^+$  2-0 and 3-0 bands, previously reported by Lagerqvist[251], were evident in the lower energy part of the spectrum. Compared to the published results, our rotational line positions for these bands were within the experimental uncertainties. Scanning to higher energies it was possible to follow the C  $^1\Sigma^+$  - X  $^1\Sigma^+$   $\nu' - 0$  progression up to  $\nu'=8$ . A few hot-bands originating from  $\nu''=1$  were also observed. Molecular constants derived from the C  $^1\Sigma^+$  - X  $^1\Sigma^+$  bands are collected in Table 4.1.

Table 4.1: Fitted molecular constants for the C  $^1\Sigma^+$  - X  $^1\Sigma^+$  bands of CaO

$\nu'$	$T_{\nu',0}$	$B_{\nu'}$
2	29,869.8(1)	0.3652(6)
3	30,407.2(1)	0.3620(5)
4	30,938.2(2)	0.355(1)
5	31,461.8(1)	0.3540(8)
6	31,977.6(2)	0.349(1)
7 <sup>a</sup>	32,513.5(2)	0.3306(7)
8 <sup>a</sup>	33,007.5(1)	0.3439(7)

All values are in units of  $\text{cm}^{-1}$ . The numbers in parentheses indicate the  $1\sigma$  errors.

<sup>a</sup>Strongly perturbed bands

In fitting these bands we fixed the ground state rotational constants at the values reported by Focsa *et al.*[248] ( $B_0'' = 0.4428$ ,  $B_1'' = 0.4395 \text{ cm}^{-1}$ ). Vibrational constants were obtained by fitting the band origins to the expression

$$T_{\nu',0} = T_{0,0} + \omega_e'\nu' - \omega_e\chi_e'\nu'(\nu' + 1) \quad (4.1)$$

The band origins for the  $\nu'=0$  and 1 levels were taken from Lagerqvist[251]. Levels with  $\nu' \geq 7$  were not included in this fit as they were clearly perturbed. Refined vibrational constants for the C state are listed in Table 4.2. The origins for the 7-0

and 8-0 bands were 26.6 and 18.8  $\text{cm}^{-1}$  above the energies predicted by extrapolation based on the constants of Table 4.2.

Table 4.2: Equilibrium electronic and vibrational constants for the C  $^1\Sigma^+$  and F  $^1\Pi$  states of CaO

	C $^1\Sigma^+$ (this work) <sup>a</sup>	C $^1\Sigma^+$	F $^1\Pi$
$T_{0,0}$	28,772.7(5)	28,772.4	26,794.5(11)
$\omega_e$	559.4(4)	560.9	521.3(3)
$\omega_e\chi_e$	3.61(6)	4.0	2.59(3)
Error	0.4	-	1.0

All values are in units of  $\text{cm}^{-1}$ . The numbers in parentheses indicate the  $1\sigma$  errors.

<sup>a</sup>This fit includes the previously reported band centers from Lagerqvist[251] as well as the data reported in this work. This fit only includes the levels from  $\nu = 0-6$  because there are significant perturbations for  $\nu = 7-8$ , as discussed in the text.

The progression of bands marked by the symbol † in Figure 4.2 exhibited the typical rotational structure for a  $^1\Pi - ^1\Sigma^+$  transition. To assign these features we began by fitting the rotational lines to obtain the band origins. In the first cycle of fitting both the lower and upper state rotational constants were allowed to vary. From these fits it was clear that all of the bands originated from the X,  $\nu''=0$  level. In the second fitting cycle the ground state rotational constant was fixed at the value given by Focsa *et al.*[248]. Band origins and upper state rotational constants from these fits are listed in Table 4.3. The lambda doublet splitting for the  $^1\Pi$  state did not produce a significant combination defect at the resolution of our measurements. Similarly, the short range of rotational levels observed did not permit the extraction of significant centrifugal distortion constants, with the exception that the fit of the band at 30,299.5  $\text{cm}^{-1}$  was improved by including a negative distortion constant of  $D' = -1.44(8) \times 10^{-5} \text{ cm}^{-1}$ . It is likely that this constant was compensating for the effects of a local perturbation.

Table 4.3: Fitted molecular constants for the F  $^1\Pi$  - X  $^1\Sigma^+$  bands of CaO

$\nu'$	$T_{\nu',0}$	$B_{\nu'}$
6	29,815.4(1)	0.3254(5)
7 <sup>a</sup>	30,299.5(2)	0.319(1)
8	30,777.7(1)	0.3163(7)
9	31,252.2(1)	0.3145(7)
10	31,722.0(1)	0.3107(4)
11	32,186.5(1)	0.3091(4)
12	32,646.0(1)	0.3081(4)
13	33,101.2(1)	0.3113(4)

All values are in units of  $\text{cm}^{-1}$ . The numbers in parentheses indicate the  $1\sigma$  errors.

<sup>a</sup>The fit for  $\nu = 7$  also included a centrifugal distortion constant,  $D = -1.44(8) \times 10^{-5} \text{ cm}^{-1}$ .

As there are two known  $^1\Pi$  states close enough to the energy range of Figure 4.2 to be considered for the upper state assignment (B and F)[266], we examined the possibility that the new bands were part of the B-X or F-X band systems. This was accomplished by fitting Equation 4.1 to the band origins. The vibrational numbering was adjusted to obtain  $T_{0,0}$  values that were closest to that of the B (25,913.0  $\text{cm}^{-1}$ ) or F (26,794.7  $\text{cm}^{-1}$ ) states. Using the vibrational numbering of Table 4.3, the extrapolated  $T_{0,0}$  value was 26,812(2)  $\text{cm}^{-1}$ , just 18  $\text{cm}^{-1}$  above the established value for the F state. The smallest difference for the B state was -140  $\text{cm}^{-1}$ , obtained by increasing the vibrational numbering of Table 4.2 by 2 units. This extrapolation procedure was close enough to assign the new bands to the F-X transition. Consequently, a new fit was made with inclusion of the F state  $T_{0,0}$  value from the study of Baldwin and Field[266]. The resulting vibrational constants are listed in Table 4.2. The standard deviation for this fit was 1.0  $\text{cm}^{-1}$ , which we consider to be acceptable as several levels are likely to be influenced by local perturbations.

The bands marked with the symbol \* in Figure 4.2 showed simple P and R branch rotational structure, consistent with a  $^1\Sigma^+ - ^1\Sigma^+$  transition. Based on the lower state

rotational constants, the three bands above 32,000  $\text{cm}^{-1}$  originated from X,  $\nu''=0$  while the band at 31,757.1  $\text{cm}^{-1}$  was from  $\nu''=1$ . The fitted molecular constants for these bands are listed in Table 4.4.

Table 4.4: Fitted molecular constants for the  $0^+ - X \ ^1\Sigma^+$  bands of CaO

$\nu'$	$T_{\nu',0}$	$B_{\nu'}$
n - 1	32,037.0(2)	0.316(1)
n <sup>a</sup>	32,479.5(2)	0.330(1)
n + 1	32,955.2(5)	0.313(3)

All values are in units of  $\text{cm}^{-1}$ . The numbers in parentheses indicate the  $1\sigma$  errors.  
<sup>a</sup>Strongly perturbed.

The higher energy bands appeared to be a short progression, with asymmetric intervals of 442.5 and 475.7  $\text{cm}^{-1}$ . This pattern suggests that there is a relatively strong perturbation. Figure 4.3 shows the rotational structures of the 32,479.5  $\text{cm}^{-1}$  band and the nearby C  $^1\Sigma^+ - X \ ^1\Sigma^+$  7-0 band. The latter is also strongly perturbed. In addition, the rotational constant for C,  $\nu'=7$  was anomalously small compared to the trend of the rotational constants for the lower energy vibrational levels (c.f., Table 4.1). The extrapolated energy for the C,  $\nu'=7$  level, 32,496.4  $\text{cm}^{-1}$ , is very close to the mid-point between the \* bands at 32,037.0 and 32,955.2  $\text{cm}^{-1}$  (32,496.1  $\text{cm}^{-1}$ ), making it feasible that the vibronic state at 32,479.5  $\text{cm}^{-1}$  and the C,  $\nu'=7$  level (Figure 4.3) are mutually perturbing. Consequently, these bands were analyzed using a homogeneous perturbation model as implemented by the PGOPHER software. This fit yielded deperturbed values of  $T(\text{C})_{7,0} = 32,496.7(2)$ ,  $B'_7 = 0.3521(6)$ ,  $T(*)_{x,0} = 32,496.3(2)$ ,  $B'_x = 0.3087(7)$ , and a perturbation matrix element of 17.00(1) $\text{cm}^{-1}$ .

The  $T(*)_{x,0}$  value was consistent with the expectation based on the mid-point of the flanking \* bands (just 0.6  $\text{cm}^{-1}$  away). However, the deperturbed C,  $\nu'=7$  origin was still 8.9  $\text{cm}^{-1}$  above the extrapolated position. This pattern suggests that a third

state is involved in the perturbation. To test the viability of this assumption we examined a Hamiltonian matrix of the form,

$$H = \begin{pmatrix} E_0(0^+, \nu' = x) & m_1 & 0 \\ m_1 & E_0(C, \nu' = 7) & m_2 \\ 0 & m_2 & E_0(\alpha) \end{pmatrix}$$

where  $E_0(C, \nu'=7)$  is the energy obtained by extrapolation, using the constants from Table 4.2,  $E_0(0^+, \nu'=x)$  is the energy from the two state deperturbation model, and  $E_0(\alpha)$  is the unperturbed vibronic energy of the third state. The homogeneous perturbation elements are given by  $m_1$  and  $m_2$ , and it is assumed that the direct interaction between  $0^+, \nu'=x$  and  $\alpha$  is negligible. The eigenvalues of this Hamiltonian reproduce the observed band origins using the parameters  $m_1 = 19.8$ ,  $m_2 = 13.0$  and  $E_0(\alpha = 32,469.0 \text{ cm}^{-1})$ . The last two parameters are strongly correlated, and therefore somewhat arbitrary. The primary significance of this exercise is that it demonstrates that the band origin shifts can be explained using a three-state model with physically reasonable parameter values.

Next we consider a possible electronic assignment for the \* bands. The short progression of these bands runs almost in step with the C-X bands, indicating that the two states have quite similar potential energy curves. Hence, a possible candidate for the electronic assignment is the  $C' \ ^1\Sigma^+$  state, derived from the  $A\pi\pi^-$  configuration. Previously, the  $\nu''=0$  and 1 levels of  $C' \ ^1\Sigma^+$  were observed by Baldwin and Field[270] via the  $C \ ^1\Sigma^+ - A' \ ^1\Pi$  transition. To test the viability of the assignment we have fitted the term energies  $(T'(C')_{\nu',0})$  using the  $\nu'=0$  and 1 values from Baldwin and Field[270], and the present data for  $(T'(*)_{\nu',0})$  with  $\nu' = n-1, n,$  and  $n+1$  to Equation 4.1. The deperturbed origin was used for  $\nu' = n$  and the value for  $n$  was treated as a variable. A reasonable fit was achieved for  $n = 16$  (standard deviation of  $\sigma = 7.8 \text{ cm}^{-1}$ ), and the fitting was improved ( $\sigma = 0.06 \text{ cm}^{-1}$ ) by including a second anharmonicity constant.

The resulting molecular constants were  $(T(C')_{0,0}) = 24,363.3(1)$ ,  $\omega_e = 555.4(2)$ ,  $\omega_e\chi_e = 5.48(3)$ ,  $\omega_e y_e = 0.103(1)$   $\text{cm}^{-1}$ . These values seem reasonable, but there are other viable assignments such as the  $g^3\Pi(0^+)$  and  $e^3\Sigma^-(0^+)$  states[254]. It is hoped that future studies of the dispersed fluorescence spectra and fluorescence decay lifetimes will shed further light on the upper state of the \* bands.

## 4.2 Calcium Hydroxide

### 4.2.1 Introduction

The characteristics of group IIA alkaline earth hydroxides has long been of substantial interest in chemistry. When introduced to a flame source they produce a wide variety of colors[271, 272]. The group IIA hydroxides are also of interest in astrochemistry. They are predicted to exist in high abundances in late stage oxygen rich stars[273], and possibly circumstellar clouds[274].

The electronic structure and characteristics of these hydroxides have been the subject of numerous experimental[273, 275, 276, 277, 278, 279, 280, 281] and theoretical studies[282, 283, 284, 285]. The lighter hydroxides, BeOH and MgOH, were originally expected to have strong covalent character in the ground electronic state, with a bent geometry[282, 284, 285, 286]. It was later shown that MgOH is quasilinear[279]. Until recently, experimental data for BeOH necessary to ascertain the nature of bonding in the ground electronic state was lacking. A recent study by our group proved that the ground state is bent, with a barrier to linearity just above the vibrational zero point energy level[287]. The heavier members of the group all have linear equilibrium geometries in their ground electronic state[282]. In CaOH this is due to a strong ionic character arising from a closed shell OH<sup>-</sup> and Ca<sup>+</sup> containing an unpaired 4s electron with a closed shell argon core. The excited electronic states arise from excitation of the unpaired electron on the calcium atom to higher lying *ns*, *np*, and *nd* orbitals on

the metal. It is clear the nature of bonding in these metal hydroxides is dependent on the ionization energy of the metal. The electronic structure of CaOH is valuable in the development of an accurate model describing the bonding characteristics in the group IIA metal hydroxides as it represents the first strongly ionic species in the series.

The electronic spectrum of calcium hydroxide (CaOH) was first observed in 1983 by Hilborn *et al.*[288] using a Broida type oven source[289]. In this study they observed the  $\tilde{A} \ ^2\Pi - \tilde{X} \ ^2\Sigma^+$  electronic spectrum of CaOH, which was discovered to have a linear equilibrium geometry in each electronic state. The same result was noted for the deuterated species, CaOD, as well. Bernath and Brazier[290] recorded this band in higher resolution, and subsequently obtained molecular constants with higher accuracy. The  $\tilde{B} \ ^2\Sigma^+ - \tilde{X} \ ^2\Sigma^+$  transition was first observed by Wormsbecher *et al.* using chemiluminescence[291]. Rotational structure of vibronic bands attributed to the  $\tilde{B} \ ^2\Sigma^+ - \tilde{X} \ ^2\Sigma^+$  transition was later reported by Bernath *et al.*[290, 292]. The electronically forbidden  $\tilde{C} \ ^2\Delta - \tilde{X} \ ^2\Sigma^+$  transition was first observed by Jarman and Bernath[293], and later by Jakubek and Field[294], which is allowed through vibronic coupling of the Ca-O-H bending mode. Rotational constants in the  $\tilde{X} \ ^2\Sigma^+$  state of CaOH have been reported for the ground and several excited vibrational states in a series of microwave studies performed by Ziurys and co-workers[273, 276, 295, 296].

In 1996 Pereira and Levy observed the  $\tilde{D} \ ^2\Sigma^+ - \tilde{X} \ ^2\Sigma^+$ ,  $\tilde{E} \ ^2\Sigma^+ - \tilde{X} \ ^2\Sigma^+$ , and  $\tilde{F} \ ^2\Pi - \tilde{X} \ ^2\Sigma^+$  transitions of CaOH by laser ablation of a calcium rod[269]. LIF and resonantly enhanced multiphoton ionization (REMPI) spectra revealed the presence of several vibronic bands they assigned to the aforementioned electronic transitions. The  $\tilde{D} \ ^2\Sigma^+$  and  $\tilde{E} \ ^2\Sigma^+$  states were noted to have a linear geometry at their equilibrium. Rotational constants for the  $\tilde{D} \ ^2\Sigma^+$  state were extracted from the observed bands. Assuming that the Ca-O-H bond length in the  $\tilde{D} \ ^2\Sigma^+$  state is equal to that of the  $\tilde{A} \ ^2\Pi$  state, the Ca-OH bond length was determined. Both the  $\tilde{D} \ ^2\Sigma^+$  and  $\tilde{E} \ ^2\Sigma^+$  states are more

strongly bound than the ground state. The observed origin band of the  $\tilde{F}$  state was the outlier in this study as it possessed P, Q, and R branch structure. Coupled with the activity seen in the bending vibrational modes from corresponding emission spectra, Pereira and Levy assigned this state to a bent geometry with significant covalent character. This is the first noted observation for a electronic state with bent geometry in CaOH. The results from this study prompted Hailey *et al.*[297] to publish an earlier study of the  $\tilde{G}$   $^2\Pi$  state of CaOH and CaOD using optical-optical double resonance spectroscopy. They discovered several vibronic bands at moderate resolution. Using the molecular constants extracted from these bands, the  $\tilde{G}$   $^2\Pi$  state was assigned as having a linear geometry. This is unusual as the  $\tilde{F}$  band observed by Pereira and Levy was assigned to a bent geometry. Following these studies Theodorakopoulos *et al.*[283] calculated the potential energy surfaces for the doublet excited electronic states of CaOH at the multireference double excitations configuration interaction (MRCI) level of theory. Their results found that the minimum energy geometry of the  $\tilde{F}$   $^2\Pi$  state is linear, with a nearby local minimum having a bent geometry of  $175^\circ$  ( $^2A'$ ,  $C_s$  symmetry) and a  $92\text{ cm}^{-1}$  barrier to linearity for this local minima. This conclusion was supported shortly afterward by Taylor *et al.*[298], where in their study the bent local minimum for the  $\tilde{F}$   $^2\Pi$  state is predicted to be  $376\text{ cm}^{-1}$  above the global minimum at a bond angle of  $175^\circ$  and a  $105\text{ cm}^{-1}$  barrier to linearity of the local minima. They found that the  $\tilde{G}$   $^2\Pi$  is also linear in nature, with a local bent minimum at  $524\text{ cm}^{-1}$  above the global minimum and a  $50\text{ cm}^{-1}$  barrier to linearity (of the local minima). At the minimum energy linear geometry, the  $\tilde{E}$   $^2\Sigma^+$ ,  $\tilde{F}$   $^2\Pi$ , and  $\tilde{G}$   $^2\Pi$  states lie close in energy. As the geometry changes to a bent configuration, and the symmetry changes from  $C_{\infty v}$  to  $C_s$ , extensive mixing occurs between the three states. The character of the  $\tilde{F}$   $^2\Pi$  state is strongly dependent on the  $\tilde{E}$   $^2\Sigma^+$ , in which an avoided crossing is predicted between the two states at approximately  $175^\circ$ .

At this time, there are no additional experimental studies for the  $\tilde{E}$   $^2\Sigma^+$  and  $\tilde{F}$   $^2\Pi$

states of CaOH. During the course of the CaO experiments outlined in Section 4.1, we observed several vibronic bands of these excited electronic states first reported by Peireira and Levy. In this section results from these studies are reported. High resolution LIF scans were obtained for the  $\tilde{E} \ ^2\Sigma^+ - \tilde{X} \ ^2\Sigma^+$  transition. Molecular constants from these bands were determined using PGOPHER, which confirm the preliminary results of Peireira and Levy. For the origin band of the  $\tilde{E} \ ^2\Sigma^+ - \tilde{X} \ ^2\Sigma^+$  transition, the spin-rotation constant ( $\gamma$ ) was determined. The origin band of the  $\tilde{F} \ ^2\Pi - \tilde{X} \ ^2\Sigma^+$  was observed at low resolution, which cannot be utilized to confirm the linear geometry in this excited state as predicted by Theodorakopoulos *et al.*[283] and Taylor *et al.*[298].

### 4.2.2 Methods

The experimental setup used to record the vibronic spectra of CaOH is identical to that described in Section 4.1.2. These bands were observed during the course of performing survey scans of CaO vibronic bands. In order to increase the intensity of CaOH bands while simultaneously reducing the signal from CaO, a small amount of water vapor was introduced to the expansion using a sample holder located between the carrier gas source and the pulsed valve. The amount of water required was miniscule, as overfilling the sample holder led to a buildup of CaOH on the calcium rod which blocked the expansion channel, invariably eliminating the ability to perform laser ablation and supersonic expansion within the vacuum chamber. The remaining experimental conditions (distance to the pinhole, backing pressure, N<sub>2</sub>O fraction, etc.) were unchanged from the conditions reported in Section 4.1.2.

### 4.2.3 Results

The subsection of Figure 4.2 featuring the vibronic bands of CaOH is shown in greater clarity in Figure 4.4.

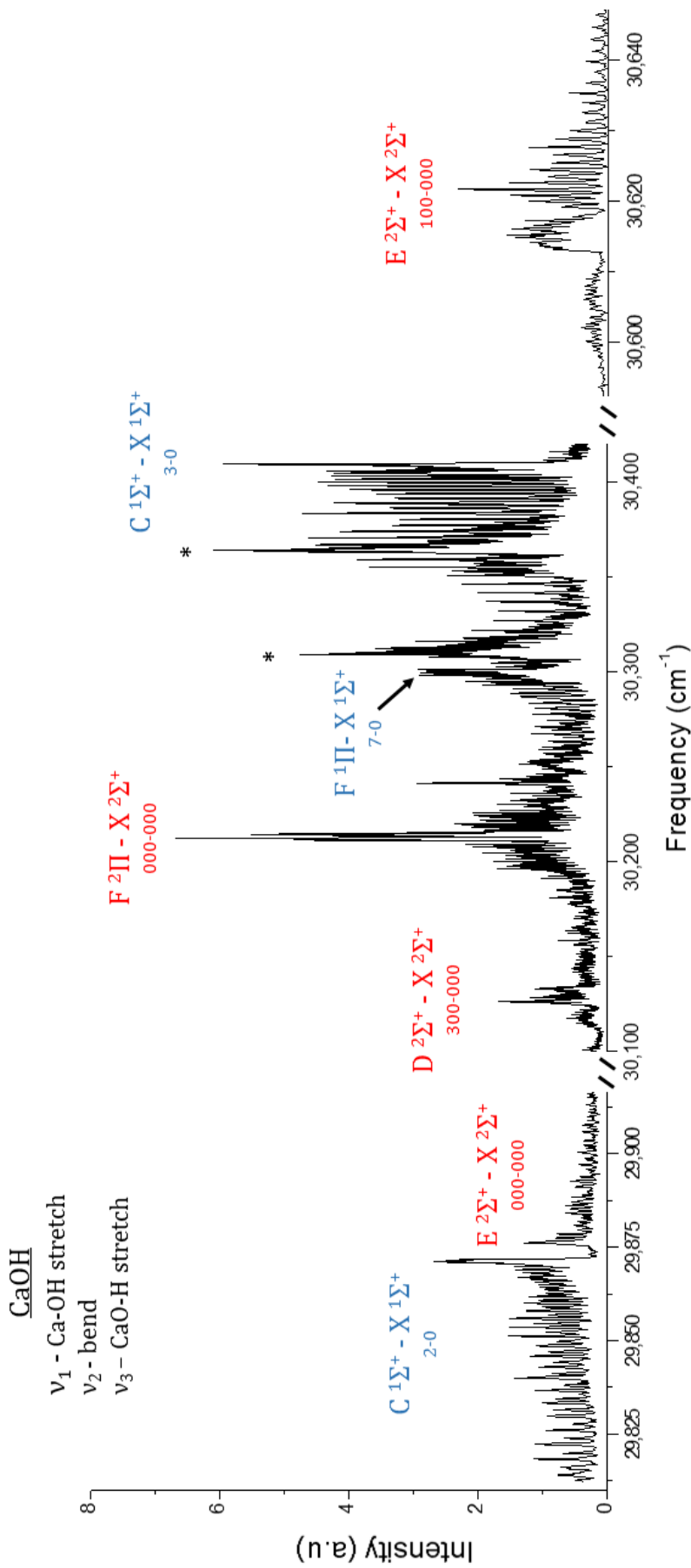


Figure 4.4: Survey scan of vibrionic bands of CaOH observed using LIF. Bands of CaOH are shown in red, while bands of CaO are in blue. The electronic transitions are labeled according to their state designations (top) and populated vibrational levels (below) in the specified electronic states. Vibrational modes of CaOH are defined (top left) as described in the text. The two features labeled as \* denote electronic transitions of CaOH from excited vibrational ground states, as noted by Pereira and Levy[269].

Vibronic bands corresponding to the  $\tilde{D} \ ^2\Sigma^+ - \tilde{X} \ ^2\Sigma^+$ ,  $\tilde{E} \ ^2\Sigma^+ - \tilde{X} \ ^2\Sigma^+$ , and  $\tilde{F} \ ^2\Pi - \tilde{X} \ ^2\Sigma^+$  transitions of CaOH are observed. While the 300-000 band of the  $\tilde{D} \ ^2\Sigma^+ - \tilde{X} \ ^2\Sigma^+$  transition had been observed at rotational resolution, the 000-000 and 100-000 bands of the  $\tilde{E} \ ^2\Sigma^+ - \tilde{X} \ ^2\Sigma^+$  transition had not. Each band exhibits P and R branch rotational structure typical of an excited electronic state of CaOH with linear geometry as previously reported by Pereira and Levy[269]. These bands belong to a Ca-OH stretching progression, and are assigned as 000 (origin band) and 100, where the vibrational modes are arranged in the following order: Ca-OH stretch, bend, CaO-H stretch[269]. No presence of vibronic bands attributed to the bending mode or CaO-H stretch were observed experimentally. The PGOPHER fitting program[226] was used to generate simulated spectra corresponding with the individual vibronic bands, and to extract molecular constants from these bands. The experimental and simulated spectra can be seen in Figures 4.5 and 4.6.

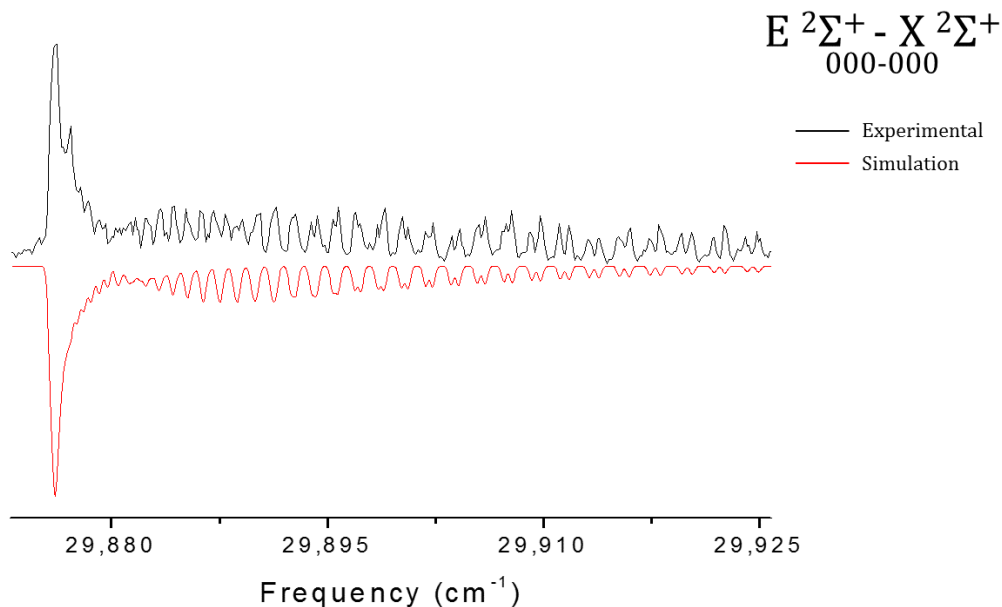


Figure 4.5: Rotationally resolved and simulated spectra of the 000-000 band of the  $\tilde{E} \ ^2\Sigma^+ - \tilde{X} \ ^2\Sigma^+$  transition of CaOH. The simulated spectrum was generated using PGOPHER. The rotational temperature of the simulation is 140K.

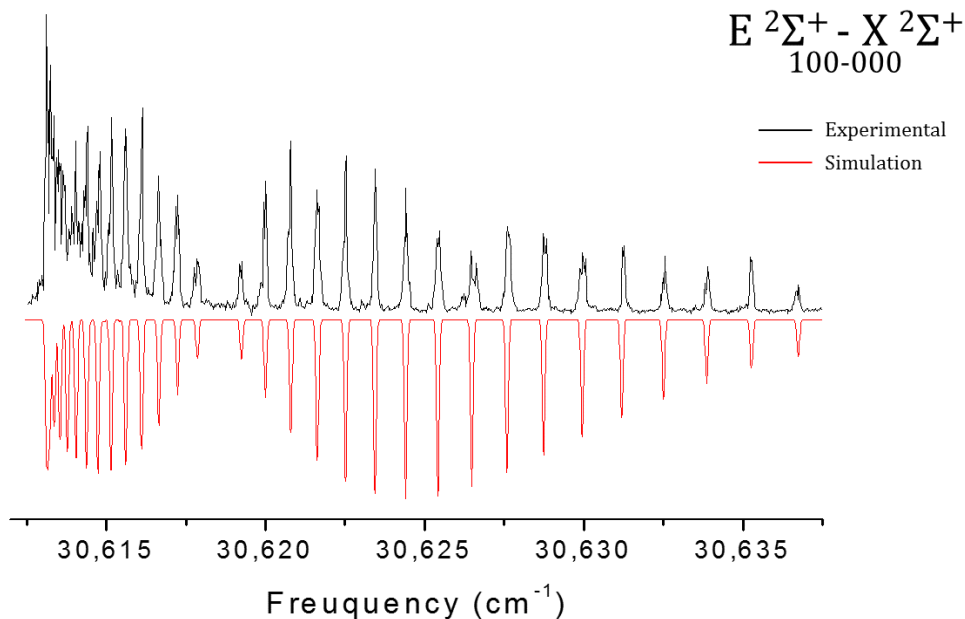


Figure 4.6: Rotationally resolved and simulated spectra of the 100-000 band of the  $\tilde{E} \ ^2\Sigma^+ - \tilde{X} \ ^2\Sigma^+$  transition of CaOH. The simulated spectrum was generated using PGOPHER. The rotational temperature of the simulation is 45K.

Each rotationally resolved band was observed at varying rotational temperatures due to inconsistencies in the expansion source as noted in Section 4.1.2. The vibronic bands of CaOH reported in this section were recorded without the use of the intracavity etalon, with the lone exception being the 100 band shown in Figure 4.6.

Pereira and Levy were unable to definitively assign vibrational progressions of the  $\tilde{E} \ ^2\Sigma^+ - \tilde{X} \ ^2\Sigma^+$  transition due to spectral congestion at higher energies. However in the survey scan (see Figure 4.2) of CaO there are several smaller unassigned vibronic bands in the region where the 200 band of CaOH is expected to appear based on the vibrational spacing between the origin band and the 100 band ( $\sim 738 \text{ cm}^{-1}$ ). Closer examination of this spectral region revealed the presence of three blue shaded vibronic bands with similar characteristics as other vibronic bands of CaOH at low spectral resolution ( $0.4 \text{ cm}^{-1}$ ). Only one of these bands was rotationally resolved at this spectral resolution. Operating under the assumption that this is the 200 band of CaOH, a PGOPHER simulation was generated in order to obtain molecular constants

to accurately assign this vibronic band, shown in Figure 4.7.

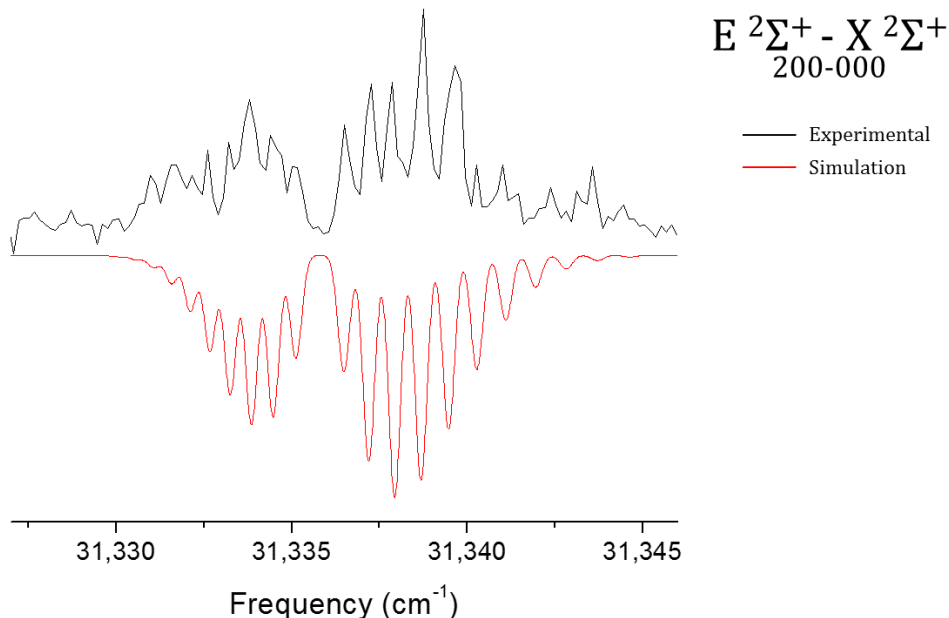


Figure 4.7: Rotationally resolved and simulated spectra of the 200-000 band of the  $\tilde{E} \ ^2\Sigma^+ - \tilde{X} \ ^2\Sigma^+$  transition of CaOH. The simulated spectrum was generated using PGOPHER. The rotational temperature of the simulation is 9K.

The inclusion of a third vibronic band was necessary in order to determine the vibrational constant,  $\omega_e$ , and anharmonicity constant,  $\omega_e\chi_e$ , for the Ca-OH stretching mode. These vibrational constants were determined by plotting the term energies of the vibronic states,  $G(\nu)$ , versus  $\nu + \frac{1}{2}$  and fitting the resulting values to a second order polynomial expression, where the relationship between  $\omega_e$ ,  $\omega_e\chi_e$ , and  $G(\nu)$  is given by the energy level expression[299]

$$G(\nu) = \omega_e \left( \nu + \frac{1}{2} \right) - \omega_e\chi_e \left( \nu + \frac{1}{2} \right)^2 \quad (4.2)$$

where  $\nu$  is equal to the vibrational levels of the  $\tilde{E} \ ^2\Sigma^+$  state observed experimentally ( $\nu = 0,1,2$ ). The vibrational constants obtained from this fit, and the rotational constants from the PGOPHER simulations, can be seen in Tables 4.5 and 4.6 below.

Table 4.5: Molecular constants for the  $\tilde{E} \ ^2\Sigma^+ - \tilde{X} \ ^2\Sigma^+$  vibronic bands of CaOH<sup>a</sup>

$\nu'$	$T_{\nu',0}$	$B_{\nu'}$	$D_{\nu'}$	$\gamma$
0	29,880.02(3)	0.3639(1)	$1.2 \times 10^{-6}(1)$	$2.76 \times 10^{-2}(1)$
1	30,618.53(1)	0.3554(2)	$-3.9 \times 10^{-6}(7)^b$	
2	31,335.79(2)	0.3456(8)		

All values are in units of  $\text{cm}^{-1}$ . The numbers in parentheses indicate the  $1\sigma$  errors.

<sup>a</sup>Ground state ( $\tilde{X} \ ^2\Sigma^+$ ) rotational constants were fixed to values reported by Ziurys *et al.*[276]

<sup>b</sup> Negative value for centrifugal distortion constant is indicative of a perturbation.

Table 4.6: Molecular constants for the  $\tilde{E} \ ^2\Sigma^+$  state of CaOH, compared with previous theoretical studies

Term	Experimental	Theoretical	
	This work <sup>a</sup>	MR-CDI <sup>b</sup>	bII <sup>c</sup>
$T_e \ (\text{cm}^{-1})$		30,165	31,302
$T_{0,0} \ (\text{cm}^{-1})$	29,880.02(3)		
$\omega_e \ (\text{cm}^{-1})$	759.76(7)		713.2
$\omega_e\chi_e \ (\text{cm}^{-1})$	10.63(2)		

<sup>a</sup>The numbers in parentheses indicate the  $1\sigma$  errors.

<sup>b</sup>Multireference double excitations configuration interaction. Reference [283].

<sup>c</sup>Effective valence shell Hamiltonian, basis set II with 12 valence orbitals. Reference [298].

The most intense feature in Figure 4.4 appears at  $\sim 30,213 \text{ cm}^{-1}$  consistent with the previously reported origin band of the  $\tilde{F} \ ^2\Pi - \tilde{X} \ ^2\Sigma^+$  transition by Pereira and Levy[269]. It is clear from this spectrum that the rotational structure of this band is unresolved, complicating spectroscopic assignments. One noteworthy feature of this band is the absence of a pronounced Q branch, previously reported by Pereira and Levy[269]. A second scan of this feature was performed in the hopes of revealing the underlying structural characteristics of this excited electronic state of CaOH. This scan can be seen in Figure 4.8.

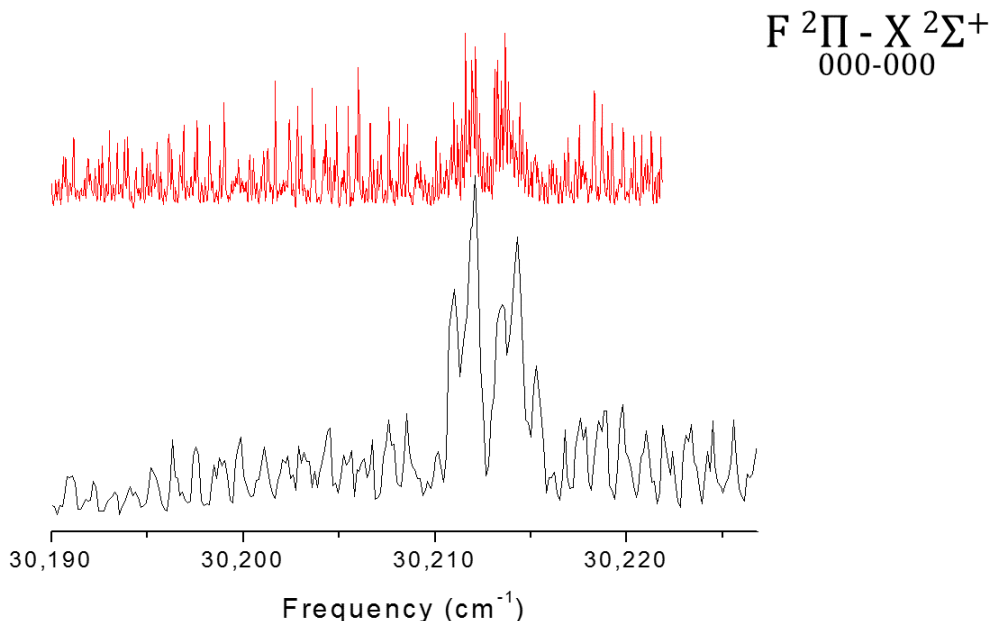


Figure 4.8: Experimental spectra for the 000-000 band of the  $\tilde{F}^2\Pi - \tilde{X}^2\Sigma^+$  transition of CaOH. The lower trace (black) is the low resolution trace from Figure 4.4, while the upper trace (red) is from a second scan of the same region with increased averaging.

While the signal-to-noise ratio in this spectrum is quite poor compared to the original spectrum, no obvious features associated with a Q-branch in the origin band of the  $\tilde{F}^2\Pi - \tilde{X}^2\Sigma^+$  transition are present. The features present on each side of the origin band resemble spectral features, but are likely noise. An accurate assignment cannot be made from these spectra.

#### 4.2.4 Discussion

The spectroscopic constants derived from the experimental observations compare favorably with previous theoretical results listed in Table 4.6. The  $\tilde{E}^2\Sigma^+$  state is predicted to be the most strongly bound electronic state of CaOH. The vibrational stretching and anharmonicity constants of the Ca-OH stretch are reported here for the first time. This vibrational stretching frequency,  $759.76(7) \text{ cm}^{-1}$ , is the largest known value for CaOH. Theoretical predictions indicate that while the Ca-O bond shortens (higher stretching frequency), the O-H bond lengthens (lower stretching frequency)

upon excitation[283, 298]. It is reasonable to assume that the calculations accurately predict this geometry change based on the strong agreement with the results for the Ca-O bond. However no experimental data for the O-H bond length in the  $\tilde{E}^2\Sigma^+$  state are reported in the literature to confirm these predictions. While the  $\tilde{E}^2\Sigma^+$  state does exhibit increased covalent bonding characteristics, the bonding in this electronic state is still largely ionic in nature.

A reasonable value for the equilibrium rotational constant,  $B_e$ , was determined from the observed vibronic bands. Using the relationship between rotational constant and bond length[277], the Ca-OH bond length was estimated for the  $\tilde{D}^2\Sigma^+$  state by Pereira and Levy[269] by fixing the CaO-H bond length to that for the  $\tilde{A}^2\Pi$  state[300]. This is not advisable for the  $\tilde{E}^2\Sigma^+$  state as this is the only electronic state that is predicted to have a significant change in the OH group upon excitation[298].

The splitting observed in higher J lines of the 000-000 band of the  $\tilde{E}^2\Sigma^+ - \tilde{X}^2\Sigma^+$  transition originates from the large spin-rotation constant ( $\gamma$ ) in the  $\tilde{E}^2\Sigma^+$  state. The spin-rotation interaction in this state is best described in terms of Hund's coupling case b[301, 302]. This molecule contains one unpaired electron ( $S = 1/2$ ). The spin angular momentum,  $\hat{\mathbf{S}}$ , is not coupled to the internuclear axis and the spin-orbit interaction is weak or non-existent ( $\Lambda = 0$ ). The rotational angular momentum is then defined by the quantum number,  $\hat{\mathbf{N}}$ , which is exclusive of spin. In this case the spin acts as a slight perturbation to the molecular rotation, where this interaction is best represented by the Hamiltonian

$$\hat{\mathbf{H}}_{\text{sr}} = \gamma \hat{\mathbf{N}} \cdot \hat{\mathbf{S}} \quad (4.3)$$

where each rotational transition is split in energy by the expressions[301, 303]

$$F_1(e) = B_\nu N(N + 1) + \frac{1}{2} \gamma_\nu N \quad (4.4)$$

$$F_2(f) = B_\nu N(N + 1) - \frac{1}{2}\gamma_\nu (N + 1). \quad (4.5)$$

The  $e$  levels correspond to  $J = N + \frac{1}{2}$  states, while the  $f$  state correlates to  $J = N - \frac{1}{2}$  states. The large value for  $\gamma$  can be attributed to a perturbation in the  ${}^2\Sigma$  state arising from interactions with a near lying  ${}^2\Pi$  state[301, 304]. The  $\tilde{F}$   ${}^2\Pi$  and  $\tilde{G}$   ${}^2\Pi$  states are believed to mix strongly with the  $\tilde{E}$   ${}^2\Sigma^+$  based on theoretical studies by Theodorakopoulos *et al.*[283] and Taylor *et al.*[298]. This interaction has been observed for the  $\tilde{B}$   ${}^2\Sigma^+$  state which interacts with the nearby  $\tilde{A}$   ${}^2\Pi$  state[290]. The value for  $\gamma$  reported here,  $2.76 \times 10^{-2} \text{ cm}^{-1}$ , is on the same order as that previously reported for the  $\tilde{B}$   ${}^2\Sigma^+$  state,  $-4.36 \times 10^{-2} \text{ cm}^{-1}$ , which lends credence to this conclusion.

No rotational structure for the origin band of the  $\tilde{F}$  state was observed, which complicates spectral assignment. It can be seen from Figure 4.8 that the presence of a dominant Q branch is difficult to identify in these spectra. However the presence or absence of a strong Q branch alone is insufficient to comment on the nature of bonding (ionic vs. covalent) in these systems, as was previously noted in previous studies by our group on BeOH[147, 287]. Theoretical calculations of the excited electronic states of CaOH by Theodorakopoulos *et al.*[283] and Taylor *et al.*[298] each indicate that for the  $\tilde{F}$  state, the geometry is linear at the global minimum with closely lying non-linear local minima (with a barrier to linearity of  $\sim 100 \text{ cm}^{-1}$ ). It is apparent that the spectral assignment of this band system is highly complex in nature due to the strong mixing between the  $\tilde{E}$ ,  $\tilde{F}$ , and  $\tilde{G}$  states. Preliminary measurements cannot confirm the theoretical prediction of a linear geometry in the  $\tilde{F}$  state. Additional measurements are necessary in order to further characterize this convoluted spectral region.

## 4.3 Dicalcium Oxide (CaOCa)

### 4.3.1 Introduction

The only reported experimental studies of CaOCa are those by Andrews and co-workers in the late 1970's. In those studies calcium metal was reacted with ozone ( $^{16}\text{O}_3$ ) and oxygen ( $^{16}\text{O}_2$ ) in a solid nitrogen matrix at 15K[305, 306]. The reactions of isotopically substituted  $^{44}\text{Ca}$  with  $^{16}\text{O}_3$ , and  $^{40}\text{Ca}$  with  $^{18}\text{O}_3$  were also performed[306]. The infrared spectra of the reaction products were recorded in the 400-800  $\text{cm}^{-1}$  region. Two vibrational bands were assigned as belonging to the symmetric species CaOCa. Analysis of these bands indicated a bent structure for the ground electronic state, with a nearly  $120^\circ$  bond angle.

A recent *ab initio* study by Bunker and co-workers[307] contradicts this assignment. This study found that the ground electronic state has a linear symmetrical equilibrium structure (CaOCa) with  $^1\Sigma_g^+$  symmetry and a Ca-O bond length of 1.995 Å. The first excited electronic state is a low lying triplet state, ( $\tilde{a} \ ^1\Sigma_u^+$ ), also possessing a linear symmetrical equilibrium structure with a Ca-O equilibrium bond length of 1.998 Å. The singlet-triplet splitting,  $T_e(\tilde{a})$ , is 386  $\text{cm}^{-1}$ . Bunker and co-workers report similar results for all alkaline earth hypermetallic oxides:  $\text{Be}_2\text{O}$ [308],  $\text{Mg}_2\text{O}$ [309],  $\text{Sr}_2\text{O}$ [310],  $\text{Ba}_2\text{O}$ [311], and  $\text{Ra}_2\text{O}$ [311].

The electronic structure of the lightest hypermetallic alkaline earth oxide, BeOBe, has been previously investigated by our group[146]. BeOBe was produced using laser ablation and supersonically expanded into a vacuum chamber. The observed vibronic bands were characterized using LIF, REMPI, and stimulated emission pumping (SEP). Electronic structure calculations were used to facilitate the analysis of the spectra. The results showed that the ground state is linear and symmetric with  $^1\Sigma_g^+$  symmetry. The electronic structure calculations support this conclusion. A theoretical study by Boldyrev and Simons[312] also predicted that for BeOBe the geometry

of the ground electronic state is linear in nature, with strong multireference character. The vibronic bands of BeOBe observed by Merrit *et al.*[146] originated from excitation of the  $X^1\Sigma_g^+$  state to a linear or near linear excited electronic state. The vibronic progressions were assigned to the symmetric and anti-symmetric stretching vibrations in the excited electronic state. The Be-O bonds weakened upon electronic excitation which is indicative of electron promotion to a nonbonding or antibonding orbital. Since BeOBe and CaOCa are isovalent, similar spectral and structural results were expected.

Prior to the work reported here, there were no reported gas phase observations of the electronic transitions of CaOCa. This section details the first reported electronic spectra of hypermetallic CaOCa. Jet-cooled CaOCa was produced by laser ablation of a Ca rod and supersonically expanded into a vacuum chamber. Ablation products were detected using LIF. Vibronic bands were observed in the 14,500 - 16,000  $\text{cm}^{-1}$  region. The presence of CaOCa was confirmed using simulations performed with the PGOPHER spectral fitting program. Electronic structure calculations, used to aid spectral assignments, were performed in MOLPRO 2012[313] using the multireference configuration method (MRCISD) with state-averaged full-valence complete active space self-consistent field wavefunctions (SA-FV-CASSCF).

### 4.3.2 Methods

The experimental setup described in Section 4.1.2 was used to record the LIF spectrum of CaOCa, but with several important adjustments. This setup can be seen in Figure 4.9 below.

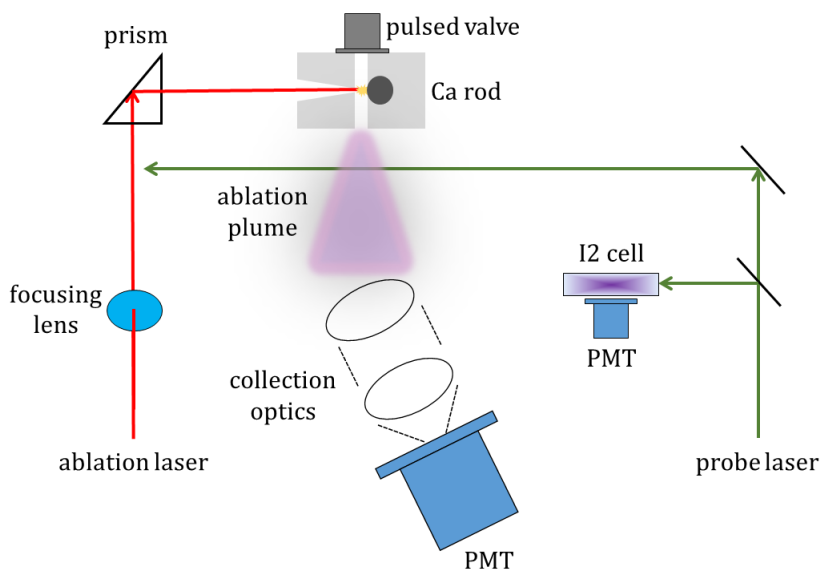


Figure 4.9: Apparatus used to record the LIF spectrum of CaOCa. The collection optics and PMT are shown at an angle to indicate that this assembly is located perpendicular to the crossing of the ablation laser and the freejet expansion.

In order to minimize inconsistencies with source conditions, a Smalley type laser ablation source[314, 315] replaced the one described in Section 4.1.2. This provided for a more stable set of experimental conditions on a day to day basis. The ideal conditions for producing CaOCa in this source were attained by varying the backing pressure of He from  $\sim 8$ -10 atm, along with smaller percentage of N<sub>2</sub>O (0.1%). The first set of experiments utilized the same pulsed valve (Parker-Hannifin General Valve Series 99) to produce gas pulses with a pulse duration of  $\sim 550 \mu\text{s}$ . This valve was damaged during operation and replaced with a similar pulsed valve, Parker-Hannifin General Valve Series 9. No change in performance between the pulsed valves was noted.

The tunable light used for these experiments was in the red region of the visible spectrum, and as such the BBO doubling crystal and short-pass filter were removed. Optimized delays for observing CaOCa were such that the ablation laser was fired  $\sim 600 \mu\text{s}$  (i.e. due to mechanical delay in the pulsed valve response) after the opening of the pulsed valve, and the probe laser was fired between 24 and 31  $\mu\text{s}$  (depending

on source conditions) after the ablation laser. The boxcar integrators were each set to average 100 shots from the laser, to increase the signal-to-noise ratio for weak vibronic bands. The laser was averaged at each wavelength step for 15 s to account for the increased number of laser pulses.

### 4.3.3 Experimental Results

Initial attempts to observe CaOCa were prompted by an experimental study performed by two members of the Heaven lab, Josh Bartlett and Robert VanGundy. While performing spectroscopic studies via laser ablation on a calcium rod, mass spectra from a time-of-flight mass spectrometer (TOF) indicated a large signal from a species corresponding to CaOCa. A LIF survey scan revealed two unresolved features at  $\sim 32,400 \text{ cm}^{-1}$ , as seen in Appendix C.1. This pattern is indicative of a molecular species with a smaller rotational constant than CaO, which is also produced by laser ablation of a calcium rod. These features are absent in Figure 4.2. High level *ab initio* calculations performed by our collaborator, Dr. Wafaa Fawzy (Murray State University), provided us with predictions for the electronic band origins of transitions from the ground to excited states of CaOCa. The results from these theoretical studies are provided in Section 4.3.4.

The calculations indicated the presence of an electronic transition ( $A^1\Sigma_u^+ - X^1\Sigma_g^+$ ) in the red region of the visible spectrum. An initial LIF survey scan (see Figure 4.10) revealed the presence of a strong band of CaO, the 5-0 band of the  $A^1\Sigma^+ - X^1\Sigma^+$  transition[255], along with several weaker unresolved bands similar to those seen in Appendix C.1. Experimental conditions (i.e. ablation laser intensity and focus onto the rod, timings between lasers and the pulsed valve, etc.) were adjusted in order to optimize the intensity of these weaker features. After optimization, additional survey scans revealed the presence of numerous blue shaded vibronic bands shown in Figure 4.11.

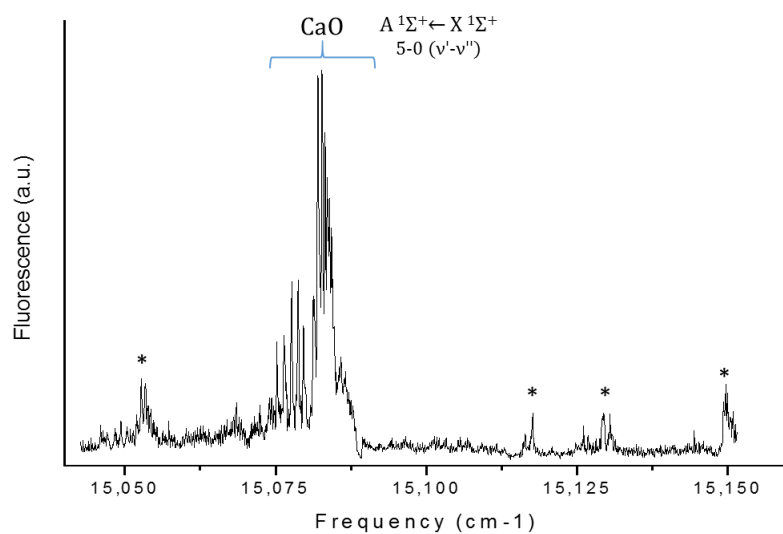


Figure 4.10: Initial LIF Survey for CaOCa. The 5-0 band of the  $A\ ^1\Sigma^+ - X\ ^1\Sigma^+$  transition predominates the observed spectrum, along with several smaller bands potentially arising from CaOCa, labeled as \*.

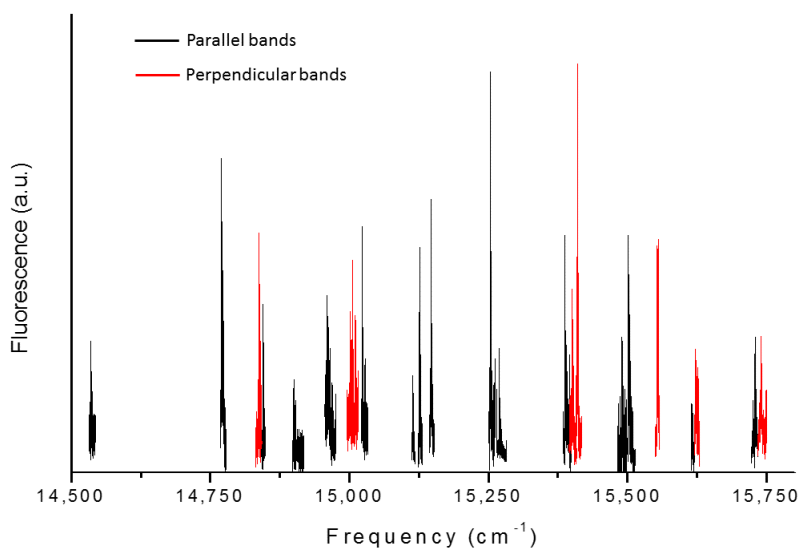


Figure 4.11: Vibronic bands observed from laser ablation of calcium in the red region of the visible spectrum. Parallel bands (P and R branch structure) are shown in black, while bands with perpendicular type transitions (P, Q, and R branches) are in red.

Two types of band systems were observed. The first, which are defined as parallel, contain well defined P and R branch transitions only. The second, which are defined as perpendicular, consist of transitions with undetermined rotational character. Each band was first observed without the use of the intracavity etalon (resolution  $\sim 0.2 \text{ cm}^{-1}$ ) in order to determine accurate band positions. Scans performed using the intracavity etalon (resolution  $\sim .05 \text{ cm}^{-1}$ ) were then performed in order to obtain rotationally resolved vibronic spectra. The remainder of this section will focus solely on the results and analysis of the parallel bands seen in Figure 4.11.

The PGOPHER program[226] was utilized to simulate the rotational structure for the vibronic bands. The spectra were rotationally cold, typically  $\sim 6\text{K}$  as determined based on simulations of the 5-0 band of the A  $^1\Sigma^+$  - X  $^1\Sigma^+$  transition of CaO. Each simulation was set as a  $^1\Sigma_u^+$  -  $^1\Sigma_g^+$  transition, with  $D_{\infty h}$  as the point group. Since the ground electronic state is assumed to have a linear geometry, and  $I = 0$  for  $^{40}\text{Ca}$ , only even J exist. For the first cycle of fitting, the molecular constants from the electronic structure calculations were used as a starting point to determine line assignments for the ground ( $B_e'' = 0.05096 \text{ cm}^{-1}$ ) and excited ( $B_e' = 0.05275 \text{ cm}^{-1}$ ) electronic states. The rotational constants and vibronic origin were then each allowed to float. Each parallel vibronic band was fit individually and molecular constants were extracted from each fit. For the second cycle, a group fit to all parallel vibronic bands was performed using an identical ground state rotational constant. Initially, it was assumed that all vibronic bands originated from the X,  $\nu''=0$  level. However, the results from each cycle of fitting yielded unusual results. Several of the bands (in the group fit) were difficult to simulate using PGOPHER. This is easily explained if some of the bands originate from  $\nu'' > 0$ . Furthermore, no definitive pattern was observed between the vibrational spacing of the bands. Finally, the rotational constants extracted for the ground state (individual fit) varied by as much as  $0.004 \text{ cm}^{-1}$ . This level of discrepancy indicated incorrect assignments of the bands observed.

Looking to the literature it was obvious that several of the observed parallel bands in Figure 4.11 belong to the  $A\ ^1\Sigma_u^+ - X\ ^1\Sigma_g^+$  transition of  $\text{Ca}_2$ , first reported by Bondybey and English[316]. Removing those bands from the analysis, only six vibronic bands remained, four of which were rotationally resolved. The PGOPHER fit of one of these bands can be seen in Figure 4.12.

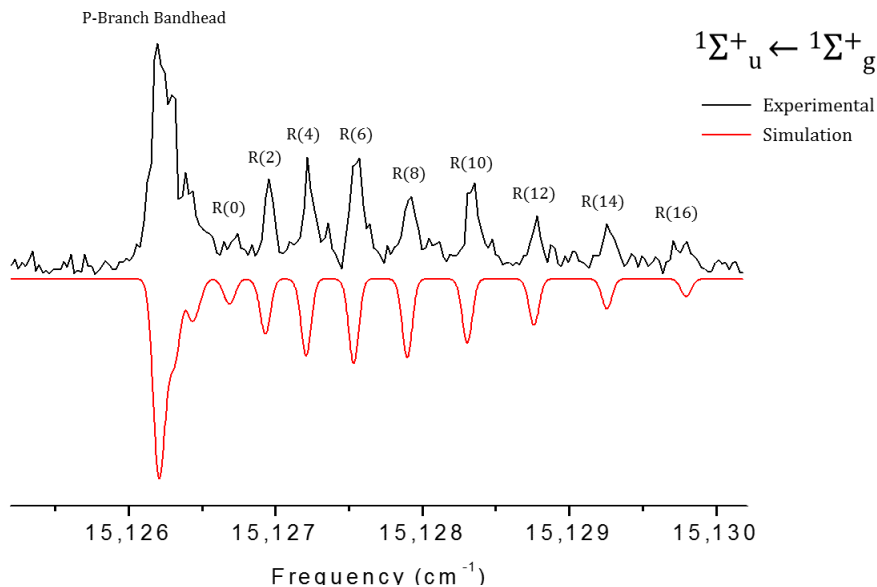


Figure 4.12: High resolution LIF spectrum of one of the rotationally resolved vibronic bands of  $\text{CaOCa}$ . Simulation of the rotational structure was performed using the PGOPHER program. A rotational temperature of 6 K was used in this simulation.

The remaining bands were each fit individually, similarly to the first cycle of fitting. The molecular constants from these fits are listed in Table 4.7.

Again, it is likely that several of the observed vibronic bands originate from excited vibrational bands ( $\nu' > 0$ ) in the  $X\ ^1\Sigma^+$  state. This is especially likely considering there are two vibronic bands separated by only  $\sim 13\text{ cm}^{-1}$ . It is difficult to obtain an accurate PGOPHER simulation (and subsequently determine molecular constants) for several of the observed vibronic bands due to the low signal-to-noise ratio in these spectra. Additional experimental data is needed in order to make definitive vibronic state assignments for the bands reported in Table 4.7.

Table 4.7: Fitted molecular constants of CaOCa derived from individual fits of vibronic bands using PGOPHER

$T'_\nu$	$B_{\nu''}$	$B_{\nu'}$
14,535 <sup>a</sup>	N/A	N/A
14,844.61(1)	0.0448(5)	0.0513(5)
15,113.87(1)	0.0539(5)	0.0586(4)
15,126.63(1)	0.0463(4)	0.0514(4)
15,253.63(1)	0.0463(6)	0.0535(6)
15,490 <sup>a</sup>	N/A	N/A

All values are in units of  $\text{cm}^{-1}$ . The numbers in parentheses indicate the  $1\sigma$  errors.

<sup>a</sup> Molecular constants undetermined due to poor signal-to-noise ratio in experimental spectrum. Band position approximated by visual inspection.

#### 4.3.4 Theoretical Calculations

As noted previously, the calculations presented here were performed by our collaborator, Dr. Wafa Fawzy. Theoretical calculations of CaOCa were performed using the MOLPRO 2012 suite of programs[313] at the Cherry L. Emerson Center for Scientific Computation at Emory University. The potential energy surface (PES) of the ground electronic state and eleven excited singlet electronic states were calculated, along with the nine triplet excited electronic states. Linear ( $D_{\infty h}$ ) and non-linear ( $C_{2v}$ ) configurations were considered. Note that MOLPRO is limited to Abelian point group symmetries only.  $D_{\infty h}$  is therefore approximated for these calculations as  $D_{2h}$ . The excited electronic states (and symmetries) of the linear structure are as follows: A  $\Sigma_u^+$  ( $B_{1u}$ ), B  $\Sigma_g^+$  ( $A_g$ ), C  $\Pi_g$  ( $B_{2g} + B_{3g}$ ), D  $\Pi_u$  ( $B_{2u} + B_{3u}$ ), E  $\Pi_g$  ( $B_{2g} + B_{3g}$ ), and F  $\Pi_u$  ( $B_{2u} + B_{3u}$ ). The symmetries of the non-linear geometry ( $C_{2v}$  symmetry) are  $B_2$ ,  $A_1$ ,  $A_2 + B_2$ ,  $A_1 + B_1$ ,  $A_2 + B_2$ , and  $A_1 + B_1$ .

These PES's were first calculated using the complete active space self-consistent field (CASSCF) method[317, 318], followed by the multi-reference configuration interaction (MRCI) method[319, 320, 321]. The active space used, CAS(10,12), consisted

of all configurations of ten valence electrons ( $2s^22p^4$  on O /  $4s^2$  on each Ca) in twelve molecular orbitals. These MO's (in  $C_{2v}$  symmetry) include five of  $A_1$  symmetry, two of  $B_1$  symmetry, four of  $B_2$  symmetry, and one of  $A_2$  symmetry. All valence electrons were correlated, and contributions to higher excitations and relativistic effects were taken into account using the Davidson correction (Q)[322] and the Douglas-Kroll-Hess (DKH) Hamiltonian[323, 324, 325], respectively. The basis set used for all three atoms was the Douglas-Kroll correlation consistent polarized core valence quadruple-zeta basis set (cc-pwCVQZ-DK) developed by Koput and Peterson[284]. This particular basis set is necessary to account for the core-valence correlation of the 3s and 3p calcium orbitals. The core electrons of the Ca and O atoms were optimized but were not included in the correlation. The full level of theory is abbreviated as SA-FV-CASSCF (10, 12)-MRCISD-Q/cc-pwCVQZ-DK, where SA denotes state averaged and FV denotes full valence.

The transition of interest, from the ground electronic state to the first excited singlet state, was calculated to originate at  $14,801\text{ cm}^{-1}$ . The results of the three dimensional PES showed the minimum energy structure is linear in the  $X\ ^1\Sigma_g^+$  ground state ( $D_{\infty h}$  point group) while it is bent ( $C_{2v}$  point group) in the first excited electronic state,  $^1B_2$ , as seen in Figure 4.13. The barrier to linearity lies  $3,300\text{ cm}^{-1}$  above the global minimum.

Using the calculated *ab initio* PES of the ground and first excited states, the Discrete Variable Representation (DVR) quantum mechanical method (available in the DVR3D software package[326]) was used to calculate the vibrational energy levels in the corresponding states ( $X\ ^1\Sigma_u^+$  and  $A\ ^1B_2$ ). Accurate fits of the ground state were obtained, with a standard deviation of  $3.99\text{ cm}^{-1}$ . However, fitting the  $^1B_2$  state was complicated due to errors with the excited state PES. Efforts to correct this issue are currently ongoing.

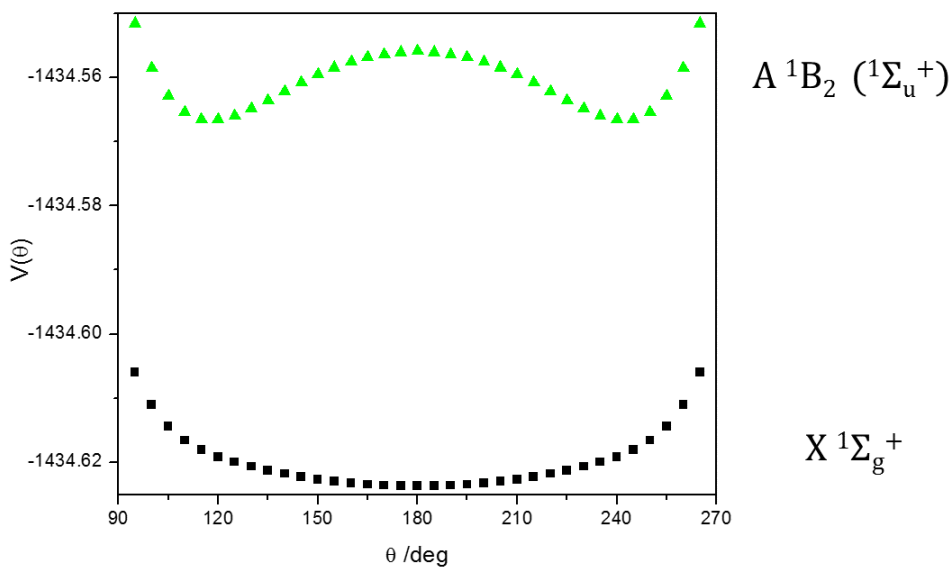


Figure 4.13: PES for the ground and first excited electronic state of CaOCa. The excited state symmetry is  $^1B_2$  (bent geometry) at the global minimum, and  $^1\Sigma_u^+$  (linear geometry) at higher energy.

### 4.3.5 Discussion

The presence of numerous vibronic bands of  $\text{Ca}_2$  complicated the initial assignment of the CaOCa bands present within the survey scan in Figure 4.11. Naturally the presence of two molecular species explains the difficulty met with assigning vibrational progressions and the numerous differences in ground state rotational constants between vibronic bands. This was unexpected and obscured by the fact that the rotational constants for the ground states of  $\text{Ca}_2$  and CaOCa are close,  $B \sim 0.04 \text{ cm}^{-1}$ .

Despite the fact that a majority of the vibronic bands observed belonged to a separate molecular species, it is clear that the remaining bands do indeed belong to the symmetric species CaOCa. The spacing between rotational lines excludes the possibility of another calcium species, as the rotational constant of CaO ( $\sim 0.3 \text{ cm}^{-1}$ ) is much larger than that CaOCa ( $\sim 0.04 \text{ cm}^{-1}$ ). Larger  $\text{Ca}_x\text{O}_y$  clusters would have

much smaller rotational constants than those observed experimentally, precluding the possibility of achieving sufficient rotational resolution for analysis. The only other likely molecular candidate would be a hot band of the A  $^1\Sigma_u^+$  - X  $^1\Sigma_g^+$  transition of Ca<sub>2</sub>. This can be discounted for several reasons. Bondybey and English[316] observed hot bands from  $\nu'' = 1 \rightarrow \nu' = 1-6$  (and 9) in their study of the A  $^1\Sigma_u^+$  - X  $^1\Sigma_g^+$  transition. The only hot band observed in this study was  $\nu'' = 1 \rightarrow \nu' = 4$ , most likely due to unfavorable expansion conditions for this individual scan. Rotational constants for the higher vibrational levels of the X  $^1\Sigma_g^+$  state of Ca<sub>2</sub> were reported by Balfour and Whitlock[327], and also by Vidal[328]. The observed vibronic bands in Table 4.7 were simulated using molecular constants from the  $\nu'' = 2$  vibrational level of the X  $^1\Sigma_g^+$  state of Ca<sub>2</sub> in PGOPHER to further verify that these bands do not belong to hot bands of Ca<sub>2</sub>. Finally, the simulated spectrum shown in Figure 4.12 demonstrates the fact the observed species is centrosymmetric in its ground electronic state, as only even rotational levels are observed (<sup>40</sup>Ca, I = 0). This lends credence to our assignment of the molecular species as CaOCa with a linear ground state (X,  $^1\Sigma_g^+$  symmetry).

Assignment of the excited electronic state was assisted through the use of spectral simulations performed using PGOPHER, as noted in Section 4.3.3. The simulation seen in Figure 4.12 is a representative fit of the four rotationally resolved vibronic bands observed experimentally. The results from these simulations were derived with the parameters adjusted to correspond with a linear excited state with  $^1\Sigma_u^+$  symmetry. The lack of a strong Q branch is further proof of this assignment. However, the results from the *ab initio* studies (see Figure 4.13) show that the excited geometry is bent at its lowest energy configuration. This would suggest that the vibronic bands reported here belong to a highly excited vibrational state of CaOCa, near or above the barrier to linearity located approximately  $\sim 3,300 \text{ cm}^{-1}$  above the global minimum.

The molecular constants presented in Table 4.7 show that the electronic excitation

of CaOCa resulted in the shortening of the Ca-O bonds (i.e. the rotational constant increased upon excitation). The simulated spectra and electronic structure calculations suggest a strongly allowed transition, with singlet multiplicity in the ground and first excited electronic states. The transitions were indeed strongly allowed, as demonstrated by the short fluorescence lifetime of the upper state ( $\sim 10\text{-}20$  ns). Further analysis of these bands is hindered by the lack of additional experimental information coupled with the need for accurate predictions of the vibrational states from the electronic structure calculations. Additional experimental studies of CaOCa using LIF and REMPI techniques will be performed in the near future with the help of Robert VanGundy in order to definitively assign the vibronic bands reported here.

As predicted by Bunker and co-workers[307], the equilibrium geometry in the ground electronic state is linear,  $^1\Sigma_g^+$  symmetry. This is due to the ionic bonding character in this state, where separate electron spins are located on each calcium ion ( $\text{Ca}^+\text{O}^{-2}\text{Ca}^+$ ). In contrast, the bent geometry at the global minimum of the excited electronic state suggests a strong covalent character,  $^1B_2$  symmetry. Future experimental studies of the perpendicular bands shown in Figure 4.11, at higher spectral resolution, will be informative in characterizing the bent geometry of the  $^1B_2$  state. The difficulty in analyzing these bands is due to the change in geometry (linear to bent) in the  $^1\Sigma_u^+/^1B_2$  state.

## 4.4 Conclusion

Jet-cooled spectra for electronic bands of CaO and CaOH in the UV region, and for CaOCa in the visible region, have been recorded using a laser ablation source coupled with LIF for detection. The observed vibronic bands of CaO extend the current range of levels reported in the literature for the C  $^1\Sigma^+$  and F  $^1\Pi$  states. This is the first reported observation of the F  $^1\Pi$  - X  $^1\Sigma^+$  transition, which is a formally

allowed one-electron excitation using the integer charge model of Baldwin *et al.*[256]. Also present within the observed spectra are three vibronic levels attributed to a new  $0^+$  state. One of these vibronic bands, n, interacts strongly with the C  $^1\Sigma^+$ ,  $\nu' = 7$  level. These bands have similar characteristics to the previously reported C'  $^1\Sigma^+$  state, and could be attributed to higher vibrational levels of this state. However several other bands, namely  $g^3\Pi(0^+)$  and  $e^3\Sigma^-(0^+)$ , are also predicted to occur in this energy range[270]. Additional work is needed in order to definitively assign these vibronic bands.

For CaOH, rotationally resolved vibronic bands of the  $\tilde{E}^2\Sigma^+ \leftarrow \tilde{X}^2\Sigma^+$  transition are reported for the first time. The bonding in the  $\tilde{E}^2\Sigma^+$  state is largely ionic in nature, consistent with previous theoretical studies[283, 298]. Additionally, the  $\tilde{E}^2\Sigma^+$  state is predicted to be strongly bound. However only molecular constants from the Ca-OH stretching mode are observed experimentally, and information on the CaO-H stretching mode and/or bending mode is necessary to make a direct comparison with the theoretical predictions. Spin-rotation splitting was observed in the high J lines of the  $\tilde{E}^2\Sigma^+$  origin band, which could arise due to interactions with the near lying  $\tilde{F}$  and  $\tilde{G}$  states. Further analysis is needed to examine its origin. The  $\tilde{F}$  state was observed, but was not rotationally resolved, precluding the possibility of assigning the excited state equilibrium geometry which has conflicting assignments in the literature (i.e. linear vs. bent)[269, 283, 298]. Future experiments of CaOH will focus on improving molecular constants of the  $\tilde{E}^2\Sigma^+$ , 200 band, and on the assignment of the origin band (and vibronic progressions) of the  $\tilde{F}$  state.

Finally, CaOCa has been observed spectroscopically in the gas phase for the first time. These investigations were aided by electronic structure calculations at the SA-FV-CASSCF (10,12)- MRCISD-Q/cc-pwCVQZ-DK level of theory. Multiple vibronic bands were observed in the 14,500 - 16,000  $\text{cm}^{-1}$  region, wherein the presence of  $\text{Ca}_2$  created during ablation complicated spectral assignment. PGOPHER simulations

were used to confirm the presence of CaOCa in the observed spectra. Only even rotational levels were observed, consistent with a centrosymmetric species with a linear geometry in the ground electronic state ( $^1\Sigma_g^+$ ), as predicted by the electronic structure calculations. Furthermore, the observed bands do not match with previously reported bands of Ca<sub>2</sub>[316], supporting the CaOCa assignment for the remaining features. The electronic structure calculations predict that the equilibrium geometry of the excited electronic state is bent, with a 3,300 cm<sup>-1</sup> barrier to linearity. The observed bands (simulated assuming a linear geometry) must therefore be highly vibrationally excited. Further studies are needed to make definitive vibrational state assignments for the vibronic bands presented here.

# Chapter 5

## Concluding Remarks

The spectroscopic characterization of the excited electronic states of several molecular species relevant to PAH formation and the study of ultracold molecules are outlined within this dissertation. Cavity ringdown and laser induced fluorescence spectroscopy were utilized as detection methods in the study of PAH intermediates (phenoxy and phenylperoxy radicals) and group IIA metallic oxides (CaO, CaOH, and CaOCa), respectively. The use of a supersonic expansion was utilized in these experiments in order to alleviate spectral congestion and aid in the analysis of structural characteristics for each species.

Vibronic bands corresponding to the  $\tilde{B}^2A_2 \leftarrow \tilde{X}^2B_1$  transition of the phenoxy radical and the  $\tilde{B}^2A'' \leftarrow \tilde{X}^2A''$  transition of the phenylperoxy radical were assigned through the assistance of electronic structure calculations performed using Gaussian 09. Rotational structure was unresolved due to significant linewidth broadening as a result of either nonradiative decay or internal decomposition pathways present in each radical. The  $\tilde{B}^2A_2 \leftarrow \tilde{X}^2B_1$  transition of the phenoxy radical is best described as  $\pi - \pi^0$ , while the  $\tilde{B}^2A'' \leftarrow \tilde{X}^2A''$  transition of the phenylperoxy radical is  $\pi - \pi^*$ . The results presented here can provide an accurate benchmark for future *ab initio* studies of combustion intermediates. Additionally, it would be of interest to continue

these studies for other intermediate species involved in combustion/PAH formation, such as the naphthyl[329, 330] or 2-oxepinoxy radical[235, 331], where experimental data on their electronic structure and bonding characteristics are lacking.

Following the work on PAH intermediates, the spectroscopic investigations of the neutral species CaO, CaOH, and CaOCa are presented. Rotationally resolved vibronic bands for each species were identified. Molecular constants for several previously unobserved vibrational levels of the C  $^1\Sigma^+$  and F  $^1\Pi$  electronic states of CaO were determined, along with three vibronic bands of a currently unassigned excited electronic state. Several assignments for these bands are considered, including the C  $^1\Sigma^+$ ,  $g^3\Pi$ , and  $e^3\Sigma^-$  states; however further experimental studies are needed to make a definitive assignment. LIF spectra of the  $\nu = 0, 1,$  and  $2$  vibrational bands (Ca-OH stretching mode) of the  $\tilde{E} \ ^2\Sigma^+$  state of CaOH constitute the only available experimental information on the ionic bonding character in this excited electronic state. Evidence of perturbative effects with nearby electronic states is observed (i.e.  $\gamma$  in origin band), but cannot be confirmed without additional information on higher lying electronic states. Future experiments will focus on ascertaining whether bonding in the nearby  $\tilde{F}$  state is ionic in nature (similar to the other electronic states of CaOH) or if it represents the first excited state electronic state of CaOH that is largely covalent in nature. While several vibronic bands for hypermetallic CaOCa are presented, little information on the electronic states of this molecule is available as no definitive vibrational state assignments can be made with the present data. Additional studies of CaOCa are currently ongoing, focusing on the characterization and assignment of these vibronic bands using a combination of LIF and REMPI spectroscopy. Results from these studies will be used to benchmark future calculations, and to provide guidance on future experimental work of CaOCa and other group IIA hypermetallic oxides, needed to further elucidate the nature of bonding in these species. Detailed information on the internal states of neutral CaO, CaOH, and CaOCa is also

paramount to future studies of their cationic forms, as ZEKE spectroscopy of cations requires accurate state information for two photon excitation.

# Appendix A

## Phenoxy

Table A.1: List of bond lengths ( $\text{\AA}$ ) and bond angles ( $^\circ$ ) for the phenoxy radical calculated in the  $\tilde{X} \ ^2B_1$  and  $\tilde{B} \ ^2A_2$  electronic states. Unlisted bond lengths and angles are identical to their mirrored counterparts.

Level	UB3LYP	UB3LYP	TD-DFT	TD-DFT
Basis Set	cc-pVDZ	aug-cc-pVTZ	cc-pVDZ	aug-cc-pVTZ
Electronic State	$\tilde{X} \ ^2B_1$	$\tilde{X} \ ^2B_1$	$\tilde{B} \ ^2A_2$	$\tilde{B} \ ^2A_2$
r C-O	1.256	1.252	1.244	1.244
r C <sub>1</sub> - C <sub>2</sub>	1.455	1.448	1.451	1.440
r C <sub>2</sub> - C <sub>3</sub>	1.380	1.371	1.439	1.433
r C <sub>3</sub> - C <sub>4</sub>	1.412	1.405	1.394	1.385
r C <sub>2</sub> - H <sub>1</sub>	1.092	1.081	1.093	1.082
r C <sub>3</sub> - H <sub>2</sub>	1.093	1.082	1.094	1.083
r C <sub>4</sub> - H <sub>3</sub>	1.092	1.081	1.089	1.078
a C <sub>6</sub> - C <sub>1</sub> - C <sub>2</sub>	117.0	117.1	111.7	112.1
a C <sub>1</sub> - C <sub>2</sub> - C <sub>3</sub>	121.0	120.8	123.6	123.3
a C <sub>2</sub> - C <sub>3</sub> - C <sub>4</sub>	120.2	120.3	122.4	122.4
a C <sub>1</sub> - C <sub>2</sub> - H <sub>1</sub>	116.9	117.1	117.3	117.7
a C <sub>4</sub> - C <sub>3</sub> - H <sub>2</sub>	119.5	119.4	119.7	119.7

# Appendix B

## Phenylperoxy

Table B.1: Harmonic vibrational constants for the  $\tilde{B}^2A''$  state derived from experimental data

Band progression	$\omega_e$
$23^\nu$	$278.0 \pm 0.6$
$20^\nu$	$539.0 \pm 0.6$
$19^\nu$	$657.0 \pm 2.3$
$22^\nu 23^\nu$	$278.0 \pm 4.6$
$20^\nu 23^\nu$	$275.5 \pm 0.3$
$19^\nu 23^\nu$	$270.5 \pm 2.7$

Table B.2: Complete list of bond lengths ( $\text{\AA}$ ) and bond angles ( $^\circ$ ) for the phenylperoxy radical calculated at the B3LYP/aug-cc-pVDZ level for  $\tilde{X}^2A''$ , and by TD-DFT for the excited electronic states.

Level	B3LYP	TD-DFT	TDDFT	TD-DFT
Electronic State	$\tilde{X}^2A''$	$\tilde{A}^2A'$	$\tilde{B}^2A''$	$\tilde{C}^2A''$
r O-O	1.321	1.372	1.492	1.456
r C-O	1.403	1.382	1.340	1.340
r C <sub>1</sub> - C <sub>6</sub>	1.397	1.401	1.407	1.427
r C <sub>6</sub> - C <sub>5</sub>	1.396	1.393	1.385	1.432
r C <sub>5</sub> - C <sub>4</sub>	1.400	1.402	1.432	1.379
r C <sub>4</sub> - C <sub>3</sub>	1.401	1.397	1.383	1.412
r C <sub>3</sub> - C <sub>2</sub>	1.397	1.399	1.408	1.433
r C <sub>2</sub> - C <sub>1</sub>	1.395	1.397	1.437	1.387
r C <sub>6</sub> - H <sub>6</sub>	1.089	1.089	1.089	1.090
r C <sub>5</sub> - H <sub>5</sub>	1.090	1.090	1.091	1.090
r C <sub>4</sub> - H <sub>4</sub>	1.090	1.090	1.089	1.088
r C <sub>3</sub> - H <sub>3</sub>	1.090	1.090	1.090	1.091
r C <sub>2</sub> - H <sub>2</sub>	1.087	1.088	1.084	1.086
a O <sub>8</sub> - O <sub>7</sub> - C <sub>1</sub>	115.3	114.2	107.2	110.5
a O <sub>7</sub> - C <sub>1</sub> - C <sub>2</sub>	123.1	122.9	122.9	125.2
a C <sub>2</sub> - C <sub>1</sub> - C <sub>6</sub>	122.6	122.0	120.2	117.6
a C <sub>1</sub> - C <sub>6</sub> - C <sub>5</sub>	118.5	118.5	119.0	121.7
a C <sub>6</sub> - C <sub>5</sub> - C <sub>4</sub>	120.2	120.7	121.7	122.7
a C <sub>5</sub> - C <sub>4</sub> - C <sub>3</sub>	120.0	119.6	119.2	117.4
a C <sub>4</sub> - C <sub>3</sub> - C <sub>2</sub>	120.8	120.9	120.7	122.8
a C <sub>3</sub> - C <sub>2</sub> - C <sub>1</sub>	117.9	118.3	119.3	119.8
a C <sub>1</sub> - C <sub>6</sub> - H <sub>6</sub>	119.7	119.8	119.4	118.5
a C <sub>4</sub> - C <sub>5</sub> - H <sub>5</sub>	120.2	120.1	119.1	120.9
a C <sub>1</sub> - C <sub>2</sub> - H <sub>2</sub>	120.0	120.5	117.8	118.7
a C <sub>4</sub> - C <sub>3</sub> - H <sub>3</sub>	119.9	120.1	120.4	119.4
a C <sub>5</sub> - C <sub>4</sub> - H <sub>4</sub>	120.0	120.2	119.6	121.9

Table B.3: Complete list of bond lengths ( $\text{\AA}$ ) and bond angles ( $^\circ$ ) for the phenylperoxy radical calculated at the B3LYP/aug-cc-pVTZ level for  $\tilde{X}^2A''$ , and by TD-DFT for the excited electronic states.

Level	B3LYP	TD-DFT	TD-DFT	TD-DFT
Electronic State	$\tilde{X}^2A''$	$\tilde{A}^2A'$	$\tilde{B}^2A''$	$\tilde{C}^2A''$
r O-O	1.321	1.371	1.497	1.456
r C-O	1.398	1.377	1.332	1.333
r C <sub>1</sub> - C <sub>6</sub>	1.389	1.393	1.402	1.418
r C <sub>6</sub> - C <sub>5</sub>	1.388	1.385	1.375	1.426
r C <sub>5</sub> - C <sub>4</sub>	1.391	1.394	1.424	1.370
r C <sub>4</sub> - C <sub>3</sub>	1.393	1.389	1.376	1.403
r C <sub>3</sub> - C <sub>2</sub>	1.388	1.391	1.398	1.427
r C <sub>2</sub> - C <sub>1</sub>	1.387	1.390	1.429	1.379
r C <sub>6</sub> - H <sub>6</sub>	1.081	1.080	1.080	1.081
r C <sub>5</sub> - H <sub>5</sub>	1.081	1.081	1.081	1.081
r C <sub>4</sub> - H <sub>4</sub>	1.081	1.081	1.080	1.079
r C <sub>3</sub> - H <sub>3</sub>	1.081	1.081	1.081	1.082
r C <sub>2</sub> - H <sub>2</sub>	1.078	1.079	1.074	1.077
a O <sub>8</sub> - O <sub>7</sub> - C <sub>1</sub>	115.5	114.5	107.4	110.8
a O <sub>7</sub> - C <sub>1</sub> - C <sub>2</sub>	123.1	122.9	123.1	125.3
a C <sub>2</sub> - C <sub>1</sub> - C <sub>6</sub>	122.4	121.8	120.0	117.3
a C <sub>1</sub> - C <sub>6</sub> - C <sub>5</sub>	118.6	118.6	119.1	121.9
a C <sub>6</sub> - C <sub>5</sub> - C <sub>4</sub>	120.1	120.7	121.6	120.7
a C <sub>5</sub> - C <sub>4</sub> - C <sub>3</sub>	120.0	119.6	119.3	117.3
a C <sub>4</sub> - C <sub>3</sub> - C <sub>2</sub>	120.7	120.8	120.7	122.8
a C <sub>3</sub> - C <sub>2</sub> - C <sub>1</sub>	118.1	118.4	119.4	120.0
a C <sub>1</sub> - C <sub>6</sub> - H <sub>6</sub>	119.6	119.7	119.2	118.4
a C <sub>4</sub> - C <sub>5</sub> - H <sub>5</sub>	120.2	120.1	119.1	120.9
a C <sub>1</sub> - C <sub>2</sub> - H <sub>2</sub>	120.0	120.4	117.8	118.6
a C <sub>4</sub> - C <sub>3</sub> - H <sub>3</sub>	119.9	120.1	120.4	119.5
a C <sub>5</sub> - C <sub>4</sub> - H <sub>4</sub>	120.0	120.2	119.6	121.9

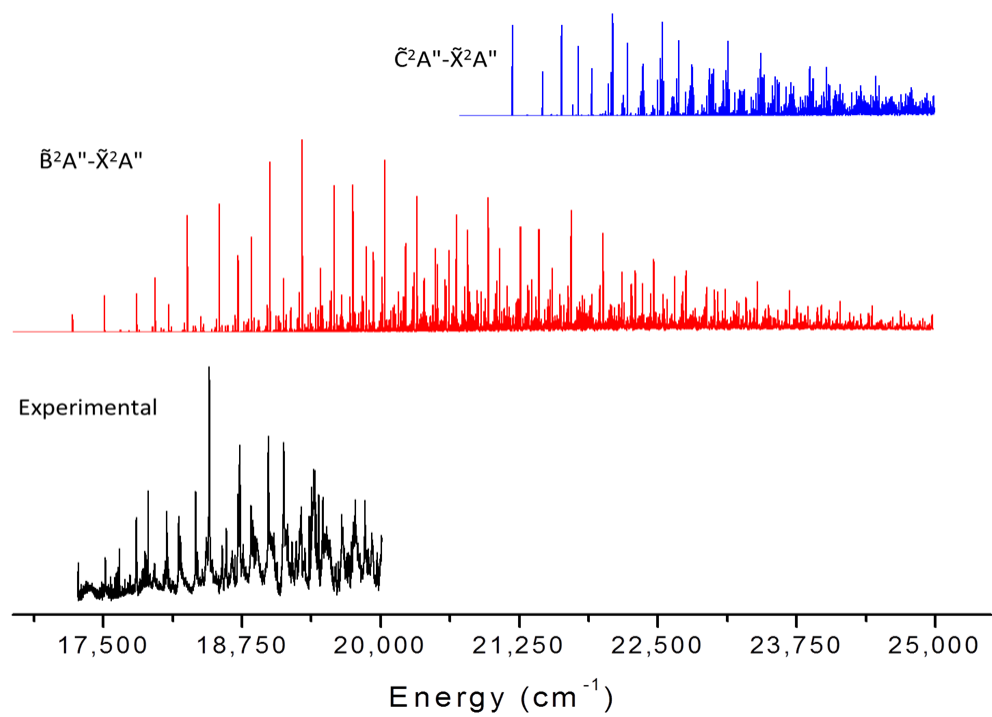


Figure B.1: Calculated vibrationally resolved electronic spectra for the  $\tilde{B}^2A'' \leftarrow \tilde{X}^2A''$  and  $\tilde{C}^2A'' \leftarrow \tilde{X}^2A''$  transitions of phenylperoxy (with aug-cc-pVTZ basis set) compared to the experimental results.

Table B.4: Calculated and scaled normal mode frequencies ( $\text{cm}^{-1}$ ) for the phenylperoxy radical in the  $\tilde{\text{A}} \ ^2\text{A}'$  electronic state compared with experimental term values,  $G(\nu')$ . The  $\tilde{\text{A}} \ ^2\text{A}'$  experimental values were reported by Just *et al.*[238]

mode assignment	Sym.	$\omega$	Exp.
1.00 $\nu_1$	$a'$	3,206	
.097 $\nu_3$	$a'$	3,202	
1.00 $\nu_2$	$a'$	3,195	
1.00 $\nu_4$	$a'$	3,181	
0.92 $\nu_5$	$a'$	3,173	
1.00 $\nu_6$	$a'$	1,631	
0.22 $\nu_8$ + 0.69 $\nu_7$	$a'$	1,621	
0.76 $\nu_8$ + 0.24 $\nu_7$	$a'$	1,513	
1.00 $\nu_9$	$a'$	1,493	
0.99 $\nu_{10}$	$a'$	1,356	
0.94 $\nu_{11}$	$a'$	1,334	900
0.97 $\nu_{12}$	$a'$	1,209	
0.95 $\nu_{13}$	$a'$	1,182	944
0.90 $\nu_{14}$	$a'$	1,171	
0.94 $\nu_{15}$	$a'$	1,101	
0.18 $\nu_{20}$ + 0.79 $\nu_{16}$	$a'$	1,046	
0.52 $\nu_{20}$ + 0.17 $\nu_{17}$ + 0.18 $\nu_{16}$	$a'$	1,033	
0.13 $\nu_{20}$ + 0.81 $\nu_{17}$	$a'$	1,012	
0.91 $\nu_{18}$	$a'$	797	
0.12 $\nu_{21}$ + 0.79 $\nu_{18}$	$a'$	627	
0.75 $\nu_{21}$	$a'$	563	
0.91 $\nu_{22}$	$a'$	432	
0.93 $\nu_{23}$	$a'$	229	213
0.95 $\nu_{24}$	$a''$	1,004	
0.95 $\nu_{25}$	$a''$	982	
0.96 $\nu_{26}$	$a''$	905	
0.20 $\nu_{28}$ + 0.80 $\nu_{27}$	$a''$	831	
0.80 $\nu_{28}$ + 0.20 $\nu_{27}$	$a''$	766	
0.98 $\nu_{29}$	$a''$	698	
0.98 $\nu_{30}$	$a''$	508	
0.93 $\nu_{31}$	$a''$	418	
0.89 $\nu_{32}$	$a''$	226	
0.88 $\nu_{32}$	$a''$	97	53

Table B.5: Calculated normal mode frequencies ( $\text{cm}^{-1}$ ) for the phenylperoxy radical in the  $\tilde{C}^2A''$  electronic state.

mode assignment	Sym.	$\omega$
$0.97\nu_1$	$a'$	3,147
$0.90\nu_2$	$a'$	3,117
$0.99\nu_3$	$a'$	3,096
$0.93\nu_4$	$a'$	3,084
$0.21\nu_{10} + 0.56\nu_9$	$a'$	3,077
$0.94\nu_5$	$a'$	3,013
$0.93\nu_6$	$a'$	1,616
$0.96\nu_7$	$a'$	1,509
$0.90\nu_8$	$a'$	1,389
$0.65\nu_{10} + 0.27\nu_9$	$a'$	1,354
$0.86\nu_{11}$	$a'$	1,317
$0.77\nu_{12}$	$a'$	1,291
$0.78\nu_{13}$	$a'$	1,168
$0.65\nu_{20}$	$a'$	1,152
$0.91\nu_{15}$	$a'$	1,031
$0.98\nu_{14}$	$a'$	980
$0.16\nu_{17} + 0.69\nu_{16}$	$a'$	964
$0.52\nu_{18} + 0.24\nu_{17} + 0.21\nu_{16}$	$a'$	956
$0.35\nu_{18} + 0.57\nu_{17}$	$a'$	812
$0.85\nu_{20}$	$a'$	574
$0.30\nu_{22} + 0.49\nu_{19}$	$a'$	449
$0.21\nu_{24} + 0.42\nu_{23} + 0.20\nu_{19}$	$a'$	405
$0.32\nu_{24} + 0.36\nu_{22}$	$a'$	262
$0.32\nu_{24} + 0.50\nu_{23}$	$a''$	949
$0.88\nu_{25}$	$a''$	875
$0.83\nu_{26}$	$a''$	859
$0.31\nu_{28} + 0.64\nu_{27}$	$a''$	854
$0.43\nu_{28} + 0.21\nu_{27}$	$a''$	709
$0.16\nu_{31} + 0.81\nu_{29}$	$a''$	633
$0.86\nu_{30}$	$a''$	429
$0.75\nu_{32} + 0.12\nu_{31}$	$a''$	332
$0.20\nu_{32} + 0.54\nu_{31} + 0.12\nu_{29}$	$a''$	170
$0.86\nu_{32}$	$a''$	65

# Appendix C

## CaOCa

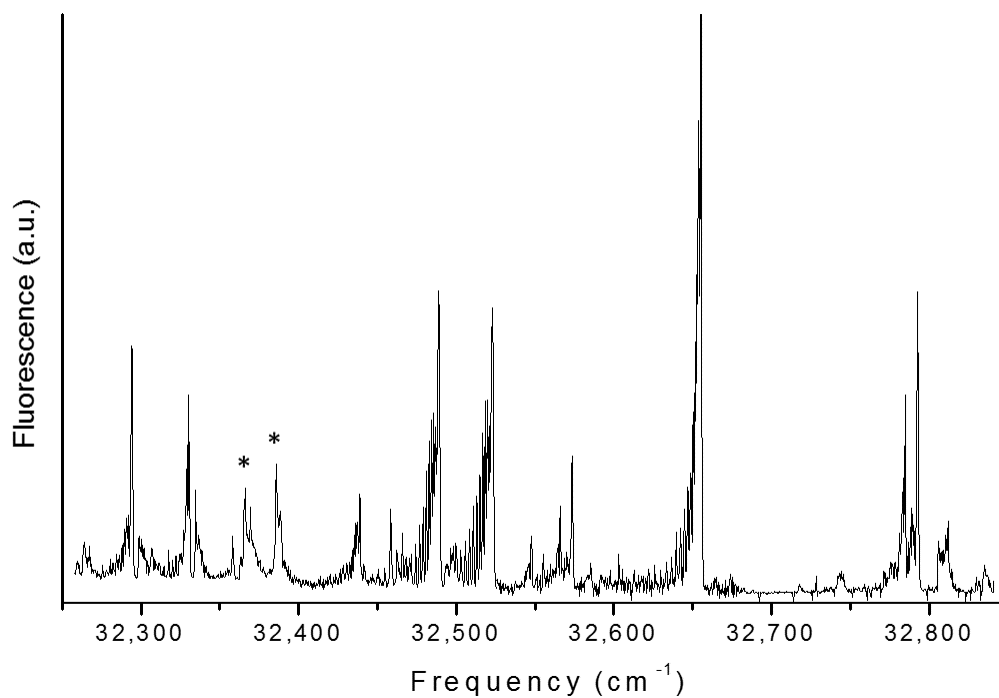


Figure C.1: LIF scan containing unassigned vibronic bands from laser ablation of a Ca rod. The structureless features denoted as \* do not originate from CaO, but from a larger molecular species. This spectrum was collected by two graduate students in the Heaven Lab, Josh Bartlett and Robert VanGundy.

# Bibliography

- [1] T. F. Stocker, D. Qin, G.-K. Plattner, M. Tignor, S. K. Allen, J. Boschung, A. Nauels, Y. Xia, V. Bex, and P. M. Midgley, “Climate Change 2013: The Physical Science Basis,” Tech. rep., Intergovernmental Panel on Climate Change, Working Group I Contribution to the IPCC Fifth Assessment Report (AR5)(Cambridge University Press, Cambridge, United Kingdom and New York, NY, USA. (2013).
- [2] S. VijayaVenkataRaman, S. Iniyan, and R. Goic, *Renew. Sust. Energ. Rev.* **16**, 878 (2012).
- [3] J. H. Kroll, and J. H. Seinfeld, *Atmos. Environ.* **42**, 3593 (2008).
- [4] M. Hallquist, J. C. Wenger, U. Baltensperger, Y. Rudich, D. Simpson, M. Claeys, J. Dommen, N. M. Donahue, C. George, A. H. Goldstein, J. F. Hamilton, H. Herrmann, T. Hoffmann, Y. Iinuma, M. Jang, M. E. Jenkin, J. L. Jimenez, A. Kiendler-Scharr, W. Maenhaut, G. McFiggans, T. F. Mentel, A. Monod, A. S. H. Prévôt, J. H. Seinfeld, J. D. Surratt, R. Szmigielski, and J. Wildt, *Atmos. Chem. Phys.* **9**, 5155 (2009).
- [5] N. M. Donahue, A. L. Robinson, and S. N. Pandis, *Atmos. Environ.* **43**, 94 (2009).
- [6] F. Will, and A. Boretti, *SAE International* **4**, 175 (2011).

- [7] R. van Basshuysen, and F. Schaefer, *Internal Combustion Engine Handbook* (SAE International, 2004).
- [8] A. Roberts, R. Brooks, and P. Shipway, *Energ. Convers. and Manage.* **82**, 327 (2014).
- [9] K. Ravindra, R. Sokhi, and R. Van Grieken, *Atmos. Environ.* **42**, 2895 (2008).
- [10] I. Glassman, and R. A. Yetter, *Combustion*, 4th ed. (Academic Press, 2008).
- [11] A. A. Abdel-Rahman, *Int. J. Energy Res.* **22**, 483 (1998).
- [12] I. Glassman, *Proc. Combust. Inst.* **22**, 295 (1989).
- [13] J. Hill, S. Polasky, E. Nelson, D. Tilman, H. Huo, L. Ludwig, J. Neumann, H. Zheng, and D. Bonta, *Proc. Natl. Acad. Sci. U.S.A.* **106**, 2077 (2009).
- [14] C. L. Friedman, Y. Zhang, and N. E. Selin, *Environ. Sci. Technol.* **48**, 429 (2014).
- [15] J. M. Delgado-Saborit, M. S. Alam, K. J. Godri Pollitt, C. Stark, and R. M. Harrison, *Atmos. Environ.* **77**, 974 (2013).
- [16] M. S. Alam, J. M. Delgado-Saborit, C. Stark, and R. M. Harrison, *Atmos. Environ.* **77**, 24 (2013).
- [17] E. Jang, M. S. Alam, and R. M. Harrison, *Atmos. Environ.* **79**, 271 (2013).
- [18] W. Yan, J. Chi, Z. Wang, W. Huang, and G. Zhang, *Environ. Pollut.* **157**, 1823 (2009).
- [19] D. Kaiser, I. Hand, Daniela Unger, D. E. Schulz-Bull, and J. J. Waniek, *Marine Poll. Bull.* **101**, 972 (2015).

- [20] Y. Chen, Y. Feng, S. Xiong, D. Liu, G. Wang, G. Sheng, and J. Fu, *Environ. Monit. Assess.* **172**, 235 (2011).
- [21] M. B. Yunker, R. W. Macdonald, R. Vingarzan, R. H. Mitchell, D. Goyette, and S. Sylvestre, *Org. Geochem.* **33**, 489 (2002).
- [22] A. Shannigrahi, T. Fukushima, and N. Ozaki, *Atmos. Environ.* **39**, 653 (2005).
- [23] S. Del Vento, and J. Dachs, *Environ. Sci. Technol.* **41**, 5608 (2007).
- [24] M. I. Cerezo, and S. Agusti, *Marine Poll. Bull.* **101**, 726 (2015).
- [25] M. Shiaris, and D. Jambard-Sweet, *Marine Poll. Bull.* **17**, 469 (1986).
- [26] J. Yan, L. Wang, P. P. Fu, and H. Yu, *Mutat. Res.* **557**, 99 (2004).
- [27] L. Huang, S. Chernyak, and S. Batterman, *Sci. Total Environ.* **487**, 173 (2014).
- [28] K.-H. Kim, S. A. Jahan, E. Kabir, and R. J. Brown, *Environ. Int.* **60**, 71 (2013).
- [29] G. D'Amato, C. E. Baena-Cagnani, L. Cecchi, I. Annesi-Maesano, C. Nunes, I. Ansotegui, M. D'Amato, G. Liccardi, M. Sofia, and W. G. Canonica, *Multi-discip. Respir. Med.* **8**, 12 (2013).
- [30] T. Rengarajan, P. Rajendran, N. Nandakumar, B. Lokeshkumar, P. Rajendran, and I. Nishigaki, *Asian Pac. J. Trop. Biomed.* **5**, 182 (2015).
- [31] D. J. Cook, S. Schlemmer, N. Balucani, D. R. Wagner, B. Steiner, and R. J. Saykally, *Nature* **380**, 227 (1996).
- [32] L. J. Allamandola, A. Tielens, and J. R. Barker, *Astrophys. J.* **290**, L25 (1985).
- [33] R. Ruiterkamp, T. H. inski, F. Salama, B. H. Foing, L. J. Allamandola, W. Schmidt, and P. Ehrenfreund, *Astron. Astrophys.* **390**, 1153 (2002).

- [34] F. Salama, G. A. Galazutdinov, J. Krelowski, L. Biennier, Y. Beletsky, and I.-O. Song, *Astrophys. J.* **728**, 154 (2011).
- [35] M. Frenklach, and H. Wang, *Proc. Combust. Inst.* **23**, 1559 (1991).
- [36] M. Frenklach, and J. Warnatz, *Combust. Sci. Technol.* **51**, 265 (1987).
- [37] A. D'Anna, A. violi, and A. D'Alessio, *Combust. Flame* **121**, 418 (2000).
- [38] M. Frenklach, D. W. Clary, W. C. Gardiner, and S. E. Stein, *Proc. Combust. Inst.* **20**, 887 (1985).
- [39] M. Frenklach, D. W. Clary, W. C. Gardiner, and S. E. Stein, *Proc. Combust. Inst.* **21**, 1067 (1988).
- [40] M. Frenklach, W. C. Gardiner, S. Stein, D. Clary, and T. Yuan, *Combust. Sci. Technol.* **50**, 79 (1986).
- [41] M. Frenklach, T. Yuan, and M. K. Ramachandra, *Energy Fuels* **2**, 462 (1988).
- [42] J. A. Miller, and C. F. Melius, *Combust. Flame* **91**, 21 (1992).
- [43] C. L. Parker, and A. L. Cooksy, *J. Phys. Chem. A* **103**, 2160 (1999).
- [44] J. A. Miller, and S. J. Klippenstein, *J. Phys. Chem. A* **105**, 7254 (2001).
- [45] X. Krokidis, N. W. Moriarty, W. A. Lester, and M. Frenklach, *Int. J. Chem. Kinet.* **33**, 808 (2001).
- [46] M. Frenklach, *Phys. Chem. Chem. Phys.* **4**, 2028 (2002).
- [47] B. Shukla, A. Susa, A. Miyoshi, and M. Koshi, *J. Phys. Chem. A* **112**, 2362 (2008).
- [48] V. V. Kislov, A. I. Sadovnikov, and A. M. Mebel, *J. Phys. Chem. A* **117**, 4794 (2013).

- [49] H. Böhm, H. Jander, and D. Tanke, *Proc. Combust. Inst.* **27**, 1605 (1998).
- [50] T. J. Mckinnon, and J. B. Howard, *Proc. Combust. Inst.* **24**, 965 (1992).
- [51] F. Xu, X. Shi, Q. Zhang, and W. Wang, *Chemosphere* **162**, 345 (2016).
- [52] C. F. Melius, M. E. Colvin, N. M. Marinov, W. J. Pit, and S. M. Senkan, *Proc. Combust. Inst.* **26**, 685 (1996).
- [53] J. Mulholland, M. Lu, and D.-H. Kim, *Proc. Combust. Inst.* **28**, 2593 (2000).
- [54] H. Richter, and J. Howard, *Prog. Energy Combust. Sci.* **26**, 565 (2000).
- [55] N. M. Marinov, W. J. Pitz, C. K. Westbrook, A. M. Vincitore, M. J. Castaldi, S. M. Senkan, and C. F. Melius, *Combust. Flame* **114**, 192 (1998).
- [56] M. Frenklach, S. Taki, M. Durgaprasad, and R. Matula, *Combust. Flame* **54**, 81 (1983).
- [57] A. Gomez, G. Sidebotham, and I. Glassman, *Combust. Flame* **58**, 45 (1984).
- [58] N. M. Marinov, M. J. Castaldi, C. F. Melius, and W. Tsang, *Combust. Sci. Technol.* **128**, 295 (1997).
- [59] H. Bockhorn, ed., *Soot Formation in Combustion*, Springer Series in Chemical Physics (Springer-Verlag Berlin Heidelberg, 1994).
- [60] S. H. Bauer, and C. F. Aten, *J. Chem. Phys.* **39**, 1253 (1963).
- [61] I. V. Tokmakov, G.-S. Kim, V. V. Kislov, A. M. Mebel, and M. C. Lin, *J. Phys. Chem. A* **109**, 6114 (2005).
- [62] D. R. Albert, and H. F. Davis, *J. Phys. Chem. Lett.* **1**, 1107 (2010).
- [63] X. Gu, F. Zhang, and R. I. Kaiser, *Chem. Phys. Lett.* **448**, 7 (2007).

- [64] P. Frank, J. Herzler, T. Just, and C. Wahl, *Proc. Combust. Inst.* **25**, 833 (1994).
- [65] C.-Y. Lin, and M. C. Lin, *J. Phys. Chem.* **90**, 425 (1986).
- [66] K. Tonokura, T. Ogura, and M. Koshi, *J. Phys. Chem. A* **108**, 7801 (2004).
- [67] Z. B. Alfassi, G. I. Khaikin, and P. Neta, *J. Phys. Chem.* **99**, 265 (1995).
- [68] J. L. Kinsey, *Annu. Rev. Phys. Chem.* **28**, 349 (1977).
- [69] P. M. Doherty, and D. R. Crosley, *Appl. Opt.* **23**, 713 (1984).
- [70] J. M. Seitzman, J. Haumann, and R. K. Hanson, *Appl. Opt.* **26**, 2892 (1987).
- [71] Z. Chi, B. M. Cullum, D. L. Stokes, J. Mobley, G. H. Miller, M. R. Hajaligol, and T. Vo-Dinh, *Spectrochim. Acta Mol. Biomol. Spectrosc.* **57**, 1377 (2001).
- [72] L. R. Allain, D. N. Stratis, B. M. Cullum, J. Mobley, M. R. Hajaligol, and T. Vo-Dinh, *J. Anal. Appl. Pyrol.* **66**, 145 (2003).
- [73] P. Liu, Z. He, G.-L. Hou, B. Guan, H. Lin, and Z. Huang, *J. Phys. Chem. A* **119**, 13009 (2015).
- [74] K. Freel, J. Park, M. Lin, and M. C. Heaven, *Chem. Phys. Lett.* **507**, 216 (2011).
- [75] T. Yu, and M. C. Lin, *J. Am. Chem. Soc.* **115**, 4371 (1993).
- [76] P. S. Thomas, and T. A. Miller, *Chem. Phys. Lett.* **491**, 123 (2010).
- [77] P. S. Thomas, and T. A. Miller, *Chem. Phys. Lett.* **514**, 196 (2011).
- [78] P. S. Thomas, R. Chhantyal-Pun, and T. A. Miller, *J. Phys. Chem. A* **114**, 218 (2010).
- [79] W. Shenghai, P. Dupre, P. Rupper, and T. A. Miller, *J. Chem. Phys.* **127**, 224305 (2007).

- [80] K. Tonokura, Y. Norikane, M. Koshi, Y. Nakano, S. Nakamichi, M. Goto, S. Hashimoto, M. Kawasaki, M. P. Sulbaek Andersen, M. D. Hurley, and T. J. Wallington, *J. Phys. Chem. A* **106**, 5908 (2002).
- [81] T. Yu, and M. C. Lin, *J. Am. Chem. Soc.* **116**, 9571 (1994).
- [82] J. Park, G. J. Nam, I. V. Tokmakov, and M. C. Lin, *J. Phys. Chem. A* **110**, 8729 (2006).
- [83] J. Park, I. V. Tokmakov, and M. C. Lin, *J. Phys. Chem. A* **111**, 6881 (2007).
- [84] T. D. Ladd, F. Jelezko, R. Laflamme, Y. Nakamura, C. Monroe, and J. L. O'Brien, *Nature* **464**, 45 (2010).
- [85] D. DeMille, *Phys. Rev. Lett.* **88**, 067901 (2002).
- [86] A. Negretti, P. Treutlein, and T. Calarco, *Quantum Inf. Process.* **10**, 721 (2011).
- [87] B. M. Roberts, Y. V. Stadnik, V. A. Dzuba, V. V. Flambaum, N. Leefer, and D. Budker, *Phys. Rev. D* **90**, 096005 (2014).
- [88] R. V. Krems, *Phys. Chem. Chem. Phys.* **10**, 4079 (2008).
- [89] N. Balakrishnan, and A. Dalgarno, *Chem. Phys. Lett.* **341**, 652 (2001).
- [90] N. Huntemann, *Physics* **10**, 9 (2017).
- [91] T. E. Wall, *J. Phys. B* **49**, 243001 (2016).
- [92] The ACME Collaboration, J. Baron, W. C. Campbell, D. DeMille, J. M. Doyle, G. Gabrielse, Y. V. Gurevich, P. W. Hess, N. R. Hutzler, E. Kirilov, I. Kozyryev, B. R. O'Leary, C. D. Panda, M. F. Parsons, E. S. Petrik, B. Spaun, A. C. Vutha, and A. D. West, *Science* **343**, 269 (2014).
- [93] V. V. Flambaum, and M. G. Kozlov, *Phys. Rev. Lett.* **99**, 150801 (2007).

- [94] M. R. Tarbutt, B. E. Sauer, J. J. Hudson, and E. A. Hinds, *New J. Phys.* **15**, 053034 (2013).
- [95] D. DeMille, S. Sainis, J. Sage, T. Bergeman, S. Kotochigova, and E. Tiesinga, *Phys. Rev. Lett.* **100**, 043202 (2008).
- [96] S. Truppe, R. Hendricks, S. Tokunaga, H. Lewandowski, M. Kozlov, C. Henkel, E. Hinds, and M. Tarbutt, *Nat. Commun.* **4**, 2600 (2013).
- [97] E. R. Hudson, H. J. Lewandowski, B. C. Sawyer, and J. Ye, *Phys. Rev. Lett.* **96**, 143004 (2006).
- [98] B. Ravaine, M. G. Kozlov, and A. Derevianko, *Phys. Rev. A* **72**, 012101 (2005).
- [99] D. DeMille, S. B. Cahn, D. Murphree, D. A. Rahmlow, and M. G. Kozlov, *Phys. Rev. Lett.* **100**, 023003 (2008).
- [100] S. Bose, *Z. Phys.* **26**, 178 (1924).
- [101] A. Einstein, *Sitzungsber. Kgl. Preuss. Akad. Wiss., Phys. Math. Kl.* **3**, 18 (1925).
- [102] T. Hänsch, and A. Schawlow, *Opt. Commun.* **13**, 68 (1975).
- [103] C. N. Cohen-Tannoudji, and W. D. Phillips, *Phys. Today* **43**, 33 (1990).
- [104] S. Chu, *Rev. Mod. Phys.* **70**, 685 (1998).
- [105] C. N. Cohen-Tannoudji, *Rev. Mod. Phys.* **70**, 707 (1998).
- [106] W. D. Phillips, *Rev. Mod. Phys.* **70**, 721 (1998).
- [107] S. Chu, L. Hollberg, J. E. Bjorkholm, A. Cable, and A. Ashkin, *Phys. Rev. Lett.* **55**, 48 (1985).

- [108] E. L. Raab, M. Prentiss, A. Cable, S. Chu, and D. E. Pritchard, *Phys. Rev. Lett.* **59**, 2631 (1987).
- [109] M. H. Anderson, J. R. Ensher, M. R. Matthews, C. E. Wieman, and E. A. Cornell, *Science* **269**, 198 (1995).
- [110] C. C. Bradley, C. A. Sackett, J. J. Tollett, and R. G. Hulet, *Phys. Rev. Lett.* **75**, 1687 (1995).
- [111] K. B. Davis, M. O. Mewes, M. R. Andrews, N. J. van Druten, D. S. Durfee, D. M. Kurn, and W. Ketterle, *Phys. Rev. Lett.* **75**, 3969 (1995).
- [112] W. Ketterle, *Rev. Mod. Phys.* **74**, 1131 (2002).
- [113] E. A. Cornell, and C. E. Wieman, *Rev. Mod. Phys.* **74**, 875 (2002).
- [114] M. D. Di Rosa, *Eur. Phys. J. D* **31**, 395 (2004).
- [115] B. K. Stuhl, B. C. Sawyer, D. Wang, and J. Ye, *Phys. Rev. Lett.* **101**, 243002 (2008).
- [116] B. Hemmerling, E. Chae, A. Ravi, L. Anderegg, G. K. Drayna, N. R. Hutzler, A. L. Collopy, J. Ye, W. Ketterle, and J. M. Doyle, *J. Phys. B* **49**, 174001 (2016).
- [117] Y. Yin, Y. Xia, X. Li, X. Yang, S. Xu, and J. Yin, *Appl. Phys. Express* **8**, 092701 (2015).
- [118] R. Yang, B. Tang, and T. Gao, *Chin. Phys. B* **25**, 043101 (2016).
- [119] N. Wells, and I. C. Lane, *Phys. Chem. Chem. Phys.* **13**, 19018 (2011).
- [120] X. Zhuang, A. Le, T. C. Steimle, N. E. Bulleid, I. J. Smallman, R. J. Hendricks, S. M. Skoff, J. J. Hudson, B. E. Sauer, E. A. Hinds, and M. R. Tarbutt, *Phys. Chem. Chem. Phys.* **13**, 19013 (2011).

- [121] T. A. Isaev, S. Hoekstra, and R. Berger, *Phys. Rev. A* **82**, 052521 (2010).
- [122] E. S. Shuman, J. F. Barry, D. R. Glenn, and D. DeMille, *Phys. Rev. Lett.* **103**, 223001 (2009).
- [123] E. S. Shuman, J. F. Barry, and D. DeMille, *Nature* **467**, 820 (2010).
- [124] V. Zhelyazkova, A. Cournol, T. E. Wall, A. Matsushima, J. J. Hudson, E. A. Hinds, M. R. Tarbutt, and B. E. Sauer, *Phys. Rev. A* **89**, 053416 (2014).
- [125] M. T. Hummon, M. Yeo, B. K. Stuhl, A. L. Collopy, Y. Xia, and J. Ye, *Phys. Rev. Lett.* **110**, 143001 (2013).
- [126] M. Yeo, *The Laser Cooling and Magneto-Optical Trapping of the YO Molecule*, Ph.D. thesis, University of Colorado (2015).
- [127] D. J. McCarron, E. B. Norrgard, M. H. Steinecker, and D. DeMille, *New J. Phys.* **17**, 035014 (2015).
- [128] E. B. Norrgard, D. J. McCarron, M. H. Steinecker, M. R. Tarbutt, and D. DeMille, *Phys. Rev. Lett.* **116**, 063004 (2016).
- [129] T. A. Isaev, and R. Berger, *Phys. Rev. Lett.* **116**, 063006 (2016).
- [130] I. Kozyryev, L. Baum, K. Matsuda, B. Hemmerling, and J. M. Doyle, *J. Phys. B* **49**, 134002 (2016).
- [131] L. D. Carr, D. DeMille, R. V. Krems, and J. Ye, *New J. Phys.* **11**, 055049 (2009).
- [132] G. Quéméner, and P. S. Julienne, *Chem. Rev.* **112**, 4949 (2012).
- [133] O. Dulieu, and C. Gabbanini, *Rep. Prog. Phys.* **72**, 086401 (2009).
- [134] K. Mølhave, and M. Drewsen, *Phys. Rev. A* **62**, 011401 (2000).

- [135] A. Bertelsen, S. Jørgensen, and M. Drewsen, *J. Phys. B* **39**, L83 (2006).
- [136] M. Drewsen, *Physica B* **460**, 105 (2015), special Issue on Electronic Crystals (ECRYS-2014).
- [137] R. Rugango, A. T. Calvin, S. Janardan, G. Shu, and K. R. Brown, *ChemPhysChem* **17**, 3764 (2016).
- [138] R. Rugango, J. E. Goeders, T. H. Dixon, J. M. Gray, N. B. Khanyile, G. Shu, R. J. Clark, and K. R. Brown, *New J. Phys.* **17**, 035009 (2015).
- [139] K. Højbjerg, A. K. Hansen, P. S. Skyt, P. F. Staanum, and M. Drewsen, *New J. Phys.* **11**, 055026 (2009).
- [140] P. F. Staanum, K. Højbjerg, P. S. Skyt, A. K. Hansen, and M. Drewsen, *Nature Phys.* **6**, 271 (2010).
- [141] A. K. Hansen, O. O. Versolato, L. Klosowski, S. B. Kristensen, A. Gingell, M. Schwarz, A. Windberger, J. Ullrich, J. R. C. Lopez-Urrutia, and M. Drewsen, *Nature* **508**, 76 (2014).
- [142] E. R. Hudson, *Phys. Rev. A* **79**, 032716 (2009).
- [143] W. G. Rellergert, S. T. Sullivan, S. J. Schowalter, S. Kotochigova, K. Chen, and E. R. Hudson, *Nature* **495**, 490 (2013).
- [144] T. Stoecklin, P. Halvick, M. A. Gannouni, M. Hochlaf, S. Kotochigova, and E. R. Hudson, *Nature Commun.* **7**, 11234 (2016).
- [145] E. R. Hudson, in “Joint ARO MURI Meeting on Ultracold Molecular Ions and Ultracold Chemistry, Emory University, Oct. 8<sup>th</sup>,” (2016).
- [146] J. M. Merritt, V. E. Bondybey, and M. C. Heaven, *J. Phys. Chem. A* **113**, 13300 (2009).

- [147] M. C. Heaven, V. E. Bondybey, J. M. Merritt, and A. L. Kaledin, *Chem. Phys. Lett.* **506**, 1 (2011).
- [148] R. Lindner, H.-J. Dietrich, and K. Müller-Dethlefs, *Chem. Phys. Lett.* **228**, 417 (1994).
- [149] J. M. Herbelin, J. A. McKay, M. A. Kwok, R. H. Ueunten, D. S. Urevig, D. J. Spencer, and D. J. Benard, *Appl. Opt.* **19**, 144 (1980).
- [150] D. Z. Anderson, J. C. Frisch, and C. S. Masser, *Appl. Opt.* **23**, 1238 (1984).
- [151] A. O’Keefe, and D. A. G. Deacon, *Rev. Sci. Instrum.* **59**, 2544 (1988).
- [152] A. O’Keefe, J. J. Scherer, J. B. Paul, and R. J. Saykally, *Cavity-Ringdown Laser Spectroscopy History, Development, and Applications*, chap. 6, 71–92 (American Chemical Society, 1999).
- [153] A. O’Keefe, and O. Lee, *American Laboratory* (1989, Dec 19).
- [154] A. O’Keefe, J. Scherer, A. Cooksy, R. Sheeks, J. Heath, and R. Saykally, *Chem. Phys. Lett.* **172**, 214 (1990).
- [155] G. Berden, and R. Engeln, eds., *Cavity Ring-Down Spectroscopy: Techniques and Applications* (Blackwell Publishing, Ltd., 2009).
- [156] J. U. White, *J. Opt. Soc. Am.* **32**, 285 (1942).
- [157] D. R. Herriot, H. Kogelnik, and R. Kompfner, *Appl. Opt.* **3**, 523 (1964).
- [158] D. R. Herriot, and J. H. Schulte, *Appl. Opt.* **4**, 883 (1965).
- [159] K. K. Lehman, G. Berden, and R. Engeln, *Cavity Ring-Down Spectroscopy: Techniques and Applications*, chap. 1, 1–26 (Blackwell Publishing, Ltd., 2009).

- [160] M. N. Sullivan, *Testing and Optimization of a Cavity Ringdown Spectrometer*, Master's thesis, Arkansas State University (2011).
- [161] K. W. Busch, and M. A. Busch, *Introduction to Cavity-Ringdown Spectroscopy*, chap. 2, 7–19 (American Chemical Society, 1999).
- [162] T. H. Maiman, *Nature* **187**, 493 (1960).
- [163] W. J. Tango, J. K. Link, and R. N. Zare, *J. Chem. Phys.* **49**, 4264 (1968).
- [164] M. L. Spaeth, and D. P. Bortfeld, *Appl. Phys. Lett.* **9**, 179 (1966).
- [165] D. S. Bethune, and J. J. Wynne, *Proc. Natl. Acad. Sci. U.S.A.* **113**, 12 (2016).
- [166] F. P. Schäfer, ed., *Dye Lasers*, 2<sup>nd</sup> ed. (Springer-Verlag, Berlin, 1990).
- [167] R. N. Zare, *Annual Rev. Anal. Chem.* **5**, 1 (2012).
- [168] I. Estermann, *Rev. Mod. Phys.* **18**, 300 (1946).
- [169] N. Ramsey, *Molecular Beams* (Oxford University Press, 1956).
- [170] A. Kantrowitz, and J. Grey, *Rev. Sci. Instrum.* **22**, 328 (1951).
- [171] J. M. Hollas, *Modern Spectroscopy*, 4th ed. (John Wiley & Sons, Ltd., 2004).
- [172] S. Y. T. Van de Meerakker, L. Bethlem, Hendrick, and G. Meijer, *Nature Phys.* **4**, 595 (2008).
- [173] R. E. Smalley, L. Wharton, and D. H. Levy, *Acc. Chem. Res.* **10**, 139 (1977).
- [174] M. D. Morse, in F. Dunning, and R. G. Hulet, eds., “Atomic, Molecular, and Optical Physics: Atoms and Molecules,” , vol. 29, Part Bchap. 2, 21–47 (Academic Press, 1996).
- [175] S. J. Sibener, R. J. Buss, P. Casavecchia, T. Hirooka, and Y. T. Lee, *J. Chem. Phys.* **72**, 4341 (1980).

- [176] K. Brezinsky, *Prog. Energy Combust. Sci.* **12**, 1 (1986).
- [177] C.-Y. Lin, and M. C. Lin, *Int. J. Chem. Kinet.* **17**, 1025 (1985).
- [178] A. M. Mebel, and M. C. Lin, *J. Am. Chem. Soc.* **116**, 9577 (1994).
- [179] A. J. Colussi, F. Zabel, and S. W. Benson, *Int. J. Chem. Kinet.* **9**, 161 (1977).
- [180] N. M. Marinov, W. J. Pitz, C. K. Westbrook, M. J. Castaldi, and S. M. Senkan, *Combust Sci. Technol.* **116-117**, 211 (1996).
- [181] J. Platz, O. J. Nielsen, T. J. Wallington, J. C. Ball, M. D. Hurley, A. M. Straccia, W. F. Schneider, and J. Sehested, *J. Phys. Chem. A* **102**, 7964 (1998).
- [182] F. Berho, and R. Lesclaux, *Chem. Phys. Lett.* **279**, 289 (1997).
- [183] Z. Tao, and Z. Li, *Int. J. Chem. Kinet.* **31**, 65 (1999).
- [184] T. Yu, A. M. Mebel, and M. C. Lin, *J. Phys. Org. Chem.* **8**, 47 (1995).
- [185] H. M. Chang, H. H. Jaffe, and C. A. Masmanidis, *J. Phys. Chem.* **79**, 1118 (1975).
- [186] G. N. R. Tripathi, and R. H. Schuler, *J. Chem. Phys.* **81**, 113 (1984).
- [187] L. J. Johnston, N. Mathivanan, F. Negri, W. Siebrand, and F. Zerbetto, *Can. J. Chem.* **71**, 1655 (1993).
- [188] J. Spanget-Larsen, M. Gil, A. Gorski, D. M. Blake, J. Waluk, and J. G. Radziszewski, *J. Am. Chem. Soc.* **123**, 11253 (2001).
- [189] C.-W. Cheng, Y.-P. Lee, and H. A. Witek, *J. Phys. Chem. A* **112**, 2648 (2008).
- [190] D. M. Chipman, R. Liu, X. Zhou, and P. Pulay, *J. Chem. Phys.* **100**, 5023 (1994).

- [191] J. Takahashi, T. Momose, and T. Shida, *Bull. Chem. Soc. Jpn.* **67**, 964 (1994).
- [192] R. Liu, K. Morokuma, A. M. Mebel, and M. C. Lin, *J. Phys. Chem.* **100**, 9314 (1996).
- [193] T. Stone, and W. Waters, *Proc. Chem. Soc., London* 253 (1962).
- [194] W. Dixon, and R. O. C. Norman, *Proc. Chem. Soc., London* 97 (1963).
- [195] T. J. Stone, and W. A. Waters, *J. Chem. Soc.* 213–218 (1964).
- [196] W. T. Dixon, and R. O. C. Norman, *J. Chem. Soc.* 4857 (1964).
- [197] P. Neta, and R. W. Fessenden, *J. Phys. Chem.* **78**, 523 (1974).
- [198] W. T. Dixon, and D. Murphy, *J. Chem. Soc., Faraday Trans. 2* **72**, 1221 (1976).
- [199] S. M. Beck, and L. E. Brus, *J. Chem. Phys.* **76**, 4700 (1982).
- [200] C. R. Johnson, M. Ludwig, and S. A. Asher, *J. Am. Chem. Soc.* **108**, 905 (1986).
- [201] A. Mukherjee, M. L. McGlashen, and T. G. Spiro, *J. Phys. Chem.* **99**, 4912 (1995).
- [202] G. N. R. Tripathi, and R. H. Schuler, *J. Phys. Chem.* **92**, 5129 (1988).
- [203] R. Schnepf, A. Sokolowski, J. Müller, V. Bachler, K. Wieghardt, and P. Hildebrandt, *J. Am. Chem. Soc.* **120**, 2352 (1998).
- [204] H. Shindo, and J. Hiraishi, *Chem. Phys. Lett.* **80**, 238 (1981).
- [205] G. Tripathi, and R. H. Schuler, *Chem. Phys. Lett.* **98**, 594 (1983).
- [206] G. Porter, and F. G. Wright, *Trans. Faraday Soc.* **51**, 1469 (1955).
- [207] B. Ward, *Spectrochim. Acta, Part A: Mol. Spectrosc.* **24**, 813 (1968).

- [208] D. Pullin, and L. Andrews, *J. Mol. Struct.* **95**, 181 (1982).
- [209] J. G. Radziszewski, M. Gil, A. Gorski, J. Spanget-Larsen, J. Waluk, and B. J. Mroz, *J. Chem. Phys.* **115**, 9733 (2001).
- [210] M. Dierksen, and S. Grimme, *J. Chem. Phys.* **120**, 3544 (2004).
- [211] C.-W. Cheng, H. Witek, and Y.-P. Lee, *J. Chem. Phys.* **129**, 154307 (2008).
- [212] M. Araki, Y. Matsushita, and K. Tsukiyama, *Astron. J.* **150**, 113 (2015).
- [213] K. A. Freel, *Gas Phase Molecular Spectroscopy: Electronic Spectroscopy of Combustion Intermediates, Chloride Azide Kinetics, and Rovibrational Energy Transfer in Acetylene*, Ph.D. thesis, Emory University (2012).
- [214] H. Linnartz, O. Vaizert, P. Cias, L. Grüter, and J. Maier, *Chem. Phys. Lett.* **345**, 89 (2001).
- [215] L. Biennier, F. Salama, L. J. Allamandola, and J. J. Scherer, *J. Chem. Phys.* **118**, 7863 (2003).
- [216] A. Kramida, Y. Ralchenko, J. Reader, and NIST ASD Team, NIST Atomic Spectra Database (ver. 5.3), [Online]. Available: <http://physics.nist.gov/asd> [2017, January 12]. National Institute of Standards and Technology, Gaithersburg, MD. (2015).
- [217] M. J. Frisch, G. W. Trucks, H. B. Schlegel, G. E. Scuseria, M. A. Robb, J. R. Cheeseman, G. Scalmani, V. Barone, B. Mennucci, G. A. Petersson, H. Nakatsuji, M. Caricato, X. Li, H. P. Hratchian, A. F. Izmaylov, J. Bloino, G. Zheng, J. L. Sonnenberg, M. Hada, M. Ehara, K. Toyota, R. Fukuda, J. Hasegawa, M. Ishida, T. Nakajima, Y. Honda, O. Kitao, H. Nakai, T. Vreven, J. A. Montgomery, Jr., J. E. Peralta, F. Ogliaro, M. Bearpark, J. J. Heyd, E. Brothers, K. N. Kudin, V. N. Staroverov, R. Kobayashi, J. Normand, K. Raghavachari,

- A. Rendell, J. C. Burant, S. S. Iyengar, J. Tomasi, M. Cossi, N. Rega, J. M. Millam, M. Klene, J. E. Knox, J. B. Cross, V. Bakken, C. Adamo, J. Jaramillo, R. Gomperts, R. E. Stratmann, O. Yazyev, A. J. Austin, R. Cammi, C. Pomelli, J. W. Ochterski, R. L. Martin, K. Morokuma, V. G. Zakrzewski, G. A. Voth, P. Salvador, J. J. Dannenberg, S. Dapprich, A. D. Daniels, . Farkas, J. B. Foresman, J. V. Ortiz, J. Cioslowski, and D. J. Fox, “*Gaussian 09*, Revision A.1,” Gaussian Inc. Wallingford CT 2009.
- [218] T. H. Dunning, *J. Chem. Phys.* **90**, 1007 (1989).
- [219] K. Hagen, and K. Hedberg, *J. Chem. Phys.* **59**, 158 (1973).
- [220] NIST Computational Chemistry Comparison and Benchmark Database, NIST Standard Reference Database Number 101, Release 18, October 2016, Editor: Russell D. Johnson III, <http://cccbdb.nist.gov/>.
- [221] “NIST. Vibrational frequency scaling factors. Available from: <http://cccbdb.nist.gov/vibscale2.asp?method=8&basis=6>.” (2013).
- [222] J. Bloino, M. Biczysko, O. Crescenzi, and V. Barone, *J. Chem. Phys.* **128**, 244105 (2008).
- [223] M. Araki, K. Niwayama, and K. Tsukiyama, *Astron. J.* **148**, 87 (2014).
- [224] J. S. Lim, I. S. Lim, K.-S. Lee, D.-S. Ahn, Y. S. Lee, and S. K. Kim, *Angew. Chem. Int. Ed.* **45**, 6290 (2006).
- [225] I. S. Lim, J. S. Lim, Y. S. Lee, and S. K. Kim, *J. Chem. Phys.* **126**, 034306 (2007).
- [226] C. Western, “PGOPHER, *A Program for Simulating Rotational, Vibrational, and Electronic Spectra*, University of Bristol, <http://pgopher.chm.bris.ac.uk>,” (2013).

- [227] A. M. Schmoltner, D. S. Anex, and Y. T. Lee, *J. Phys. Chem.* **96**, 1236 (1992).
- [228] H.-H. Carstensen, and A. M. Dean, *Int. J. Chem. Kinet.* **44**, 75 (2012).
- [229] K. A. Freel, M. N. Sullivan, J. Park, M. C. Lin, and M. C. Heaven, *J. Phys. Chem. A* **117**, 7484 (2013).
- [230] K. Tanaka, M. Ando, Y. Sakamoto, and K. Tonokura, *Int. J. Chem. Kinet.* **44**, 41 (2012).
- [231] B. B. Kirk, D. G. Harman, H. I. Kenttamaa, A. J. Trevitt, and S. J. Blanksby, *Phys. Chem. Chem. Phys.* **14**, 16719 (2012).
- [232] D. S. N. Parker, F. Zhang, and R. I. Kaiser, *J. Phys. Chem. A* **115**, 11515 (2011).
- [233] N. Sebbar, H. Bockhorn, and J. Bozzelli, *Int. J. Chem. Kinet.* **40**, 583 (2008).
- [234] G. da Silva, and J. W. Bozzelli, *J. Phys. Chem. A* **112**, 3566 (2008).
- [235] J. K. Merle, and C. M. Hadad, *J. Phys. Chem. A* **108**, 8419 (2004).
- [236] J. L. Weisman, and M. Head-Gordon, *J. Am. Chem. Soc.* **123**, 11686 (2001).
- [237] M. Krauss, and R. Osman, *J. Phys. Chem.* **99**, 11387 (1995).
- [238] G. M. Just, E. N. Sharp, S. J. Zalyubovsky, and T. A. Miller, *Chem. Phys. Lett.* **417**, 378 (2006).
- [239] E. N. Sharp, P. Rupper, and T. A. Miller, *Phys. Chem. Chem. Phys.* **10**, 3955 (2008).
- [240] S. Yamauchi, N. Hirota, S. Takahara, H. Misawa, K. Sawabe, H. Sakuragi, and K. Tokumaru, *J. Am. Chem. Soc.* **111**, 4402 (1989).
- [241] A. Mardyukov, and W. Sander, *Chem.-Eur. J.* **15**, 1462 (2009).

- [242] M.-W. Chen, G. M. P. Just, T. Codd, and T. A. Miller, *J. Chem. Phys.* **135**, 184304 (2011).
- [243] G. M. P. Just, P. Rupper, T. A. Miller, and W. L. Meerts, *Phys. Chem. Chem. Phys.* **12**, 4773 (2010).
- [244] G. M. P. Just, P. Rupper, T. A. Miller, and W. L. Meerts, *J. Chem. Phys.* **131**, 184303 (2009).
- [245] J. T. Stewart, M. N. Sullivan, and M. C. Heaven, *J. Mol. Spectrosc.* **322**, 18 (2016).
- [246] J. H. Bartlett, R. A. VanGundy, and M. C. Heaven, *J. Chem. Phys.* **143**, 044302 (2015).
- [247] R. W. Field, G. A. Capelle, and C. Jones, *J. Mol. Spectrosc.* **54**, 156 (1975).
- [248] C. Focsa, A. Poclet, B. Pinchemel, R. Le Roy, and P. Bernath, *J. Mol. Spectrosc.* **203**, 330 (2000).
- [249] M. Hultin, and A. Lagerqvist, *Arkiv Fysik* **2**, 471 (1951).
- [250] A. Lagerqvist, *Naturwissenschaften* **40**, 268 (1953).
- [251] A. Lagerqvist, *Arkiv Fysik* **8**, 83 (1954).
- [252] R. F. Marks, R. A. Gottscho, and R. W. Field, *Phys. Scr.* **25**, 312 (1982).
- [253] R. F. Marks, H. S. Schweda, R. A. Gottscho, and R. W. Field, *J. Chem. Phys.* **76**, 4689 (1982).
- [254] J. B. Norman, K. J. Cross, H. S. Schweda, M. Polak, and R. W. Field, *Mol. Phys.* **66**, 235 (1989).

- [255] A. van Groenendael, M. Tudorie, C. Focsa, B. Pinchemel, and P. Bernath, *J. Mol. Spectrosc.* **234**, 255 (2005).
- [256] D. P. Baldwin, E. J. Hill, and R. W. Field, *J. Am. Chem. Soc.* **112**, 9156 (1990).
- [257] S. F. Rice, H. Martin, and R. W. Field, *J. Chem. Phys.* **82**, 5023 (1985).
- [258] J. N. Allison, R. J. Cave, and W. A. Goddard, *J. Phys. Chem.* **88**, 1262 (1984).
- [259] C. W. Bauschlicher, and D. R. Yarkony, *J. Chem. Phys.* **68**, 3990 (1978).
- [260] J. Cheng, H. Chen, X. Zhu, and X. Cheng, *J. Mol. Struct.* **1084**, 122 (2015).
- [261] R. N. Diffenderfer, and D. R. Yarkony, *J. Chem. Phys.* **77**, 5573 (1982).
- [262] W. B. England, *Chem. Phys.* **53**, 1 (1980).
- [263] H. Khalil, V. Brites, F. Le Quéré, and C. Léonard, *Chem. Phys.* **386**, 50 (2011).
- [264] H. Khalil, F. Le Quéré, V. Brites, and C. Léonard, *J. Mol. Spectrosc.* **271**, 1 (2012).
- [265] H. Khalil, F. Le Quéré, C. Léonard, and V. Brites, *J. Phys. Chem. A* **117**, 11254 (2013).
- [266] D. P. Baldwin, and R. W. Field, *J. Mol. Spectrosc.* **139**, 68 (1990).
- [267] J. J. Scherer, *Cavity Ringdown Laser Absorption Spectroscopy of Transition Metal Cluster Systems*, Ph.D. thesis, University of California, Berkley (1994).
- [268] H. Salami, and A. J. Ross, *J. Mol. Spectrosc.* **233**, 157 (2005).
- [269] R. Pereira, and D. H. Levy, *J. Chem. Phys.* **105**, 9733 (1996).
- [270] D. P. Baldwin, and R. W. Field, *J. Mol. Spectrosc.* **133**, 90 (1989).
- [271] J. F. W. Herschel, *Trans. R. Soc. Edinburg* **9**, 445 (1823).

- [272] C. G. James, and T. Sudgen, *Nature* **175**, 333 (1955).
- [273] L. M. Ziurys, D. A. Fletcher, M. A. Anderson, and W. L. Barclay Jr., *Astrophys. J. Supp. Series* **102**, 425 (1996).
- [274] T. Tsuji, *Astron. Astrophys.* **23**, 411 (1973).
- [275] P. F. Bernath, *Science* **254**, 665 (1991).
- [276] D. A. Fletcher, M. A. Anderson, W. L. Barclay, and L. M. Ziurys, *J. Chem. Phys.* **102**, 4334 (1995).
- [277] M. Li, and J. A. Coxon, *J. Chem. Phys.* **104**, 4961 (1996).
- [278] Y. Ni, *Laser Spectroscopy and Structure of Magnesium Hydroxide and Deuterated Magnesium Hydroxide: The A-X System*, Ph.D. thesis, University of California, Santa Barbara (1986).
- [279] P. Bunker, M. Kolbuszewski, P. Jensen, m. Brumm, M. Anderson, W. Barclay, L. Ziurys, Y. Ni, and D. O. Harris, *Chem. Phys. Lett.* **239**, 217 (1995).
- [280] M. Anderson, M. Allen, W. Barcaly, and L. Ziurys, *Chem. Phys. Lett.* **205**, 415 (1993).
- [281] P. I. Presunka, and J. A. Coxon, *Chem. Phys.* **190**, 97 (1995).
- [282] C. W. Bauschlicher, S. R. Langhoff, and H. Partridge, *J. Chem. Phys.* **84**, 901 (1986).
- [283] G. Theodorakopoulos, I. D. Petsalakis, H.-P. Liebermann, R. J. Buenker, and J. Koput, *J. Chem. Phys.* **117**, 4810 (2002).
- [284] J. Koput, and K. A. Peterson, *J. Phys. Chem. A* **106**, 9595 (2002).
- [285] A. Hinchliffe, *J. Mol. Struct.* **64**, 289 (1980).

- [286] J. Koput, and K. A. Peterson, *J. Phys. Chem. A* **107**, 3981 (2003).
- [287] K. J. Mascaritolo, J. M. Merritt, M. C. Heaven, and P. Jensen, *J. Phys. Chem. A* **117**, 13654 (2013).
- [288] R. C. Hilborn, Z. Qingshi, and D. O. Harris, *J. Mol. Spectrosc.* **97**, 73 (1983).
- [289] J. B. West, R. S. Bradford, J. D. Eversole, and C. R. Jones, *Rev. Sci. Instrum.* **46**, 164 (1975).
- [290] P. Bernath, and C. R. Brazier, *Astrophys. J.* **288**, 373 (1985).
- [291] R. F. Wormsbecher, M. Trkula, C. Martner, R. E. Penn, and D. O. Harris, *J. Mol. Spectrosc.* **97**, 29 (1983).
- [292] P. Bernath, and S. Kinsey-Nielsen, *Chem. Phys. Lett.* **105**, 663 (1984).
- [293] C. N. Jarman, and P. F. Bernath, *J. Chem. Phys.* **97**, 1711 (1992).
- [294] Z. J. Jakubek, and R. W. Field, *J. Chem. Phys.* **98**, 6574 (1993).
- [295] L. Ziurys, W. L. Barcaly Jr., and M. Anderson, *Astrophys. J.* **384**, L63 (1992).
- [296] B. P. Nuccio, A. J. Apponi, and L. M. Ziurys, *J. Chem. Phys.* **103**, 9193 (1995).
- [297] R. A. Hailey, C. Jarman, and P. F. Bernath, *J. Chem. Phys.* **107**, 669 (1997).
- [298] C. M. Taylor, R. K. Chaudhuri, and K. F. Freed, *J. Chem. Phys.* **122**, 044317 (2005).
- [299] P. F. Bernath, *Spectra of Atoms and Molecules* (Oxford University Press, 2005).
- [300] M. Dick, P. Sheridan, J.-G. Wang, S. Yu, and P. Bernath, *J. Mol. Spectrosc.* **240**, 238 (2006).
- [301] J. Brown, and A. Carrington, *Rotational Spectroscopy of Diatomic Molecules* (Cambridge Univ. Press, 2003).

- [302] F. Hund, *Z. Physik.* **42**, 93 (1927).
- [303] J. Van Vleck, *Phys. Rev.* **33**, 467 (1929).
- [304] H. Lefebvre-Brion, and R. W. Field, *The Spectra and Dynamics of Diatomic Molecules* (Elsevier Academic Press, 2004).
- [305] D. M. Thomas, and L. Andrews, *J. Mol. Spectrosc.* **50**, 220 (1974).
- [306] L. Andrews, and B. S. Ault, *J. Mol. Spectrosc.* **68**, 114 (1977).
- [307] B. Ostojić, P. Bunker, P. Schwerdtfeger, A. Gertych, and P. Jensen, *J. Mol. Spectrosc.* **1023**, 101 (2012).
- [308] B. Ostojić, P. Jensen, P. Schwerdtfeger, B. Assadollahzadeh, and P. Bunker, *J. Mol. Spectrosc.* **263**, 21 (2010).
- [309] B. Ostojić, P. R. Bunker, P. Schwerdtfeger, B. Assadollahzadeh, and P. Jensen, *Phys. Chem. Chem. Phys.* **13**, 7546 (2011).
- [310] B. Ostojić, P. Jensen, P. Schwerdtfeger, and P. R. Bunker, *J. Phys. Chem. A* **117**, 9370 (2013).
- [311] B. Ostojić, P. Jensen, P. Schwerdtfeger, and P. Bunker, *J. Mol. Spectrosc.* **301**, 20 (2014).
- [312] A. I. Boldyrev, and J. Simons, *J. Phys. Chem.* **99**, 15041 (1995).
- [313] H.-J. Werner, P. J. Knowles, G. Knizia, F. R. Manby, and Schtz, M., *WIREs Comput. Mol. Sci.* **2**, 242 (2012).
- [314] T. Dietz, M. Duncan, D. E. Powers, and R. E. Smalley, *J. Chem. Phys.* **74**, 6511 (1981).
- [315] M. Duncan, *Rev. Sci. Instrum.* **83**, 041101/1 (2012).

- [316] V. Bondybey, and J. English, *Chem. Phys. Lett.* **111**, 195 (1984).
- [317] H. Werner, and P. J. Knowles, *J. Chem. Phys.* **82**, 5053 (1985).
- [318] P. J. Knowles, and H.-J. Werner, *Chem. Phys. Lett.* **115**, 259 (1985).
- [319] H.-J. Werner, and P. J. Knowles, *J. Chem. Phys.* **89**, 5803 (1988).
- [320] P. J. Knowles, and H.-J. Werner, *Chem. Phys. Letters* **145**, 514 (1988).
- [321] P. J. Knowles, and H.-J. Werner, *Theor. Chim. Acta* **84**, 95 (1992).
- [322] S. Langhoff, and E. R. Davidson, *Int. J. Quant. Chem.* **8**, 61 (1974).
- [323] M. Reiher, and A. Wolf, *J. Chem. Phys.* **121**, 2037 (2004).
- [324] M. Reiher, and A. Wolf, *J. Chem. Phys.* **121**, 10945 (2004).
- [325] A. Wolf, M. Reiher, and B. A. Hess, *J. Chem. Phys.* **117**, 9215 (2002).
- [326] J. Tennyson, M. A. Kostin, P. Barletta, G. J. Harris, O. L. Polyansky, J. Ramanlal, and N. F. Zobov, *Comput. Phys. Commun.* **163**, 85 (2004).
- [327] W. J. Balfour, and R. F. Whitlock, *Can. J. Phys.* **53**, 472 (1975).
- [328] C. R. Vidal, *J. Chem. Phys.* **72**, 1864 (1980).
- [329] J. Park, H. M. T. Nguyen, Z. F. Xu, and M. C. Lin, *J. Phys. Chem. A* **113**, 12199 (2009).
- [330] C.-W. Zhou, V. V. Kislov, and A. M. Mebel, *J. Phys. Chem. A* **116**, 1571 (2012).
- [331] M. J. Fadden, and C. M. Hadad, *J. Phys. Chem. A* **104**, 8121 (2000).